Search for charged stable massive particles in 7TeV proton-proton collision data with the ATLAS detector at the LHC

Matthew George Lecore King

(Degree)
博士（学術）

(Date of Degree)
2013-03-25

(Date of Publication)
2013-07-04

(Resource Type)
doctoral thesis

(Report Number)
甲5710

(URL)
https://hdl.handle.net/20.500.14094/D1005710

Search for charged stable massive particles in 7TeV proton-proton collision data with the ATLAS detector at the LHC

Matthew King

Department of Physics, Graduate School of Science,
Kobe University

February 25, 2013

Contents

Chapter 1.

Introduction

Particle physics is the study of the elementary constituents of matter and their interactions. Discoveries over the course of the mid 20th century led to the development of the Standard Model of particle physics in the 1970s. In the Standard Model, all matter is composed of spin $\frac{1}{2}$ fermions and all interactions are mediated by integer spin bosons. This model incorporated all particles known at the time and predicted the existence of new particles, which were then discovered in subsequent particle accelerator experiments.

The Standard Model, despite its many successes, does not yet provide a complete description of the universe. There is no definite explanation for the gravitational force or a candidate particle which could be responsible for the observed "dark matter" of the universe. Furthermore, at a theoretical level, it requires considerable fine tuning of parameters to give a reasonable mass for the Higgs boson.

These problems and others have led to interest in many theories that extend the Standard Model and account for the remaining issues. Many of these theories predict phenomena which should be observable in particle accelerators. Searches for such phenomena are undertaken whenever a new energy threshold, with the potential of producing previously unobserved interactions, is reached.

The Large Hadron Collider (LHC) at CERN is a proton-proton collider designed to provide collisions at the highest energy level yet attained. The previously most powerful accelerator, Tevatron at Fermilab, produced proton-antiproton collisions at an energy scale up to 2TeV; by comparison the LHC is designed to reach energies of 14TeV. The LHC thus represents a significant increase in collision energy and is capable of producing interactions unobservable at previous accelerators.

The ATLAS detector is one of two general purpose detectors on the LHC. It is designed to gather as much information from particles produced in collisions as possible. The detector consists of an array of different technologies, designed to measure different aspects of the particles produced. Reconstructing the path and momentum of particles through the detector allows the properties of the interaction which produced them to be studied.

Stable Massive Particles (SMPs) are predicted to exist by a number of theories extending the Standard Model. The term 'stable' in SMPs is relative; any particle with a

lifetime long enough for it to travel a measurable distance may be deemed stable. SMPs represent a fairly generic signature of unexplained physics and are thus a subject of searches for new phenomena at the LHC.

The different possibilities for an SMP and the time it takes to decay leave quite different signatures in particle detectors. If the SMP is charged and has a lifetime that leads to it decaying inside the detector, it will leave a large kink in its track at the point of the decay. Alternatively, if the SMP is not charged, energetic particles from its decay will be produced at a secondary vertex, removed from the beam. If the lifetime of the SMP is long enough for it to traverse the entire detector before decaying it will leave a different signature. If the SMP is chargeless, a significant amount of energy will be carried away from the interaction point resulting in events with large amounts of missing energy. Finally, a charged long lived SMP may be directly observable as a "heavy muon-like" track, with large momentum but a relatively low velocity.

The ATLAS detector has a muon spectrometer designed specifically for the detection and reconstruction of muon tracks. Its elements have sufficient time measurement resolution and distance from the interaction point to make accurate measurements of particle velocity. If charged long lived SMPs exist and are produced by the collisions at the LHC it should be possible to identify them by measuring their velocity in the ATLAS muon spectrometer.

In this thesis an SMP search is conducted at the ATLAS detector using 4.06fb^{-1} of LHC pp collisions at 7TeV. The search method consists of tagging high momentum particles with low velocity. For this purpose, a detailed study into the measurement of the velocity of particles at ATLAS was conducted. The SMP search will be performed in the framework of the long lived stau ($\widetilde{\tau}$) particle predicted by the gauge mediated supersymmetry breaking model. Chapter 2 explains the physical motivation behind this model and the way in which the $\widetilde{\tau}$ as well as likely background is produced. Details of the LHC and ATLAS are provided in chapter 3. Chapter 4 describes how the real data used in this study was selected and how the simulated data was produced. Chapter 5 details the operation of MuonBetaRefit, how tracks are reconstructed in the muon spectrometer and how velocity measurements are made. The SMP search method is described in chapter 6 along with the results obtained. Chapter 7 provides a final summary.

Chapter 2.

Theoretical motivation

The Standard Model of particle physics represents the current understanding of the universe by physicists. The model has had great successes in predicting the existence of particles before their discovery and explaining the nature of physical interactions. Most of the particles predicted by the Standard Model have been conclusively discovered in particle accelerator experiments. Nevertheless, there exist some problems with the Standard Model and further extension of the model is expected to be required.

Many theoretical extensions to the Standard Model have been proposed, some of which predict the existence of charged, stable, massive particles (SMPs). The most straightforward instance is where additional states of the Standard Model particles are possible, with the addition of a conserved, or partially conserved, quantum number. This study is performed in the framework of a search for long lived SMPs predicted by supersymmetry (SUSY), which adds R-parity to the Standard Model particles.

This chapter aims to introduce the Standard Model and outline some of its remaining problems (section 2.1). Then supersymmetry is introduced and its features examined (section 2.2). Finally the experimental signatures predicted by such a theory and the origin of Standard Model background to these signatures is discussed (section 2.3).

2.1. The Standard Model

The Standard Model (SM)[1][2] contains three generations of pointlike fermions (spin $\frac{1}{2}$ particles) and an array of pointlike bosons (spin 1 particles). These particles, along with their basic properties, are summarized in table 2.1.

The fermions inside each generation have similar properties, but the higher order generations have increasing mass and are thus unstable. The only exceptions are the neutrinos, which all have similar small masses. The first generation of fermions is stable to within the lifetime of the universe, and composes nearly all known matter.

In the Standard Model, forces are mediated by gauge bosons. Photons mediate the electromagnetic force, the W and Z bosons mediate the weak nuclear force and

	Name	Symbol	Charge (e)	Mass (GeV)
1st Gen. quark	up	u	$+\frac{2}{3}$	$\approx 3 \times 10^{-3}$
1st Gen. quark	down	d	$-\frac{1}{3}$	$\approx 4 \times 10^{-3}$
1st Gen. lepton	electron	e^-	-1	511×10^{-6}
1st Gen. lepton	electron neutrino	ν_e	0	$< 2 \times 10^{-9}$
2st Gen. quark	charm	c	$+\frac{2}{3}$	1.29
2st Gen. quark	strange	s	$-\frac{1}{3}$	95×10^{-3}
2st Gen. lepton	muon	μ^-	-1	106×10^{-3}
2st Gen. lepton	muon neutrino	ν_μ	0	$< 0.17 \times 10^{-3}$
3st Gen. quark	top	t	$+\frac{2}{3}$	4.2
3st Gen. quark	bottom	b	$-\frac{1}{3}$	173
3st Gen. lepton	tau	τ	-1	1777
3st Gen. lepton	tau neutrino	ν_τ	0	$< 15.5 \times 10^{-3}$
Boson	photon	γ	0	0
Boson	gluon	g	0	0
Boson	Z	Z^0	0	91
Boson	W	$W^\pm$	± 1	80

Table 2.1.: Discovered Standard Model particles

gluons mediate the strong nuclear force. The Higgs boson (H) is predicted to give rise to elementary particle masses but its exact properties are not currently known. A gravity-mediating graviton (G) has also been proposed, but not yet discovered.

Of the elementary fermions, only quarks are influenced by the strong nuclear force. Composite particles formed from multiple quarks held together by the strong nuclear force are known as hadrons and come in two types, baryons and mesons. Baryons, such as protons and neutrons, are made up of three quarks or three anti-quarks. Mesons are composed of one quark and one anti-quark.

Quarks can only decay from the heavy and unstable species to the lighter and more stable species through the weak nuclear interaction. The decay occurs through the emission of a real or virtual W-boson, which decays to a fermion-antifermion pair.

2.1.1. Unresolved problems

The Standard Model, despite its successes in describing physical phenomena, has some problems remaining, most notably the heirarchy problem and dark matter.

The greatest remaining issue with the Standard Model is the so called "hierarchy problem". The electromagnetic force and weak nuclear force can be unified above an energy scale equal to the mass of the Z boson. The equivalent scale for gravitational interaction, the reduced Planck scale (m_P), is much higher:

$$m_\mathrm{Z} \approx 90 \mathrm{GeV} \ll m_\mathrm{P} \approx 2 \times 10^{18} \mathrm{GeV}. \tag{2.1}$$

The origin of this difference is difficult to resolve naturally in quantum field theory. The same result can be obtained, but requires fine tuning of the Standard Model parameters.

Another prominent problem is the lack of a viable dark matter candidate. Dark matter refers to matter that interacts via the gravitational force, but does not interact significantly in any other way. There is strong evidence for the existence of about five times more dark matter in the universe than observable matter. Neutrinos are the only SM particles with weak enough interactions to be "dark", but are too light to be contained in smaller galaxies and cannot compose all dark matter in the universe.

The current Standard Model is incapable of accounting for these issues and will require additional extension.

2.2. Supersymmetry

Supersymmetry is a physical symmetry that connects the properties of bosons to fermions, which, in the Standard Model, are completely separate. In practice this leads to the generation of a "superpartner" of each particle in the Standard Model, fermionic partners for bosons and bosonic partners for fermions. R-parity is also introduced in many supersymmetric models as a way of suppressing the decays of Standard Model particles into SUSY particles. The R-quantum number is 1 for all Standard Model particles and -1 for all SUSY particles and is conserved. This leads to the phenomenology that; SUSY particles must be produced in pairs, decays of SUSY particles must produce other SUSY particles. The lightest SUSY particle is thus stable as it has no way to decay whilst conserving R.

If the symmetry between Standard Model particles and their superpartners was unbroken, the masses would be similar. SUSY particles have not been observed in particle accelerator experiments and must be massive. The symmetry must therefore be broken at lower energies. There are many possible ways in which this symmetry breaking can occur, leading to numerous proposed supersymmetric models.

The notation of the superpartners of SM particles follows the naming of the SM particles, but with an additional prefix or suffix. Supersymmetric fermions and classifications of fermion have an 's' prefix (i.e. squark, slepton, sdown and smuon). Similarly, supersymmetric bosons have an 'ino' suffix (i.e. Wino, photino). The symbolic representation is the same as that of the SM superpartner, with an overhead tilde e.g. $\widetilde{W}^{\pm}$, $\widetilde{e}$, $\widetilde{\tau}$. There are also mixed mass eigenstates of the charged (chargino $\widetilde{\chi}^{\pm}$) and neutral (neutralino $\widetilde{\chi}^{0}$) gauge boson superpartners.

Many of the models proposed can lead to solutions to the hierarchy problem as the quantum loops of the additional superpartners cancel divergences in loops of the SM particles. Some models also yield a candidate for dark matter in the form of the neutralino or gravitino.

Of interest to this study is the Gauge Mediated Supersymmetry Breaking (GMSB) model[3], where the necessary symmetry breaking is performed by messenger particles through SM gauge interactions. The parameters of the model are:

- $m_{messenger}$ - the mass scale of the messenger particles;

- n_5 - the number of messenger particle $SU(5)$ vectors;

- C_{grav} - the gravitino mass scale factor;

- $s(\mu)$ - the sign of the Higgsino mass parameter;

- $\tan \beta$ - the ratio of the vacuum expectation values of the up-type and down-type Higgs field;

- Λ - the scale of sparticle masses.

The lightest supersymmetric particle (LSP) in GMSB models is the gravitino. This particle is stable, but unobservable in any particle detector. The next to lightest LSP (NLSP) can be either the lightest neutralino, the stau or a combination of mass degenerate sleptons. The neutralino case corresponds to a small and near-excluded parameter space at small values of Λ and $m_{messenger}$; for the purposes of this study the NLSP can be assumed to be the lightest stau[1], hereafter referred to simply as $\widetilde{\tau}$.

The NLSP can only interact with the gravitino via the gravitational force, which is weak enough that semi stable states of the NLSP are possible. If the gravitino mass scale factor is sufficiently large, the decay of the NLSP may take enough time for it to traverse a particle detector.

In models where the NLSP is a charged slepton, such as the stau, with a long lifetime, it should be observable in particle detectors[4]. In such a model, the slepton would be observable as a heavy charged lepton with behaviour similar to a Standard Model muon, but with far greater mass.

2.3. Event signatures

This section examines the signatures of interest when searching for long lived sleptons, as well as the expected background to the search and its origins.

2.3.1. GMSB long lived $\widetilde{\tau}$ signature

In GMSB where the NLSP is a long lived $\widetilde{\tau}$, heavier sparticles will decay in a cascade down to $\widetilde{\tau}$s, which will slowly decay into a gravitino and a charged lepton[7][8]. Due to

---

[1]The masses of sfermions with right and left spins can differ on a similar scale to their masses.

the conservation of R-parity, the sparticles must be produced in pairs. Both sparticles decay down into the NLSP, leading to the generation of two $\widetilde{\tau}$s.

The cascade can produce jets if the original sparticles are squarks or gluinos. If the original particles are sleptons other than the $\widetilde{\tau}$, then high energy leptons are produced. High energy leptons may also be produced by the semi-leptonic decays of squarks. Alternatively, $\widetilde{\tau}$, anti-$\widetilde{\tau}$ pairs may be produced directly, in which case there are no additional particles.
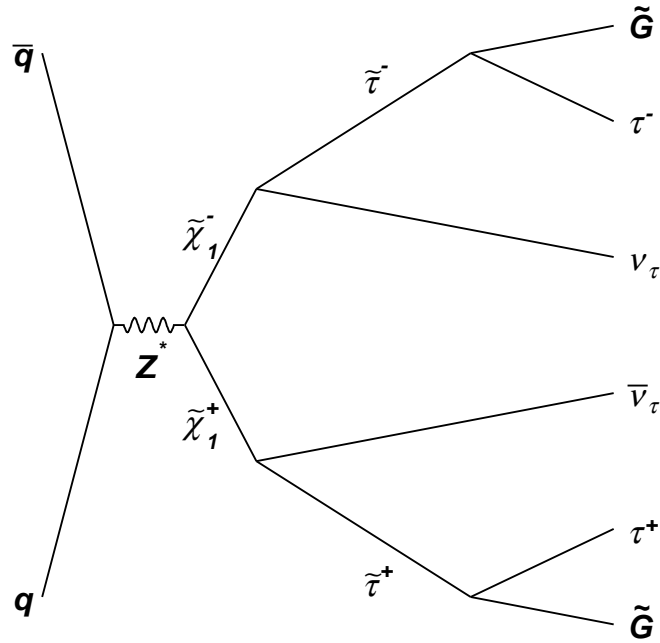
Figure 2.1.: Typical GMSB decay chain to Gravitino ($\tilde{G}$) LSP via the $\widetilde{\tau}$ NLSP

The energy released by these cascades is large, but the distribution of momentum between the event products can vary, leading to different possible event signatures. The cascade is highly likely to produce neutrinos. If these are produced with large momentum then the event may have "missing Energy", where energy is carried off by the neutrinos and cannot be detected. If the $\widetilde{\tau}$ are not the first sleptons produced, then leptons will also be produced. These leptons also have the possibility of being produced with large momentum. Moreover, the $\widetilde{\tau}$ itself, produced with high momentum, is charged and should be directly detectable.

The $\widetilde{\tau}$, if it does not decay inside the detector, should leave a track indistinguishable from a muon, except for its considerably higher mass ($m_\mu = 0.105\text{GeV}$, $m_{\widetilde{\tau}} > 100\text{GeV}$). The higher mass will lead to a lower particle velocity, which can be measured. This signature of a slow muon-like track is the main indication of a long lived $\widetilde{\tau}$ event.

2.3.2. Background to GMSB $\widetilde{\tau}$ signature

As the main feature of interest to this study is the track made by the $\widetilde{\tau}$ itself. The background will consist of "fake" $\widetilde{\tau}$ candidates. Fake candidates are expected to be entirely composed of high momentum muons with mis-measured velocity. Muons with actual low velocity are quickly stopped inside denser detector systems and are not reconstructed as muons. Additionally, measurements of muon momentum are far less prone to measurement error than those of muon velocity.
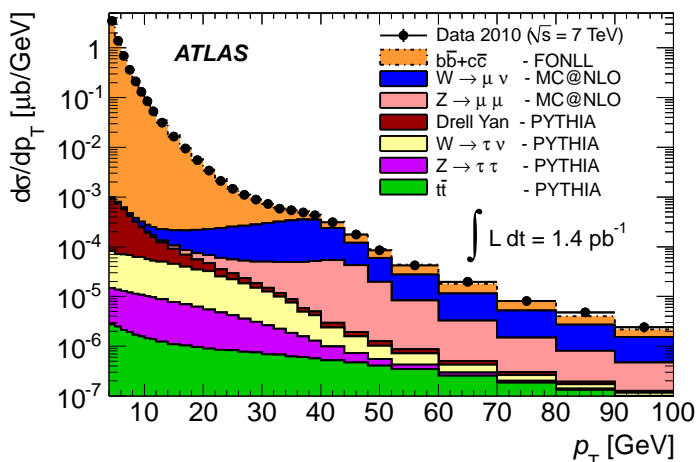
Figure 2.2.: Simulation of processes contributing to the muon cross section at $\sqrt{s} = 7$TeV and measured inclusive muon cross section as a function of p_T at ATLAS in 2010[5]

Many Standard Model processes produce muons of sufficient momentum to become fake candidates (fig. 2.2). In hadron colliders such as the LHC, production of high momentum muons, for the purposes of this study $p_T > 30$GeV, is dominated by the decays of b and c-quarks with significant additional contribution from the decays of W and Z-bosons.

2.3.3. Muon reference

A reference signal of muons is required for calibration of the velocity measurement method. To ensure that the muons are produced at a known time they should originate from a process with prompt decays. Muons produced in isolation are preferred as measurements made on its track are more likely to be a response to the muon itself.

Any single muon decay channel can be boosted to give a muon of almost any momentum. By finding the invariant mass of a pair of muons, however, it is possible to find the mass of the particle responsible for their production. By identifying muon pairs
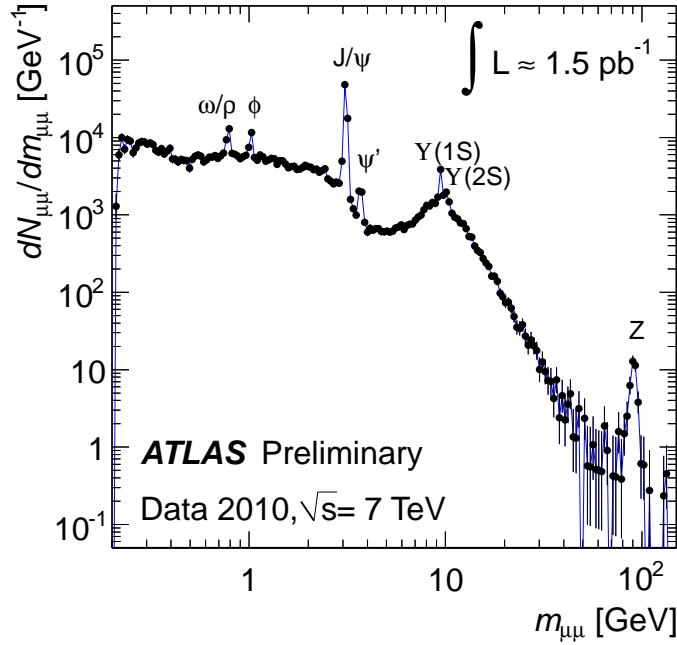
Figure 2.3.: Spectrum of di-muon invariant mass from ATLAS 2010 data, peaks corresponding to known particle decays are shown.
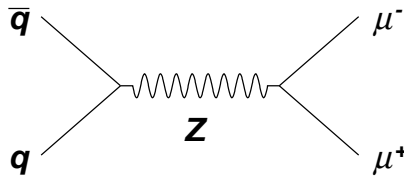
Figure 2.4.: $Z{\to}\mu\mu$ decay channel

with invariant mass close to that of a particle known to decay to pairs of muons, a clean reference sample can be produced.

Figure 2.3 shows the di-muon invariant mass distribution taken at ATLAS in 2010[6]. The highest invariant mass muon pairs are produced by Z-boson decays. $Z{\to}\mu\mu$ decays produce prompt pairs of isolated muons with momentum higher than the bulk of those produced by other processes. Mis-tagging of pairs of individually produced muons as a $Z{\to}\mu\mu$ pair is minimal due to this high momentum. Muons produced in the decay of Z-bosons thus form a reliable muon reference signal for the purposes of calibration.

Chapter 3.

The LHC & ATLAS

3.1. The Large Hadron Collider

The Large Hadron Collider (LHC) is the largest particle collider in the world and has operated at CERN since 2009 in tunnels previously used by the Large Electron-Positron Collider (LEP). The LHC is designed to collide protons at a centre of mass energy of 14TeV with a luminosity of $0.1\text{nb}^{-1}\text{s}^{-1}$, although the design energy level has not yet been reached.

The LHC is fed bunches of accelerated protons by the previously existing SPS accelerator and further accelerates them in two parallel rings in opposite directions through the LHC tunnels. Superconducting magnets are used to maintain beam focus and to bend the beams around the ring.

Figure 3.1.: The Large Hadron Collider. Detectors are highlighted with red text, other points are used for maintenance and access to the LHC tunnels

The beams are collided with each other at four points around the LHC, providing proton-proton collision events for the four experiments located at these points (fig. 3.1).

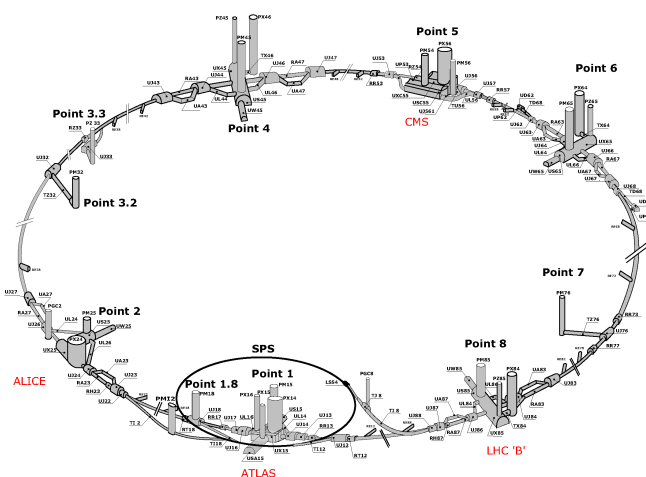ATLAS and CMS are general purpose detectors useful in many different physics searches, most notably that for the Higgs boson. LHCb searches for new physics and checks the predictions of the current Standard Model by measuring the properties of *b*-hadron related processes. ALICE is designed to observe the quark-gluon plasma state from heavy ion collisions and make measurements related to furthering the understanding of strong force interactions.

The LHC beam is deployed in numbered "runs", split into run periods. Each run lasts for up to around 20 hours before the beam is dumped and a new run started.

3.1.1. Interaction energy and cross sections

The protons accelerated by the LHC, unlike the particles used in lepton accelerators such as LEP, are composite particles composed of quarks and gluons. The energy held by a proton is not centralized at a single point but spread over numerous partons, namely the quarks and gluons that make up the particle as well as a sea of particles resulting from quantum fluctuations in and around the proton. The energy for actual interactions of these partons is thus lower than the centre of mass energy of the protons and varies with the distribution of energy amongst partons.

The cross sections for physics processes depend on the interaction energy. Some notable cross sections and their dependence on energy are shown in figure 3.2. Although the total interaction cross section of the LHC does not increase greatly with the increase in interaction energy over the Tevatron at Fermilab, the cross sections of rarer processes, such as those involving the Higgs, are increased significantly.

Still, the total event cross section is multiple orders of magnitude greater than that for rare processes. Detectors must thus be able to differentiate events likely to contain physics processes of interest from those that do not with high efficiency. This is especially true when conducting searches for evidence of SUSY for example, where expected cross sections for models not previously excluded are lower than all processes shown in figure 3.2. The process of quickly reducing the high event rate to a more manageable rate of events with properties of interest is known as triggering. Triggering in the ATLAS detector is covered in section 3.2.5.

3.1.2. Luminosity

Interactions occur during proton bunch crossings on a statistical basis. Luminosity (L) gives an estimate of how many chances for interaction there are per unit of time. The interaction rate of a process with cross section σ_{phy} is related to the luminosity by

$$\frac{\mathrm{d}N}{\mathrm{d}t} = \sigma_{phy} \times L \tag{3.1}$$

proton - (anti)proton cross sections
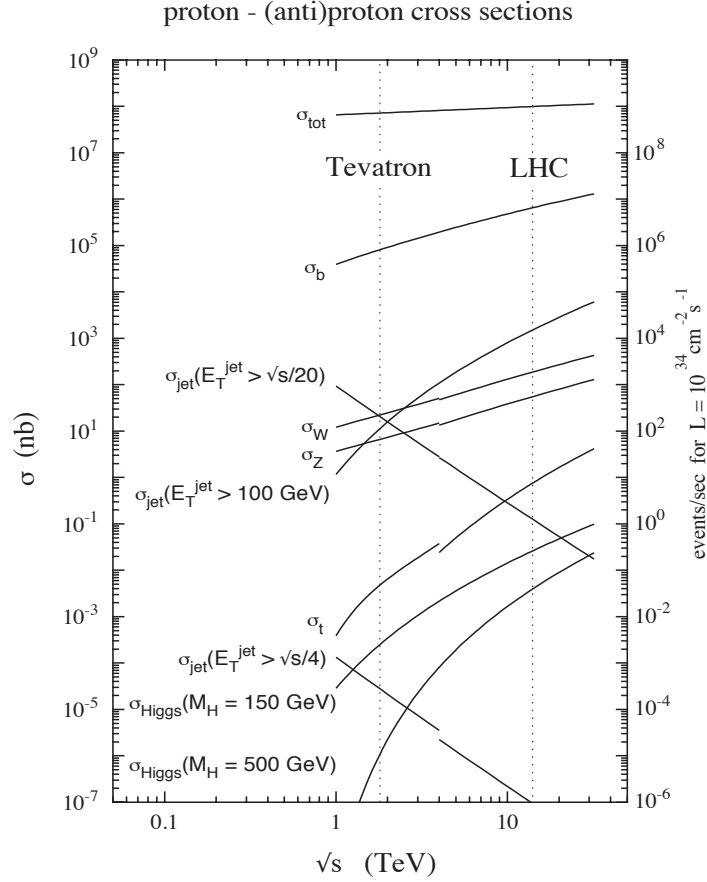
Figure 3.2.: Relationship between physics cross sections and interaction energy. The LHC level is drawn at the design energy, the Tevatron at Fermilab is also drawn for comparison.

The integrated luminosity ($\mathcal{L}$) is simply L integrated over time to give the total number of chances for interaction over a period of time.

Luminosity is defined as the number of particles passing a unit of area per unit of time multiplied by the opacity of the target. For colliders this becomes more complicated as there is no stationary target and the "opacity" depends on the density distributions of the two beams and their orientation. Assuming the beams follow identical gaussian distributions with vertical and horizontal widths σ_x, σ_y and assuming the beams collide exactly head-on the following equation for luminosity can be derived

$$L = \frac{N_{b1}N_{b2}f_b}{4\pi\sigma_x\sigma_y} \qquad (3.2)$$

where N_{b1}, N_{b2} are the number of protons in the two bunches being collided and f_b is the bunch crossing frequency.

To increase the luminosity it is necessary to increase the number of protons in the bunches, reduce the beam width or increase the crossing frequency by increasing the number of bunches. Luminosity can be increased more subtly by improving the way the beam is focussed and orientated. However these considerations are ignored when deriving equation 3.2. The LHC will be upgraded over the next few years during the "long shutdowns" yielding increased luminosity and collision energy. The detectors will be also be upgraded during this time to deal with the increased event rate.

3.1.3. Data taken in 2011

During 2011 the LHC operated at a proton centre of mass energy of 7TeV. The total luminosity delivered by the LHC during 2011 is 5.61fb^{-1} and of that ATLAS processed and recorded events corresponding to 5.25fb^{-1}.
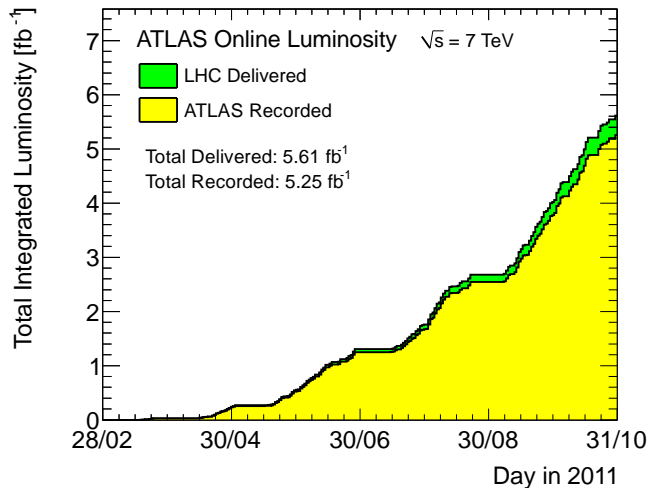
Figure 3.3.: Sum of luminosity by day. Technical faults prevent ATLAS from recording all the luminosity delivered by the LHC.

The cumulative luminosity delivered over 2011 is shown in figure 3.3 and the luminosity can be seen to vary. The variation is due to changes in the operation of the LHC during 2011. The operation can be described as having six separate phases in 2011, separated by five technical stops[9].

- Phase 1: Used 75ns spacing between proton bunches, number of bunches increased to around 200 by the 1st technical stop on March 28th.

- Phase 2: Bunch spacing changed to 50ns, number of bunches increased to 800 by the 2nd technical stop on May 9th.

- Phase 3: Number of bunches increased to 1380 by the 3rd technical stop on July 4th.

- Phase 4: Bunches kept at 1380, improvements in beam focussing used to increase luminosity, next technical stop began on September 29th.

- Phase 5: Further improvements in beam focussing along the z-axis continue to increase luminosity, next technical stop on November 7th.

- Phase 6: Heavy ion runs until end of 2011 data taking period.

3.2. The ATLAS detector

The ATLAS experiment is one of the two general purpose detectors on the LHC. It is designed to be able to reconstruct events from many different physics processes and can be used to investigate a variety of physical theories.
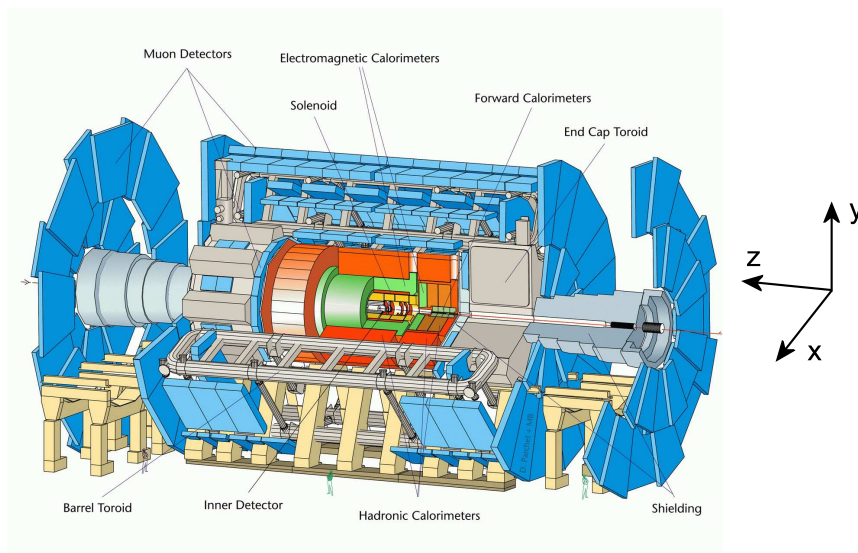
Figure 3.4.: The ATLAS detector

3.2.1. Detector overview

A brief overview of the conventions used in describing the detector and the technologies it implements will be provided.

Coordinate systems

Figure 3.4 shows an overview of the detector and the coordinate system used. The z-axis is defined as running parallel to the beams in an anti-clockwise direction around the LHC, the x-axis points horizontally towards the centre of the LHC and the y-axis

points upwards. Another commonly used coordinate system inside the detector is the pseudorapidity (η) and azimuthal angle (ϕ)

$$\eta = -\log\tan(\theta/2) \tag{3.3}$$

where θ and ϕ are their usual definitions in polar coordinates symmetric around z. η is useful in describing particle detectors such as ATLAS because particle production rates over an interval are approximately proportional to the size of that interval in η. The momentum and path of tracks can be approximately described solely by η and ϕ if little bending occurs in the magnetic field. A common measure of the separation of track direction, or hit position in η and ϕ is $\Delta R = \sqrt{\eta^2 + \phi^2}$.

In the coordinate convention, "transverse" is taken to mean perpendicular to the z-axis and is notated by a subscript T (p_T, E_T etc.). Transverse measurements are important because, due to the composite nature of protons, the momentum of colliding partons may be very different along z, leading to a boosting of event products in either z-direction. Momentum and energy in the transverse plane however can be reliably considered to originate from the physical interaction.

Detector Technologies

The detector can be broadly split into three regions. The barrel refers to the central region where detectors approximately lie in concentric cylinders along z, and two endcaps where detectors are arranged into disks at fixed points in z. The endcap at positive z, η is designated the A-side while endcap at negative z, η is designated the C-side.

There are four magnet systems providing strong magnetic fields throughout ATLAS, The bending of charged particle trajectories in these fields allows ATLAS to measure the momentum of such particles. The centre of the detector is enclosed by a solenoid generating a 2T field along the z-axis. The barrel and two endcap regions each have a toroidal magnet system providing a field circling the detector in the ϕ-direction.

The LHC beam lines enter the detector on either side, enclosed by radiation shielding and cross at the interaction point in the centre of the detector. The inner detector (section 3.2.2) sits inside the central solenoid and detects charged particle tracks around the interaction point with very high granularity. This allows the initial momentum of tracks to be measured and separate tracks to be associated with a common originating event by tracking them back to the same vertex.

Outside of the solenoid lie the electromagnetic and hadronic calorimeters (section 3.2.3), respectively. The calorimeters measure particle energy by stopping them and calculating the energy deposited. The electromagnetic calorimeter is designed to detect particles interacting via the electromagnetic force and will stop lighter species such as photons and electrons. The hadronic calorimeters have enough depth to additionally detect particles interacting via the strong nuclear force and will stop nearly all hadrons.

The muon spectrometer (section 3.2.4) is positioned outside of the calorimeters. In the barrel region the detectors are interspersed with the toroidal magnet, in the endcaps they are positioned in front of, behind and around the toroid. The spectrometer detects any charged particles, but nearly all detectable particles other than muons are stopped inside the calorimeters.

All of these detector systems are built to requirements dictated by the nature of the LHC. The proton-proton collisions make the LHC capable of delivering luminosity levels sufficient for the discovery or exclusion of many popular physics models. However, the collisions also cause massive amounts of background and a very high event rate. The detector must be capable of discriminating events of interest from the background, be resistant to radiation damage and operate fast enough to not be overwhelmed by the event rate.

Figure 3.5 shows the measurements made by the different regions of the detector for different types of particle. Neutrinos, which only interact via the weak nuclear force, traverse the detector without leaving any kind of measurement. Their presence can only be deduced indirectly by reconstructing the other particles in an event and looking for missing transverse momentum (p_T).
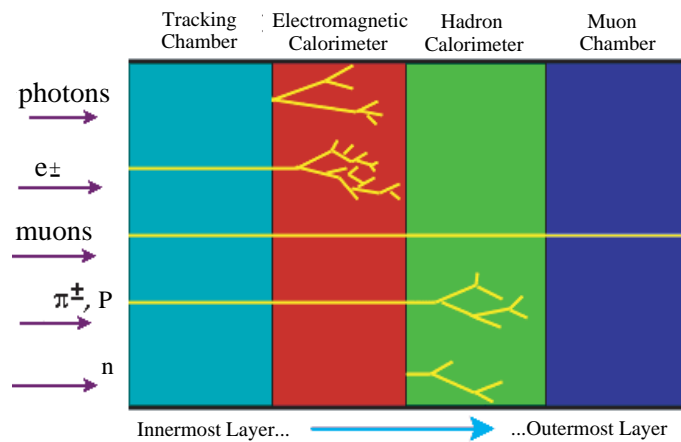
Figure 3.5.: The interactions of different Standard Model particles with the detectors at ATLAS. Not shown are neutrinos, which leave no track in any of the detectors

3.2.2. The inner detector

The inner detector is used to detect charged particles close to the interaction point. It allows particle tracks through the detector to be reconstructed and the particle momentum calculated. Crucially, the tracks must extend close enough to the beam crossing and be of fine enough resolution in η and ϕ that individual vertices can be identified and tracks correctly associated with them. It does this over the range $|\eta| < 2.5$ and is designed to reconstruct particles over a p_T threshold, nominally, of 500MeV.
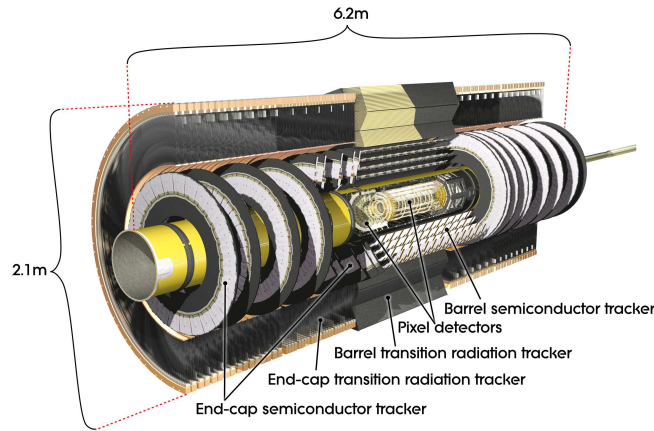
Figure 3.6.: 3D representation of the ATLAS inner detector system

Momentum can be calculated by measuring the amount of bending a track undergoes during its transition though the magnetic field of the solenoid. Since the solenoidal field inside the inner detector lies parallel to the z-axis, the trajectory of charged particles will be bent in the transverse plane by an amount inversely proportional to their momentum in that plane. The inner detector elements are positioned to make their most precise measurements in the ϕ-plane in order to maximise the momentum measurement accuracy.

The inner detector consists of three independent tracking technologies providing complementary readings from which tracks can be made, namely the pixel sensors, semiconductor tracker (SCT) and transition radiation tracker (TRT).

The pixel and SCT detectors

The pixel and SCT trackers are both detectors printed onto semiconductor wafers designed to withstand the radiation dosages associated with close proximity to the interaction point. Semiconducter detectors are reverse biased with a voltage and any charged particles passing through the detector will allow a small amount of current to flow across the voltage. This current is picked up and amplified by associated electronics and comprises the measurement for that sensor.

The pixel sensors represented the cutting edge of semiconductor detectors at the time ATLAS was designed. They have pixels of nominal size $50\mu m \times 400\mu m$ and are formed from an oxygenated material shown to have radiation hardness sufficient for operation in the innermost region of ATLAS. There are 1744 pixel sensors used at ATLAS, each with 47232 pixels. The sensors are arranged in three concentric layers in the barrel, and three layers in each of the endcaps. Each layer is designed to provide a positional measurement accuracy of $10\mu m$ in the ϕ-plane and $115\mu m$ in the η-plane. The cost and complexity associated with this type of detector is very high. For detecting over a larger surface area elsewhere in the detector less complex technologies are preferred.

The SCT is a more traditional style of semiconductor detector with strip elements $12\text{cm} \times 80\mu\text{m}$ in size. Every module is deployed with two layers offset from each other by a 40mrad rotation. This allows each module to make relatively precise measurements along the z-axis despite the 12cm strip length. There are 4 concentric barrel layers and nine layers in each endcap. Both the barrel and endcap sections are designed to provide a measurement accuracy of $17\mu\text{m}$ in the ϕ-plane and $580\mu\text{m}$ in the η-plane. While it does not have the radiation hardness or resolution of the pixel detector, its comparatively low cost and low complexity makes covering a larger detector area possible.

The TRT detector

The TRT detector uses polyimide drift tubes 4mm in diameter to detect charged particles. The tubes are coated with aluminium to provide conductivity. The pickup is a wire running down the inside of the tube, supported at either end of the tube by a plug and connected directly to the readout electronics. The tube walls are kept at a voltage of -1530V relative to the wire. Any charged particle will liberate electrons from the gas mixture filling the tubes. The electrons drift towards the wire and result in a small amount of current flowing from the wire to the readout electronics. This signal is then amplified to give the measurement of the sensor. By calculating the drift time and hence drift radius a designed measurement accuracy of $130\mu\text{m}$ can be obtained in the ϕ plane. No precision measurements can be made in the η-plane.

There are 298304 tubes in the inner detector. In the barrel region they are stacked cylindrically along the z-axis and in the endcap are arranged radially in the transverse plane. The tubes are laid out so that particles with high momentum in the range $|\eta| < 2.0$ typically cross more than 30 tubes. By comparison, the most common number of pixel measurements for a track is 3, around 8 for the SCT. The increased leverage available to the TRT because of the longer track length make a great difference when measuring high momentum tracks. Trajectory bending in such tracks is minimal and difficult to accurately measure over short distances.

Tracking in the inner detector

Tracks are identified in the inner detector by clustering signals from all the detectors and searching for patterns. The combination of precision pixel measurements at short distances followed by a large number of TRT hits extending over a far greater distance allows for robust pattern recognition. There are multiple track reconstruction algorithms, reconstruction from the pixel outwards to find primary tracks and from the TRT inwards to find tracks originating at secondary vertices caused by particle decay away from the interaction point. Primary tracks are reconstructed by the inner detector with an efficiency of around 80%. Secondary tracks, being much more difficult to identify, have reconstruction efficiencies of around 6%[13].
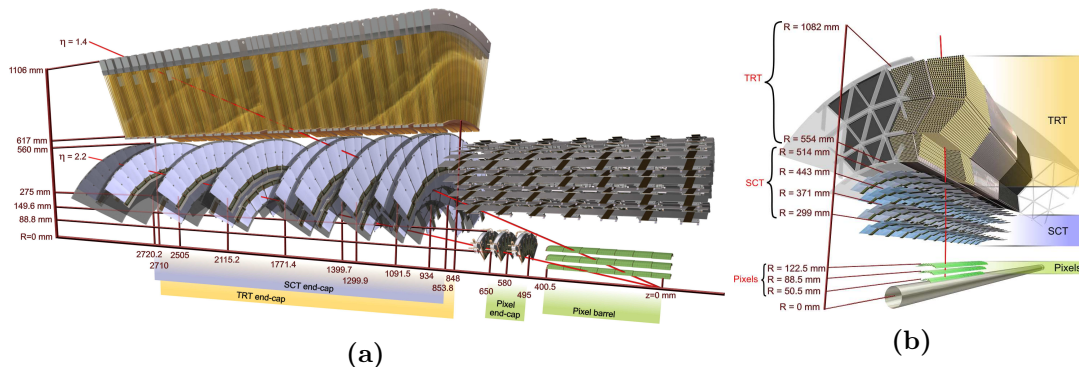
Figure 3.7.: Inner detector tracking in the (a)endcap, (b)barrel regions

The momentum measurements made of the tracks are of a similar resolution across the η range of the detector. The resolution ranges from approximately one percent for tracks with $p_T \approx 1\text{GeV}$ to around 10% for $p_T \approx 200\text{GeV}$. Higher momentum tracks have lower resolution because of the lower degree to which their trajectories are bent in the magnetic field. The greater positional resolution that would be necessary to improve momentum resolution depends not only on the detector module resolution, but also on correct alignment of those modules.

Reconstructed tracks are checked against each other around the interaction point to try to match tracks together into likely event vertices. Correctly identifying which tracks belong to which vertices is essential for physics analysis. The vertex reconstruction efficiency varies with the number of interaction events per bunch crossing [1] ranging from above 70 percent for less than 10 interactions to around 50 percent for more than 40 interactions[13].

3.2.3. The calorimeter

The ATLAS calorimeter makes measurements of particle energy by stopping particles and estimating the energy absorbed. In the η range overlapping the inner detector it is designed to make measurements of granularity sufficient to complement the inner detector tracks. It is also designed to accurately detect chargeless particles not observed in the inner detector. Over a wider η range it is also designed to quickly measure the total transverse energy of all particles in an event to calculate any missing transverse energy, a good indicator of interesting physics, for use in triggering. The calorimeter is designed to quickly stop particles and contain the electron showers produced. This both increases the energy measurement resolution and prevents punch through of heavy particles into the muon spectrometer.

---

[1] The number of events per crossing approximately follows a Poisson distribution and increases with increasing numbers of protons per bunch and improvements to the focal properties of the beams at the interaction point. Typical values during 2011 tend to be several tens of events per crossing
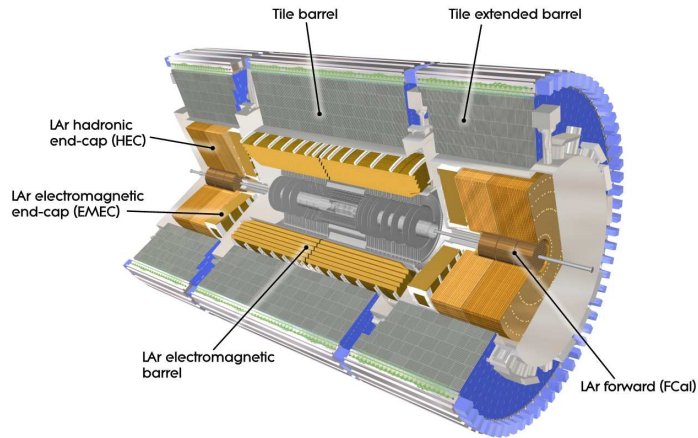
Figure 3.8.: 3D representation of the ATLAS calorimeter system

The calorimeter consists of two concentric systems: inside is the electromagnetic calorimeter; outside is the hadronic calorimeter. The electromagnetic calorimeter depth is such that it stops light and electromagnetically interacting particles such as electrons and photons and measures the energy deposited. It uses a single, liquid argon based detector technology to cover both the barrel and the majority of both endcap regions up to moderately high η. At extremely high η, however, the first layer of the forward calorimeter provides electromagnetic calorimetry information. The hadronic calorimeter is designed to have enough depth to reliably stop particles interacting via the strong nuclear force, but it will also detect electromagnetically interacting particles. The hadronic calorimeter system uses two liquid argon based detectors to cover different η regions of the endcaps
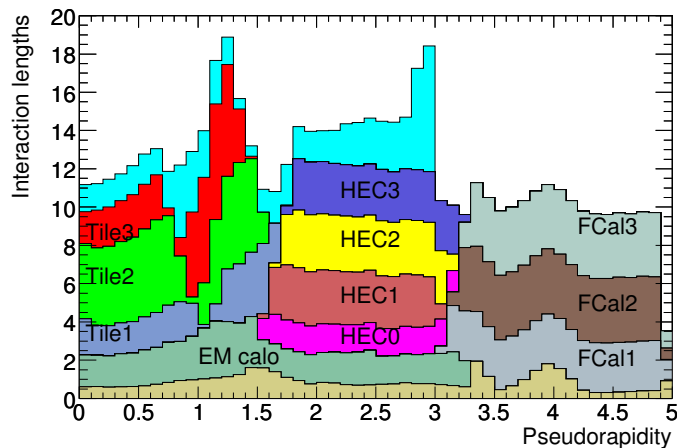
Figure 3.9.: Depth of the ATLAS calorimeter systems in interaction lengths. The light blue area represents the additional material between the calorimeter and the muon spectrometer up to $|\eta| < 3$.

and a scintillation based technology in the barrel region. The combined depth of the various calorimeter systems is greater than 10 interaction lengths (λ) over the entire η range of the calorimeter (fig 3.9).

The granularity of calorimeter cells is designed to match the physics requirements of the η region those cells occupy. The region $|\eta| < 2.5$ makes high precision measurements for identification of individual particles. This region is also covered by the inner detector. The cells being designed to give information which can be used in conjunction with inner tracks to determine particle properties. The calorimeter also provides coverage at a lower granularity up to $|\eta| < 4.9$. While there is not always enough spacial resolution to distinguish individual particles, the near total coverage allows accurate calculation of the total transverse energy of an event.

The electromagnetic calorimeter

The electromagnetic (EM) calorimeter is a sampling calorimeter, which uses liquid argon as the ionisation medium, lead plates for absorption and copper sheets for signal readout. Light particles interacting via the electromagnetic force, i.e. electrons and photons, lose energy quickly when entering the calorimeter. As they initially enter, the electron shower they cause is relatively narrow, widening as the particle and its products move through the detector. The EM calorimeter is divided into 3 layers of decreasing granularity with increasing distance from the interaction point to measure the energy of particles with these characteristics.
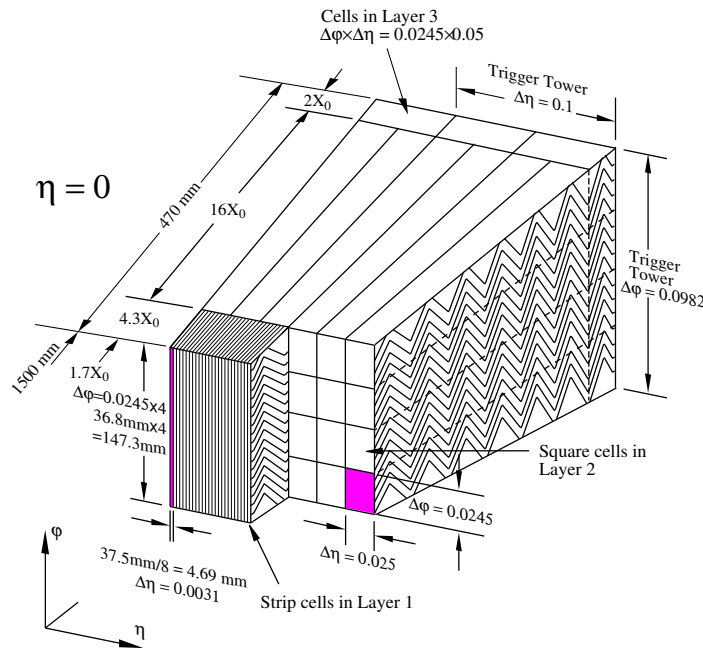

Figure 3.10.: An ATLAS electromagnetic calorimeter barrel module, the accordion structure over the three layers of differing granularity can be seen

The EM calorimeter has a depth of > 22 radiation lengths (X_0) across its entire η range, which corresponds to around 2 of the 10 interaction lengths (λ) of the whole calorimeter system. This depth of the EM calorimeter means that lighter particles are reliably stopped, while heavier particles will tend to continue through into the hadronic calorimeter. The thickness of absorption layers varies, generally becoming thinner with increased depth along lines in η, This keeps the effective absorption depth similar over the entire η range despite the cylindrical geometry of the detector. In total, the EM calorimeter covers the range $|\eta| < 3.2$. Further electromagnetic calorimetry information is provided up to $|\eta| < 4.9$ by the forward calorimeter.

The readout and absorption layers in the EM calorimeter are stacked in an accordion pattern around the ϕ-axis with liquid argon filling gaps maintained between the layers. This structure gives total coverage in ϕ as there is no path through the calorimeter that does not continually cross over multiple electrode layers.

The readout sheets are segmented along η so that a collection of neighbouring segments in stacked layers gives a calorimeter cell in η and ϕ (fig. 3.10). There are three layers of electromagnetic calorimeter in both the barrel and the endcap. The innermost layer has very fine η segmentation but its cells are relatively long in ϕ. The second and third layer have higher ϕ granularity, but much less segmentation in η. The lead absorption plates are not segmented and are sandwiched with thin steel sheets to provide support to the segmented readout layers.

The readout layers are comprised of 3 copper sheets separated by layers of insulating polyimide sheets. The outer copper layers are held at a high voltage. A signal is induced in the central layer when electrons are absorbed into the outer layers through capacitive coupling. The magnitude of the signal for a group of layered segments allows the calorimeter to measure the amount of energy deposited in that calorimeter cell.

The hadronic tile calorimeter

The tile calorimeter is arranged into two adjacent barrel regions and extended barrel regions on either side to further its coverage ($|\eta| < 1.7$ in total). It does not have an endcap region.

The detector is designed to make high granularity measurements and to reliably stop strongly interacting particles. It does this using modules formed from solid steel blocks interspersed with a staggered pattern of 3mm thick scintillating tiles at a steel to scintillator ratio of approximately $4.7 : 1$ in depth (fig. 3.11a). There are 64 modules arranged in ϕ in each barrel and extended barrel section; each module collects signals independently of the others.

Ionising particles passing through the steel will create showers of electrons which, when interacting with the scintillator tiles, generate photons. The scintillator tiles are inside a plastic sleeve which increases reflectivity back into the tile except on either side of the steel block, where they are connected to optical fibres. Many of the generated

(a)

(b)
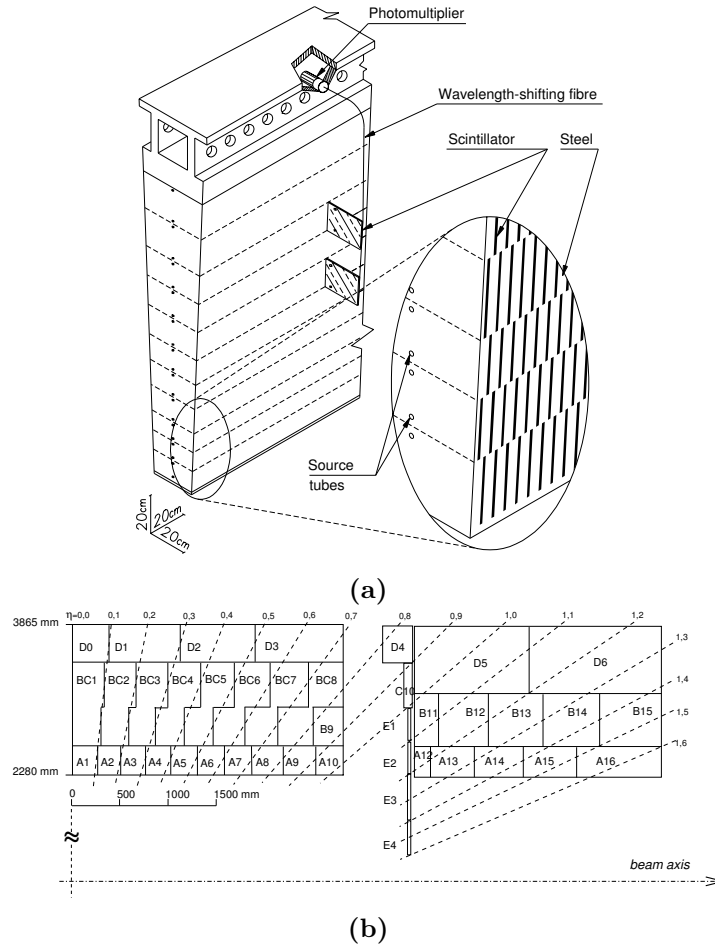
Figure 3.11.: An ATLAS tile calorimeter module. (a) 3D representation of an individual module, support girder at the top holds the electronics, source tubes into which radioactive sources can be inserted for calibration are also shown. (b) shows the cell segmentation in the barrel and extended barrel on one side of the detector in the rz-plane.

photons will pass into the two optical fibres on either side of the tile and travel to the two photomultiplier tubes (PMT) connected to them, resulting in an electrical signal. Each tile is connected to two separate PMTs for redundancy and the fibre grouping forms the scintillator tiles into effective calorimeter cells of approximate size $\Delta\eta = 0.1$ for the inner 2 layers and $\Delta\eta = 0.2$ for the outer layer. The resulting segmentation of tile calorimeter cells is shown in figure 3.11b.

The hadronic endcap calorimeter

The hadronic endcap calorimeter (HEC) is a liquid argon sampling calorimeter covering the endcap range $1.5 < |\eta| < 3.2$. Similar to the EM calorimeter it uses the liquid argon

as a ionization medium and picks up signals on copper readouts; the detector geometry however is very different.
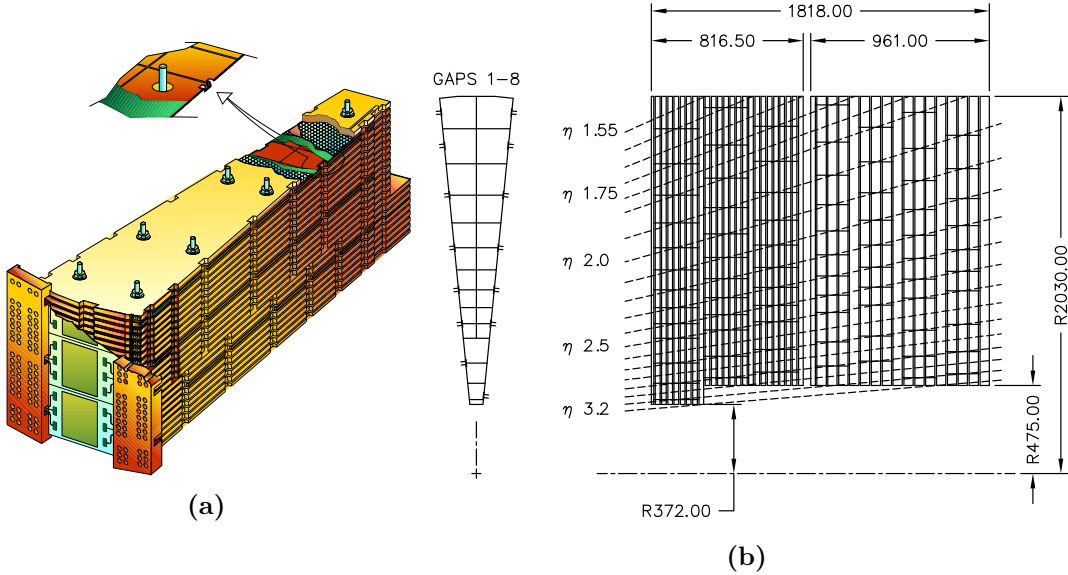
Figure 3.12.: The hadronic endcap calorimeter

The HEC uses a flat plate design with all elements perpendicular to the z-axis (fig. 3.12b). Grounded copper plates provide the absorption medium and segmented copper sheets act as readouts, which is shown in the cutaway section in figure 3.12a. The readouts have granularity of approximately $\Delta\eta = 0.1$, $\Delta\phi = 0.1$ at $\eta < 2.5$ and cells of double that size for $\eta > 2.5$. They are separated from the plates by a honeycomb structure, and sandwiched between insulating layers and high voltage layers. The gaps in the honeycomb structure are filled with liquid argon. Electrons liberated from the argon collect on the high voltage layers and induce a signal in the readout segment, which is amplified by electronics on the outer edge of the module.

The segment layers are grouped together into cells and the cells arranged to approximately follow a distribution constant in η (fig. 3.12b). The HEC detectors are split into two wheels. The inner has three layers of cells with thin absorption plates for making fine measurements of the deposited energy. The outer has four layers of cells with thicker plates and makes courser measurements.

The forward calorimeters

The forward calorimeters (FCal) is another liquid argon sampling calorimeter, covering the high η endcap range $3.1 < |\eta| < 4.9$. The high particle fluxes through this region of the detector necessitate a different design to the rest of the endcap with thinner liquid argon gaps reducing the electron drift time. This prevents signals from piling up, rendering the detector unable to distinguish individual energy depositions. Since the

main electromagnetic calorimeter system does not extend past $|\eta| = 3.2$, the first layer of the forward calorimeter (FCal1) is tasked with making electromagnetic measurements, while the following two layers (FCal2&3) make hadronic measurements.

(a)   **(b)**   **(c)**
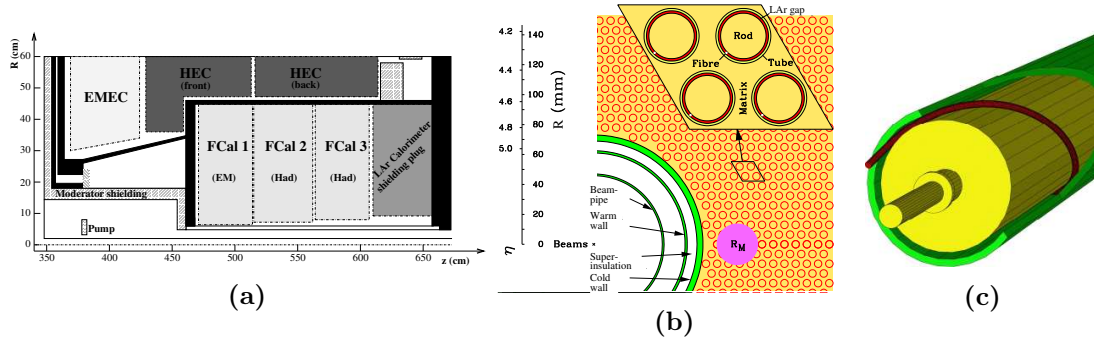
Figure 3.13.: The hadronic endcap calorimeter. (a) The calorimeter layer positions in relation to the EM calorimeter endcap and the HEC in the rz-plane. (b) The FCal calorimeter in the xy-plane. (c) A 3D representation of the fibre separating the rod and tube sections.

(a)   **(b)**
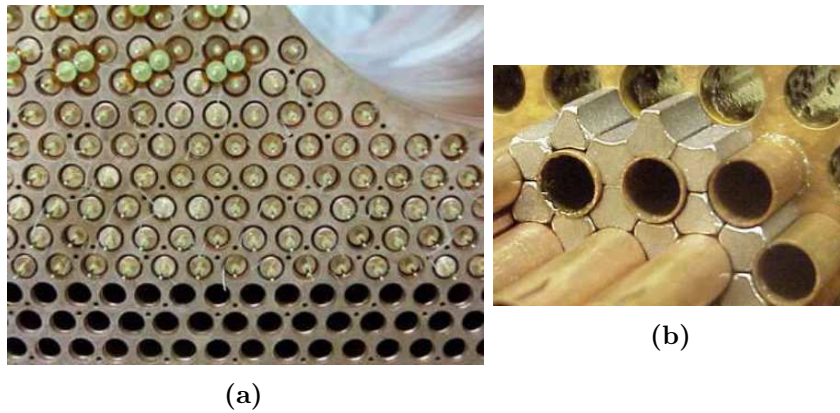
Figure 3.14.: Photographs of the hadronic calorimeter systems. (a)Front view of FCal1, the beam pipe occupies the space to the top left. (b) Example of the FCal2&3 absorption slug structure.

All layers of the FCal share a similar structure, the bulk of the detector is absorption material perforated with holes that house the liquid argon gaps and electrodes. Each electrode consists of a rod held at high voltage surrounded by a grounded tube separated by an insulating fibre loosely wound around the tube (fig 3.13c).

The gaps maintained between rod and tube are different in the different FCal layers to adjust for the varying amount of energy likely to be deposited in them. FCal1 has the thinnest to deal with the high deposition from electrons and photons, FCal2 has around 50% larger gaps and FCal3 around 100%, however even the gaps in FCal3 gaps are less than a quarter the width of those used in the other calorimeter systems. To increase

the measurement accuracy in FCal1, copper is used as the absorption material, with stacked plates through which the electrode assemblies are threaded (fig 3.14a). FCal2 and FCal3 are designed with more of a view to contain particle showers and stop particles as effectively as possible, as such the absorption is done using tungsten slugs stacked between the electrode tubes (fig. 3.14b).

After the FCal layers, a plug of solid copper limits particles punching through into the muon system; no measurements are made of the energy deposited in this plug.

Time and energy measurements in the calorimeter

This study makes use of time measurements produced by the ATLAS calorimeter system. The ATLAS calorimeters need to have good response times in order to successfully estimate deposited energy and associate it with the correct bunch crossing. This is achieved through pre-amplifier and signal shaping circuits that convert the signals received from readout electrodes into a pulse. The height of the pulse determines the deposited energy and starting time determines the time of arrival of the particle at the detector.

The liquid argon detectors' readout response can be approximated to saw tooth signals: a sudden induced current as electrons are liberated from the argon and begin to move towards the anode, followed by a linear decrease as electrons reach the electrode and stop. The length of this signal is determined by the width of the argon gap and the drift velocity, which can be considered constant across the gap. The argon gap width in the detectors varies, but drift time is of the order of 400ns for the ATLAS liquid argon detectors.

The tile calorimeter by comparison can be approximated to an fast (around 17ns width) impulse of signal, with width caused mainly by the time taken for all light generated to navigate the tiles and fibres to the PMTs. The PMTs themselves have rise times of a few ns, giving the tile calorimeters themselves a time resolution of the same order. The need for fast processing and importance of energy estimation over time measurements, however, means that much of this resolution is lost in the electronics following PMT.

The shaping circuits are designed to quickly manipulate signals from calorimeter readouts into a form from which accurate estimations of deposited energy can be drawn for each event. The readout signals themselves cannot be used because in liquid argon detectors the signal length extends over many bunch crossings and the signal height must be estimated in isolation from any energy already deposited in the cell. Representations of the signals output for each event by the shaping circuits are given in figure 3.15[2].

---

[2]The presampler response is also shown. The presampler is a thin calorimeter layer positioned in front of the EM calorimeter in order to provide an initial estimate of particle energy as it enters the calorimeters. It is not used in this study.
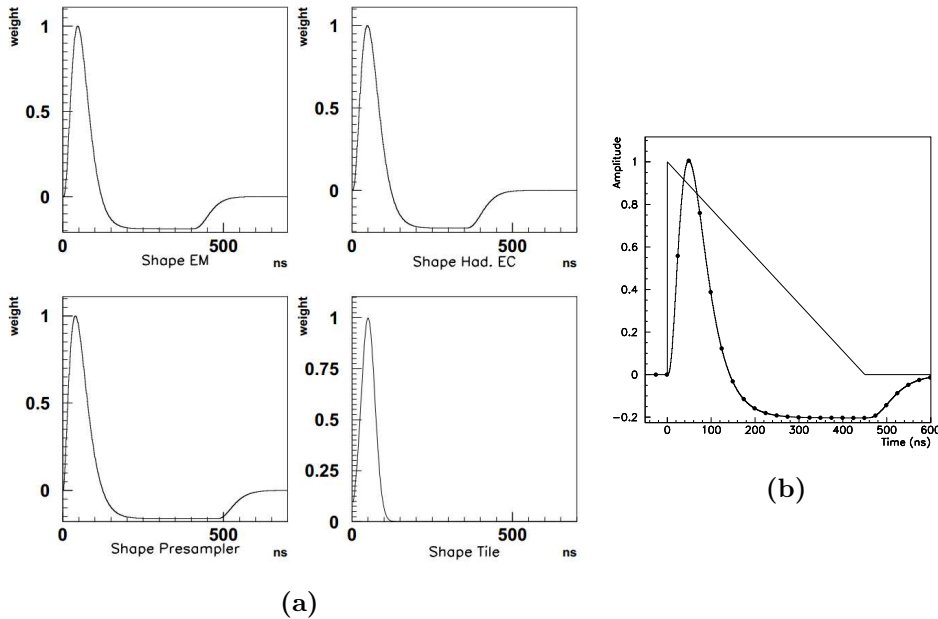
Figure 3.15.: Calorimeter signal shaping response functions. (a) Shaping functions for all calorimeter technologies[14]. (b) Triangular signal received at electrode superimposed on shaper response for EM-calorimeter.

These waveforms are sampled at 25ns intervals (typically 5 samples)[11] and the values are saved for further analysis.

The energy deposition measurements are made at a later stage by applying a fit to the sampled values, from which the peak value can be estimated. The peak value is proportional to the energy deposited, while time measurements can be made by calculating the "start" of the shaper response.

3.2.4. The muon spectrometer

The muon spectrometer is the outermost detector system at ATLAS, designed to detect muons and measure their momentum. With all other detectable Standard Model particles mostly stopped inside the calorimeter, the muon spectrometer has access to a relatively clean signal. High p_T muons are indicative of interaction events at high energy and, if identified quickly, can be used for triggering. This makes the leptonic decay channels of rare processes, such as the Higgs, especially appealing for analysis.

The muon spectrometer estimates the momentum of muons by measuring the bending of their tracks inside the magnetic fields generated by the three toroidal magnet systems at ATLAS. The magnet systems and the muon detector layout around them are visible in figure 3.16. The magnetic fields generated circle the detector in ϕ with near uniformity, making muon tracks bend almost entirely in the rz-plane once inside the spectrometer.
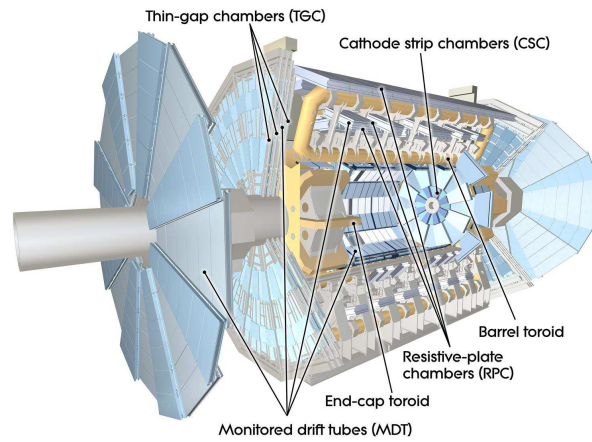
Figure 3.16.: 3D representation of the ATLAS muon spectrometer system

The muon spectrometer covers both the endcap and barrel regions of the detector with several groups of layers, called "stations". In the endcap region, the inner-station is placed in front of the toroidal magnet, the mid-station behind it and the outer-station approximately 7m behind that. In the barrel the inner-station sits in front of the toroid, the mid-station inside and the outer-station immediately outside the toroid. There is also the smaller extended-station in the endcap, placed on the outer rim of the toroid. The stations are additionally split into "long" and "short" detector sections that overlap, as well as a few other less standard section types. The resulting notation for, e.g. a Barrel Midstation Long section is BML.
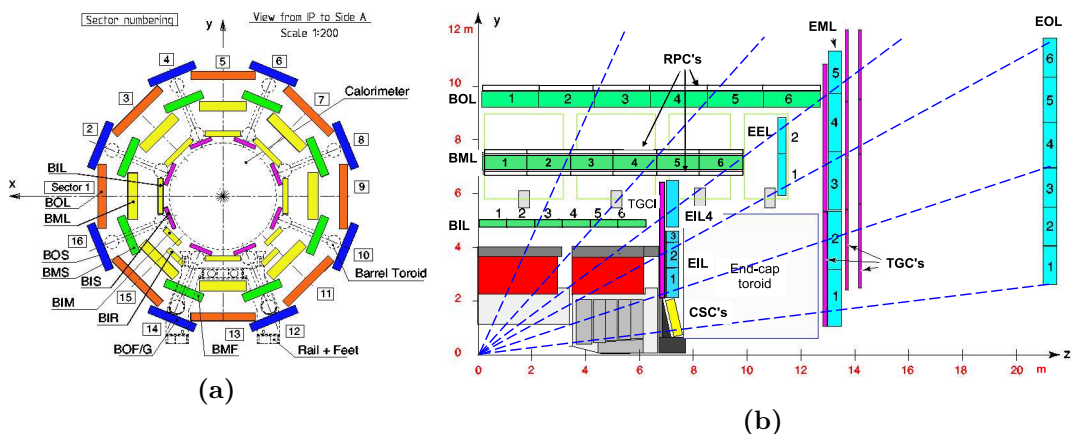
Figure 3.17.: ATLAS muon spectrometer stations in (a) the barrel xy-plane (b) the barrel and endcap rz-plane.

This section is concerned with describing the way in which the detectors function and make individual measurements. A detailed description of the way in which tracks

are reconstructed from these measurements can be found in section 5.2.2. The trigger methodology is also briefly discussed in section 3.2.5.

There are four distinct detector technologies in the muon spectrometer, which can be split into two categories

- **Precision detectors** make accurate measurements of the path of a particle, but do not have fast response times. They are mainly required to make high precision measurements in the rz-plane to measure any bending of the track and hence accurately estimate the particle momentum. Precision in ϕ is a secondary concern for the majority of the detector.

    - **Monitored Drift Tubes (MDT)** cover the range $|\eta| < 2.7$ for most stations. MDT measurements cannot be used without being reconstructed into a track and can only provide accurate positional information in the rz-plane. In the rz-plane though, the MDT has the highest positional measurement accuracy of all the muon detectors.

   - **Cathode Strip Chambers (CSC)** cover the range $2.0 < |\eta| < 2.7$ in the innermost muon detector stations. These regions experience too high a particle flux for the MDT. The CSC makes fairly accurate measurements of both track η and ϕ as there is no overlapping trigger layer in the same station.

- **Trigger detectors** make less accurate positional measurements but have fast time responses to quickly identify muon tracks and make a first estimation of their momentum. They also provide a ϕ measurement to complement the rz-plane measurements of the MDT in building 3D tracks.

    - **Thin Gap Chambers (TGC)** cover the endcap range $1.05 < |\eta| < 2.7$ and have sufficient time resolution to reliably associate muon tracks with the correct bunch crossing, whilst having sufficient radiation hardness for that region.

    - **Resistive Plate Chambers (RPC)** cover the barrel range $|\eta| < 1.05$ and have excellent time resolution.

Monitored Drift Tubes

The MDT is the main precision muon detector and uses stacked layers of 3cm diameter aluminium drift tubes to track charged particles throughout the muon spectrometer. The tubes are filled with an ionizing gas mixture and have a wire running down the centre held at a 3000V potential that acts as the pickup. Any electrons liberated from the gas will drift towards the wire and generate a current, picked up by the electronics connected to one end of the wire. An MDT module consists of two sets of 3 or 4 layers of tubes stacked on either side of spacer structures (fig. 3.18a). MDT modules are present in

every muon station, with the small and large stations designed to slightly overlap for full coverage. Every muon track reconstructed has the majority of its measurements made by the MDT.

(a)

(b)

(c)
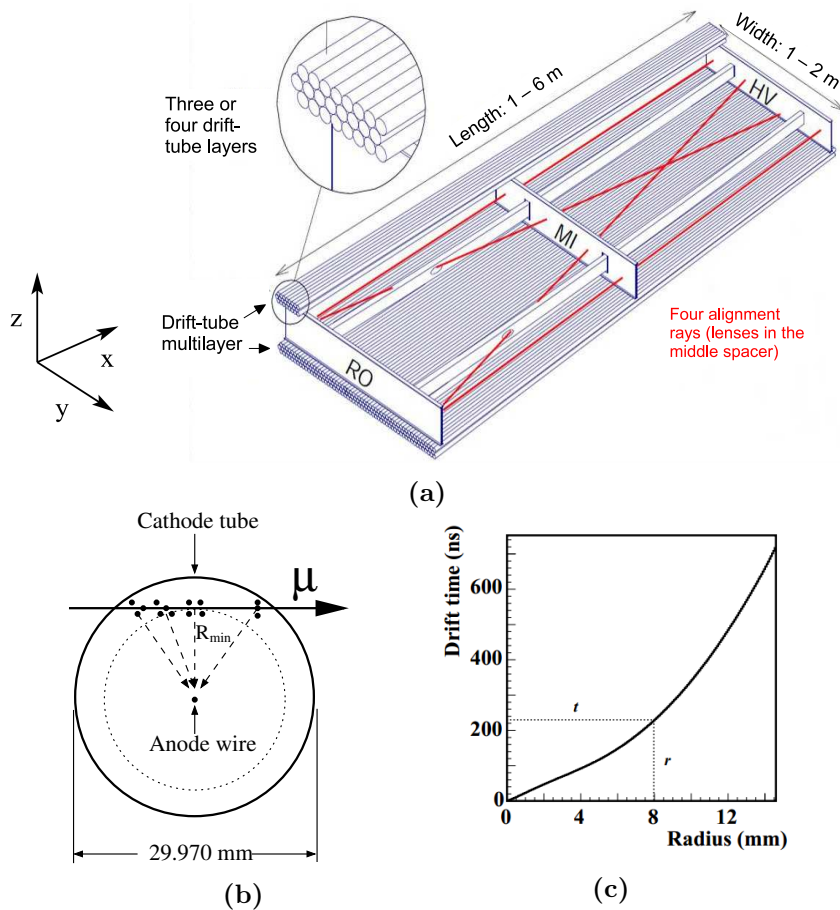
Figure 3.18.: (a) Schematic of an MDT module with local coordinate system. (b) Cross section of a single tube showing drift circle of a passing muon track. (c) Relationship between drift circle radius and electron drift time.

The MDT detectors makes precision measurements for the entire barrel region and the majority of the endcap. Only the high η region of the inner station, where the flux is expected to exceed the safe operational counting rate for the MDT of 150Hz/cm, is not covered, although the same η range can be safely covered in the other two stations. Tubes in both the barrel and endcap regions are aligned with the ϕ axis at their centre to make accurate measurements in the rz-plane. Their resolution in ϕ is determined by the tube length and is, as such, limited.

The muon track liberates electrodes along its path through the MDT tube (fig. 3.18b). Electrons drift towards the pickup wire, with those liberated at the minimum radial distance reaching it first, producing the signal. The relationship (fig. 3.18c) between drift time and drift radius is not linear mainly due to the radial nature of the electric field.

The drift radius is not initially known; the drift time can be calculated by subtracting the muon time of flight (ToF) for the current bunch crossing from the signal arrival time. Since all muons reaching the muon spectrometer will have velocities of negligible difference to the speed of light, the ToF is known to be

$$t_{ToF} = \frac{d_{tube}}{c} + t_{bc} \tag{3.4}$$

where d_{tube} is the distance of the tube from the interaction point and t_{bc} is the bunch crossing time.

The radius at which electrons were liberated nearest to the pickup can be calculated from the drift time. Calculation of the radius results in drift circles being reconstructed for each tube a muon traverses. By combining the drift circles produced, an accurate reconstruction of muon trajectory through the MDT layers can be made. The positional accuracy of an MDT tube measurement after reconstruction is expected to be approximately 80μm.

Cathode Strip Chambers

The CSCs are precision detectors designed for the high flux environment of the high η region of the inner station. They consist of gas chambers with anode wires running through them parallel to the r-axis at the centre of the chamber. The walls of the chamber are lined with cathode strips, perpendicular to the wires on one wall of the chamber, parallel on the other. The two cathode strips are connected to readouts and have signals induced on them when electrons are liberated from the gas. The two opposing strip layouts enable the CSCs to make measurements of both track η and ϕ. Each CSC module has four chamber layers. The modules are arranged in an overlapping structure for full coverage in ϕ (fig. 3.19a) in the η region $2.0 < |\eta| < 2.7$ of the inner station.

The η-measuring strips are around 1.5mm in width and separated by 0.25mm gaps and have a measurement accuracy of approximately 60μm in the rz-plane. However, segmentation in the opposing plane is much coarser, leading to a measurement accuracy of approximately 5mm. The CSC achieves its high precision by measuring the relative charges between strips. Typically between 3 and 5 strips are used by the electronics to fit the charge distribution, the peak of which gives the position measurement (fig. 3.19c).

The drift time of a CSC chamber is generally less than 40ns, resulting in a designed timing resolution of around 7ns for the whole system. There is an issue, however, with the time resolution of detectors using planes of wire anodes. The electric field is radially distributed around the wires, but becomes vanishingly small in the spaces equidistant between two wires. This causes long electron drift times in those areas, leading to late arrival of measurements relative to their bunch crossing. For the purpose of associating hits with bunch crossings in the CSC, this was overcome by OR-ing the hits occupying the same η-ϕ region in adjacent layers. The CSCs are oriented such that tracks are unlikely to pass through the equidistant regions in all four CSC layers.

(a)

(b)

(c)
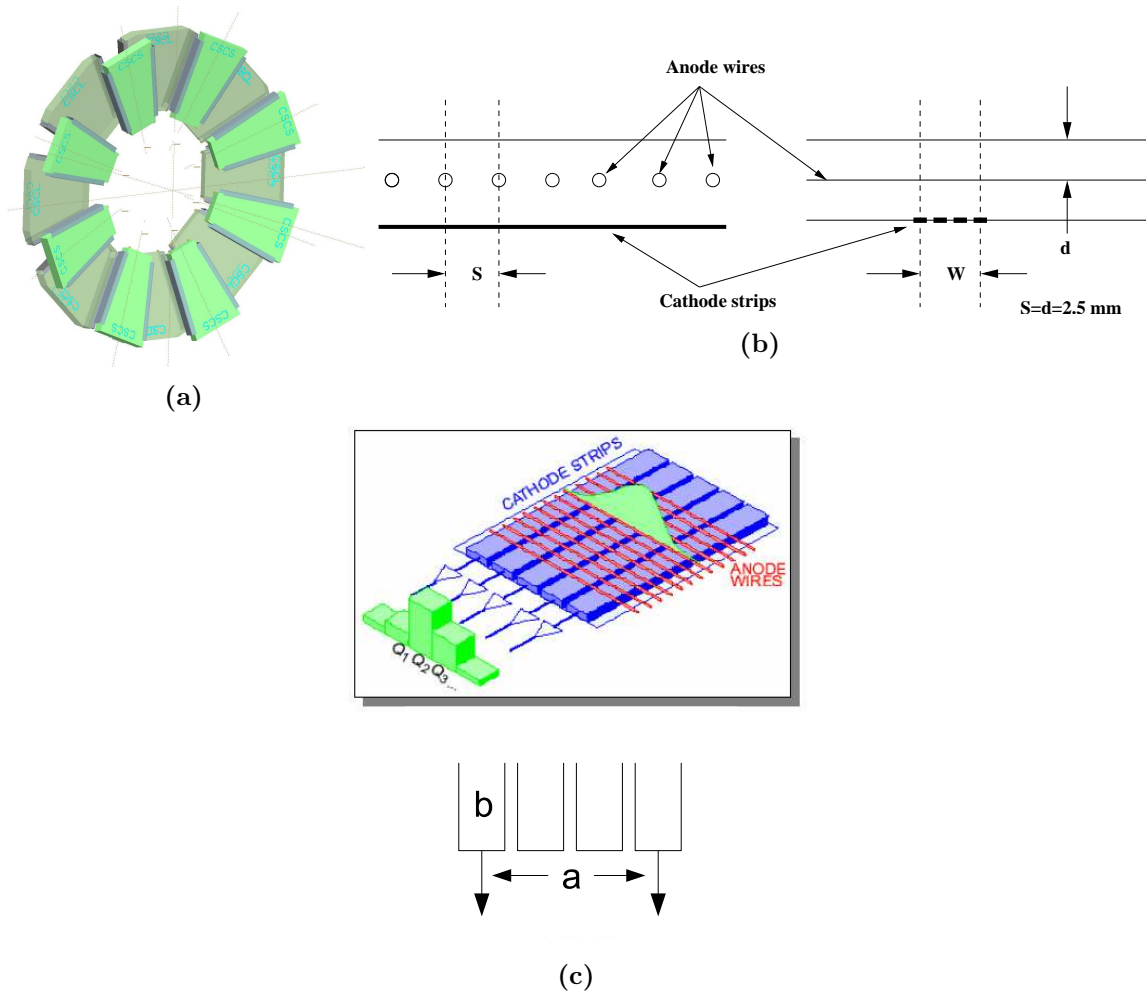
Figure 3.19.: CSC structure and readout method. (a) Geometry of the individual chambers. Unlike all other chambers they are set at a slight inclination towards the interaction point. (b) Cross section of a chamber along the strip axis (left) and the wire axis (right). (c) Charge distribution across wires and resulting charge induced in strips nearest to those wires, strip pitch $a \approx 5.5$mm, strip width $b \approx 1.5$mm.

Thin Gap Chambers

The TGCs are the trigger detectors used in the endcap region. They provide muon triggering signals in the $1.05 < |\eta| < 2.4$ region and provide additional ϕ measurements for track building up to $|\eta| < 2.7$. Figure 3.20b shows the cross section of a TGC chamber. Most chambers[3] have pickup strips on one side running parallel to the r-axis through the centre of the chamber and wires held at high voltage running perpendicular to them across the chamber. The pickups are separated from the cathode by an insulating layer and have current induced when electrons are liberated from the gas. The opposing wall

---

[3]The middle layer of the triplet has no pickup strips, only wires

of the chambers have no pickups. Unlike the CSCs, the wires are also connected to detection electronics, allowing then to be used to make measurements in the rz-plane.
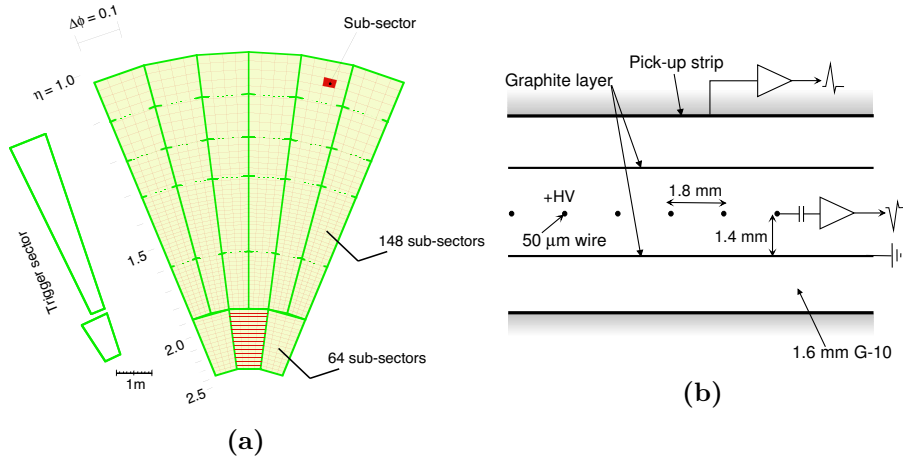
Figure 3.20.: The TGC structure. (a) TGC mid-station layout in the xy-plane. (b) Cross section of a single TGC layer along the strip axis.

There are two TGC layers in the inner-station and seven in the mid-station, while no TGC layers are present in the outer-station. Figure 3.23a in section 3.2.5 shows the layout of the TGC layers. The TGC layers are sandwiched together in groups of two (doublets) or three (triplets). The inner-station has a single doublet, while the mid-station has one triplet before the MDT modules and two doublets after. The TGC is not split into small and large sections and as such cannot follow the same station naming scheme as the MDT. The mid-station triplet and doublets are designated M1, M2 and M3 in increasing distance from the interaction point, the inner-station doublet is known as the EIFI[4].

Despite the difference in layout, the TGC is designed to cover the same η and ϕ space as the MDT in the two MDT stations it occupies (fig. 3.20a). The large number of layers used gives it high efficiency in detecting muon tracks and its time resolution is sufficient to assign muons to the correct bunch crossing. The spacial resolution is not as fine as the MDT or CSC systems, but has been designed to be sufficient to provide a coarse measurement of muon momentum for triggering.

The TGC suffers from the same problem with drift time uncertainty as the CSC, with the wire electrode planes leading to late measurements. Nevertheless 99% of measurements arrive within the bunch crossing time window of 25ns, which, given the number of layers, does not significantly impact trigger performance.

---

[4]Endcap Inner, Forward Inner

Resistive Plate Chambers

The RPCs are the trigger detectors used in the barrel region, providing triggering and ϕ measurements over $|\eta| < 1.05$. Figure 3.21b shows a cross section of two RPC modules and the way in which they intersect to form a chamber. Each RPC module consists of two gas gaps with pickup strips in the ϕ direction on one side of the gap and the z direction on the other. Unlike the TGC and CSC there are no anode wires. The walls of the chamber are composed of graphite electrodes which act as the anode on one side and the cathode on the other. The pickup strips are separated from the anode and cathode layers by an insulating foil and have signals induced by capacitive coupling. The layers with no gas gaps and the intermediate structure between gas gaps is filled with a paper honeycomb structure that has little to no effect on tracks passing through the detector.

(a)   (b)
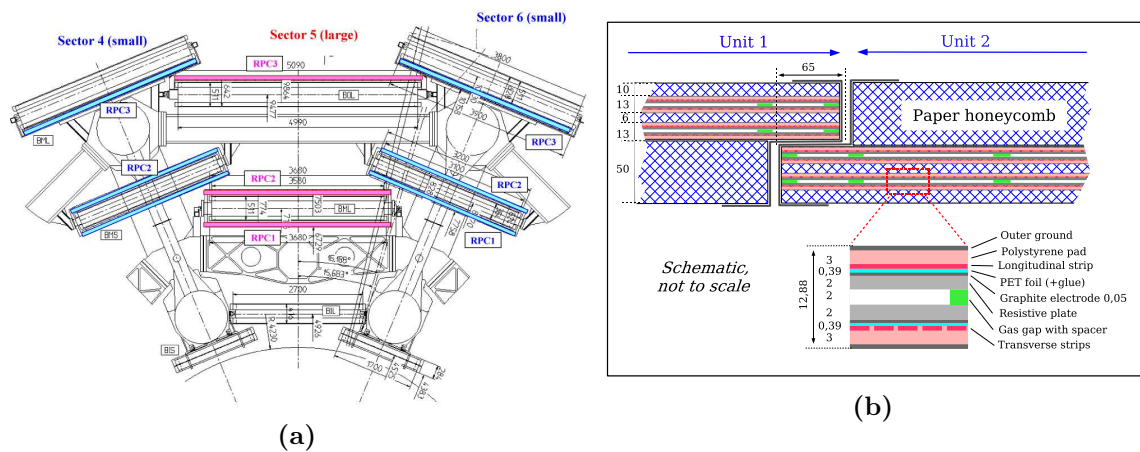
Figure 3.21.: The RPC structure. (a) Layout of RPC modules (coloured) in relation to the MDT and toroid. (b) Cross section through an RPC chamber, showing the intersection between modules.

Figure 3.21a shows the layout of the RPC modules in relation to the barrel toroid and MDT modules. Two RPC modules are present in the barrel midstation sections, one on either side of the MDT. One module is present in the outer-station on the outer side of the large sections and the inner side of the small sections to give a relatively consistent distance position in r. No RPC modules are present in the inner-stations. This layout, and the opposing strip structure of the RPC allows six independent measurements of both track η and ϕ to be made for each muon passing through the barrel region. Similar to the TGC, the spatial precision is relatively coarse, but sufficient to estimate muon momentum in the trigger system. The time resolution of the RPC however is excellent due to its uniform electric field and short drift time (5ns). The main constraint is the readout electronics, which only sample at a 3.25ns rate.

Time measurements in the muon spectrometer

The muon spectrometers are designed to make positional measurements, with the triggering detectors having enough immediate time resolution to be used by the L1 trigger (see section 3.2.5) and to correctly associate muons with events. Time measurements corresponding to the beginning and end of a signal pulse are recorded for each measurement with a sampling speed of order several ns. Unlike in the calorimeter, there is no requirement to measure pulse height and little problem with signal pile-up due to the comparatively low flux of particles. As such, the time measurement can be made by simply monitoring the amplifier outputs for voltage above an appropriate threshold.

Of the four detectors in the ATLAS muon spectrometer, only the MDT and RPC are used in this study to measure particle velocity. The CSC may produce usable time measurements with appropriate calibration, but this was not undertaken for this study because of the low production rate of GMSB events in high $|\eta|$ regions. The TGC does not have sufficient time resolution to be used in making velocity measurements.

Time resolution for the purposes of triggering and for the purposes of velocity measurement after event reconstruction are somewhat different. For muon L1 triggering (section 3.2.5) the signal must be detected within a small time window ($\approx$ 25ns) for each bunch crossing to correctly associate measurements to events. No detailed reconstruction takes place during the L1 trigger, so any uncertainty in the drift time of electrons and signal propagation time along electrodes must be within this time window. The TGC then has sufficient time resolution for triggering, whereas the MDT, with a 400ns drift time, does not. After reconstruction, however, the position of the track relative to electrodes is known and most drift and propagation times can be accounted for. Since the MDT has no region with vanishingly small drift fields, the relationship between track position and drift time is straightforward. For the TGC, however, the vanishingly small drift field region between the wires leads to a much larger uncertainty in drift time than for of the MDT. In reconstruction then, while the MDT measurements typically have a time resolution of order several ns, the TGC measurements still have resolution of order 20ns.

The RPC, since it does not use wires, has a fairly uniform drift field, resulting in fast signal. Using strips, through which particles pass directly, as opposed to wires, also results in an almost immediate signal induction. The RPC detector thus has an intrinsic time resolution of less than 1.5ns, but is limited by the readout electronics to be of order several ns.

3.2.5. Triggers

The bunch crossing rate at ATLAS is 40MHz. The event rate this causes varies statistically and depends on the luminosity of the LHC, but is of order 1GHz. The resulting data rate is too large for any current computing system to handle in its entirety and is mostly composed of events of no interest in terms of physics. The ATLAS trigger system is

designed to identify events with interesting properties and bring the data rate down to a more manageable event rate of 200Hz.

The trigger system has three successive levels, L1, L2 and the Event Filter (EF); each performing successive refining of events passing the preceding level. The L1 trigger reduces the rate from 40MHz to approximately 75kHz, the L2 reduces this to around 3.5kHz and the Event Filter finally reduces the resulting event rate to 200Hz. All event data must be buffered in an intermediary storage until the event is rejected by one of the trigger levels or it passes the levels. This takes approximately $2.5\mu s$ for the L1, 40ms for the L2 and around 4s for the Event Filter. If rejected, an event's data is deleted and the buffer made available for new event data. If an event passes the Event Filter, it is written to the output streams and saved for analysis.

The low latency requirement of the L1 trigger necessitates a low granularity analysis performed entirely at a hardware level. It uses custom circuits specifically designed to make fast decisions about the characteristics of events. The L1 electronics is split between being physically mounted on the detector and being located off detector in the USA15 cavern, which is adjacent to the cavern containing ATLAS. The L2 trigger and EF (collectively known as the High Level Trigger (HLT)) are implemented in software using standard computer hardware. They make more refined decisions than the L1 trigger and have access to more detailed detector information. The HLT is located outside of the cavern structure, on the surface.

The L1 trigger quickly searches for signals of interest and form Regions of Interest (ROI) around any signals detected. The L1 trigger only uses information from the muon spectrometer and the calorimeter; inner detector reconstruction is not performed in the L1 trigger. All data collected in the ROI is then passed on to the L2 trigger. The L2 trigger performs a more thorough analysis of data in the ROI and if passed, the data for the entire event is passed into the Event Filter, which makes the final decision. Figure 3.22 shows the separation of processes involved in the trigger and how data is buffered and passed between them.

Each trigger method has multiple thresholds set, resulting in tighter and looser versions of the same trigger. The necessary reduction of the data rate is balanced against sensitivity by selecting appropriate thresholds. Multiple loose triggers, which alone do not sufficiently reduce the event rate, can be combined into a single composite trigger that has appropriate rate attenuation. These combined triggers may give better sensitivity for some analyses than the tighter individual triggers. Looser triggers may still be used alone to collect events, mainly to monitor the trigger performance, but the rate at which these events are collected must be artificially reduced by a constant factor (the prescale).

Each trigger has a unique name associated with it, denoting the trigger level passed, the trigger type and the threshold. The single muon and missing E_T triggers are of interest to this study and will be discussed in the following sections. Their trigger type strings are "mu" and "xe", respectively. For instance, the $p_T > 18$GeV threshold single muon trigger in the Event Filter is named EF_mu18 with variations EF_mu18_MG, EF_mu18_medium & EF_mu18_MG_medium. There are also slight variations in the

trigger algorithms that can be denoted by a combination of strings after the trigger type and threshold, which typically denote different track quality requirements.

There exist many other trigger types in the muon spectrometer and calorimeter, as well as various combinations of trigger criteria from both. These are not used in this study and will not be discussed.

Single muon triggers

The single muon trigger filters events to find those containing muon signals with p_T above a certain threshold. The thresholds range from approximately 6 to 35GeV, with 18GeV being the lowest unprescaled trigger threshold for 2011.

The L1 muon trigger identifies muon-like signals by searching for coincidences of hits in the trigger detector stations. This is done using coincidence windows which are pre-defined windows representing deviation in the xy-plane from an infinite momentum track. The chambers are split into Regions Of Interest (ROI), each with a different set of coincidence windows. Different windows are required for each ROI because of the
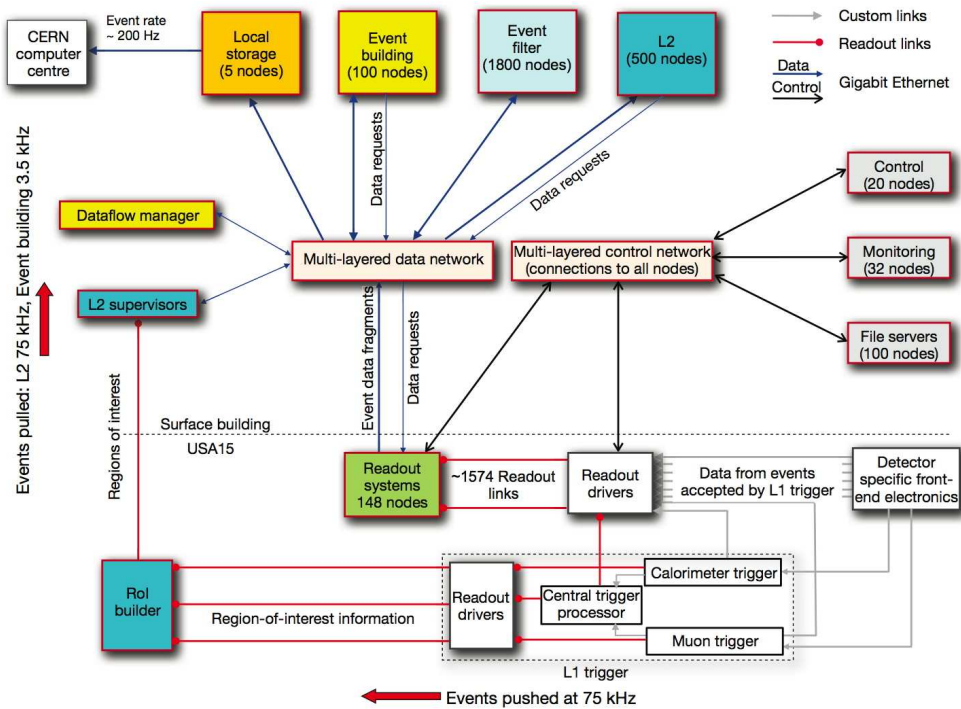

Figure 3.22.: Block diagram of the ATLAS trigger and data acquisition system, final readout is in the top left
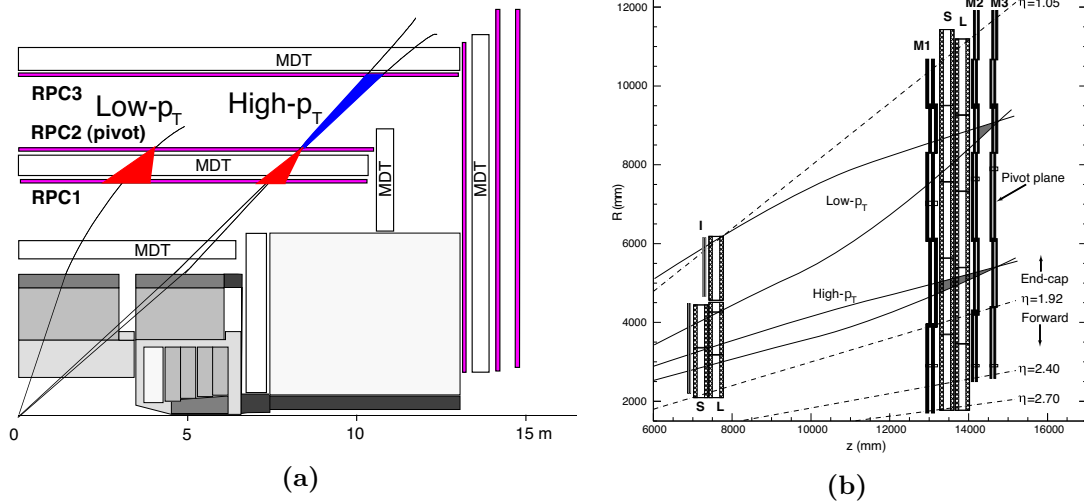
Figure 3.23.: The single muon trigger

differing cumulative magnetic field strength passed through, and the different detector plane angle relative to the track. There are five window sizes defined for each ROI, each representing a different momentum threshold.

The L1 algorithm starts by searching for signals from detector elements in the RPC and TGC layers designated as pivot planes (fig. 3.23). Coinciding hits are then searched for on the preceding station inside the appropriate window, centred on a projection of the pivot hit location onto the plane of that station. This is performed simultaneously in η and ϕ for the RPC, while the TGC treats η and ϕ measuring hits separately until the last stage. The L1 low-p_T trigger is passed if sufficient hits are found in the preceding station. The L1 high-p_T trigger is passed if hits matching the low-p_T trigger are found in the remaining station, where a tighter window is used. The "Sector Logic" (SL) trigger combines the results of the low-p_T and high-p_T triggers. The TGC SL trigger requires the coincidence of η and ϕ triggers. The results of the triggers for all thresholds are then sent to the L2 trigger electronics for further analysis.

The L2 and EF triggers perform a more thorough reconstruction of the event using measurements from the precision as well as trigger detectors. The exact procedure applied for triggering is beyond the scope of this study. However, muon reconstruction for analysis is described in detail in section 5.2.

Missing E_T (E_T^{miss}) triggers

The E_T^{miss} trigger finds events which have more energy deposited in the calorimeter in one direction than the opposing direction. This can be the result of either especially high energy deposition in one direction, or of especially low energy deposition in one direction. The number after "xe" in the trigger name denotes the threshold used by the trigger

The trigger can be used to search for especially high energy particles that are not stopped by the calorimeter. Single high energy muons or neutrinos can be indications of interesting physics and, if produced in the transverse plane, are likely to leave a missing E_T signature.

Missing E_T is found in the L1 trigger by separating the calorimeters into towers (collections of cells of relatively constant η and ϕ) and summing the energy estimated to be deposited. Since each tower is at a known angle to the nominal interaction point and energy deposited in the various towers can quickly be converted energy along the x and y-planes (E_x and E_y). The values for E_x and E_y are summed and combined into E_T^{miss}, which is checked against eight thresholds, each giving trigger results.

The L2 and EF triggers, again, perform a more thorough reconstruction of the event, which will not be covered in this study.

3.2.6. Data recording and data quality

After triggers have been applied, the event data passing the triggers must be saved onto servers where it is made available for further analysis. The data in each run is split into a number of "luminosity blocks" and can be spread over many files on different servers. The files can be accessed using the Grid, a worldwide network of such servers used by CERN.

ATLAS continues to take data in cases where non-critical parts of the detector fail. For any given analysis, there may be data taken during a time when necessary parts of the detector are not functioning to within the requirements of that analysis. There is a data quality (DQ) system in place at ATLAS which records any such detector faults. This data quality information is made available using the Good Run Lists.

Good Run List

Good Run Lists (GRLs) are xml files specifying which luminosity blocks contain data taken when ATLAS was performing to within required standards. Different types of analysis have different requirements, so there are several different types of GRL.

When running an analysis, it is simply necessary to filter the data being used to only contain events in luminosity blocks specified as 'Good' by the appropriate GRL.

Chapter 4.

Data

To conduct a search for SMPs we require a substantial amount of collision data from ATLAS. We also require simulations of events containing the particles being searched for and those likely to comprise the Standard Model background to the search.

This chapter aims to specify the data and simulation sources used and how events were pre-selected from ATLAS for analysis. The SMP datasets used, and model parameters from which they were generated are described in section 4.1. Simulation of expected Standard Model background processes is briefly explained in section 4.2. Finally, the triggers and datastreams used to select events in data are described in section 4.3.

4.1. SMP Monte Carlo simulation

Datasets for GMSB models producing pairs of long lived $\tilde{\tau}$s have been generated using HERWIG[28] for proton-proton collisions at 7TeV.

Λ	$\tan\beta = 5$	$\tan\beta = 10$	$\tan\beta = 30$
50	161	158	122
60	191	188	153
70	221	218	183
80	251	249	212
90	282		241
100	312	309	269
120	373	370	326
130	404	401	355
140			383
150	465	462	411

Table 4.1.: $\tilde{\tau}$ masses (GeV) generated in models with GMSB parameters $\tan\beta$ and Λs, blank spaces represent unavailable datasets.

The datasets were generated with GMSB parameters $N_5 = 3$, $m_{messenger} = 250\text{TeV}$, the sign of the Higgsino mass parameter sign $(\mu) = 1$ and the gravitino mass scale factor

47

$C_{grav} = 5000$. Λ and $\tan\beta$ were varied, giving masses of the primary $\widetilde{\tau}$ shown in table 4.1.

4.1.1. SMP Monte Carlo event properties

GMSB SUSY particles will quickly decay into pairs of $\widetilde{\tau}$ particles. SM particles are also produced but the precise Standard Model content of a GMSB event depends on the decay pathways in that event.

Figure 4.1 shows the number of muons and neutrinos in events from the GMSB $\Lambda = 100$, $\tan\beta = 10$ dataset. Events without neutrino production are rare. Muons are a common event product, but a significant number of events occur with no muon production.
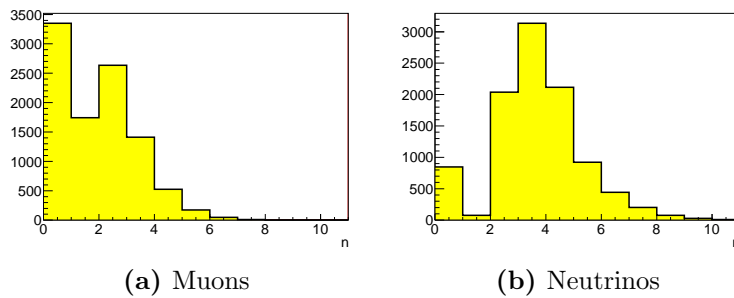
(a) Muons   **(b)** Neutrinos

Figure 4.1.: Number of (a) muons and (b) neutrinos in GMSB_100_10 dataset.

(a) Muons   **(b)** Neutrinos   **(c)** $\widetilde{\tau}$
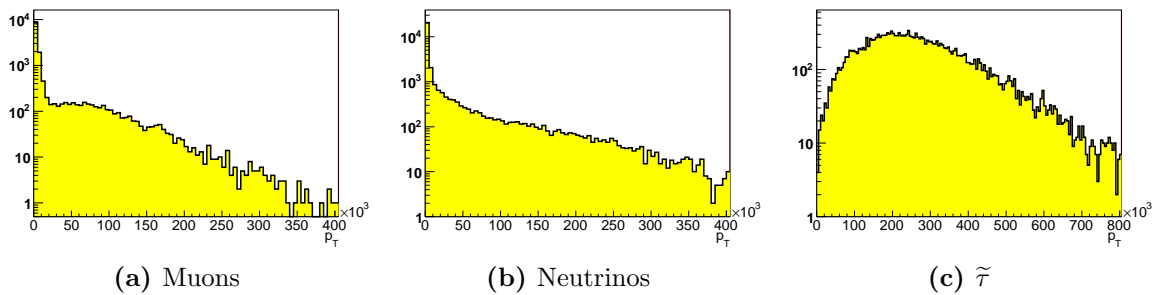
Figure 4.2.: p_T of (a) muons, (b) neutrinos and (c) $\widetilde{\tau}$ in GMSB_100_10 dataset. Scale (a) and (b) extends to 400GeV, (c) extends to 800GeV.

Figure 4.2 shows the transverse momentum of muons, neutrinos and $\widetilde{\tau}$ in events from the GMSB $\Lambda = 100$, $\tan\beta = 10$ dataset. Muons and neutrinos are largely produced with $p_T < 20$GeV but can be produced with transverse momentum of several hundred GeV in some events. $\widetilde{\tau}$ are typically produced with transverse momentum of the order of several hundred GeV. Figure 4.3 demonstrates that the transverse momentum magnitudes of the aforementioned particles are not related to one another.
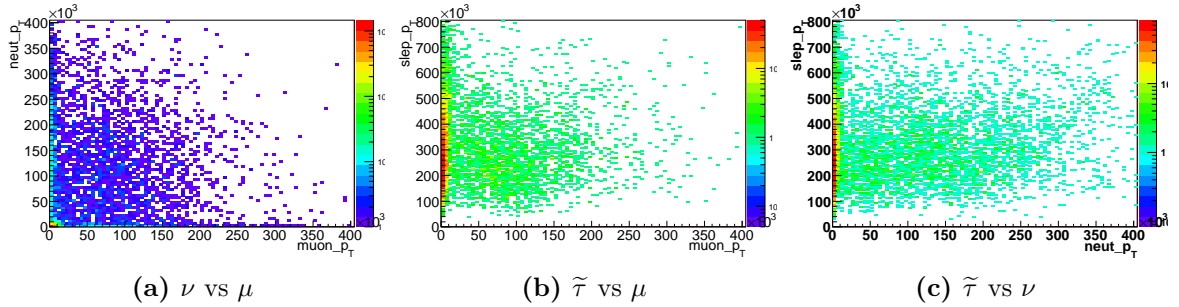
Figure 4.3.: Comparison between p_T of (a) muons and neutrinos, (b) neutrinos and $\widetilde{\tau}$ and (c) muons and $\widetilde{\tau}$ in GMSB_100_10 dataset.

4.2. Muon Monte Carlo simulation

The method employed by this study to identify SMPs is based on measurements of velocity, which rely heavily on time measurements. We do not expect that the accuracy of time measurement accuracy in simulation will be identical to that in data.

Muons can be reliably identified in real data, and are used to test the effectiveness of the velocity measurement algorithm. Muon simulations are used to compare the effectiveness of the algorithm on simulated data with that on real data to check that the method would be able to identify SMPs in real data.

The muon Monte Carlo datasets used in this study are of $Z{\rightarrow}\mu\mu$ and $W{\rightarrow}\mu\nu$ events generated using PYTHIA[27].

4.3. Datastream Selection

Datasets output from ATLAS are split into datastreams composed of events that passed certain triggers or combinations of triggers. It is not possible to analyse all events produced at ATLAS; only those recorded into the datastreams may be used.

Selecting the datastream most likely to contain SMP events requires knowing which triggers are most reliably activated by these events.

4.3.1. Trigger Selection

The efficiency of all available Event Filter (EF) triggers was calculated over a combination of all the simulated GMSB datasets to get a first estimate of which triggers may be useful. The only trigger types to achieve an efficiency of greater than 40% were the plain missing transverse energy (E_T^{miss}) and single muon triggers. The lowest unprescaled

threshold for the single muon trigger is $p_T > 18\text{GeV}$; the lowest for the E_T^{miss} trigger is $E_T^{miss} > 60\text{GeV}$. The two sets of triggers used in this study are thus as follows[1]

- **Single muon trigger**, any of the following:

  – EF_mu18

  – EF_mu18_MG

  – EF_mu18_MG_medium

  – EF_mu18_medium

- $\boldsymbol{E_T^{miss}}$ **trigger**, any of the following:

  – EF_xe60_noMu

  – EF_xe60_tight_noMu

  – EF_xe60_verytight_noMu

(a)　　　　　**(b)**　　　　　**(c)**
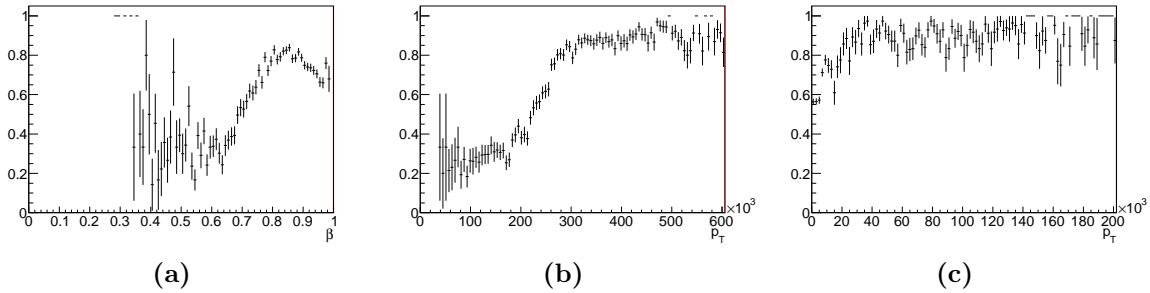
Figure 4.4.: Single muon trigger efficiency against: (a) fastest SMP velocity(β) in event; (b) highest $\widetilde{\tau}$ p_T in event; (c) highest muon p_T in event. (GMSB $\Lambda = 100$, $\tan\beta = 10$)

Figure 4.4a shows the single muon trigger efficiency against the highest slepton velocity in the event, figure 4.4b shows the efficiency against highest slepton p_T. These responses indicate that the single muon trigger is directly detecting the slepton as though it were a muon. Sleptons are almost always produced with enough p_T to activate the trigger. Trigger efficiency for sleptons is mainly dependent upon whether the particle reaches the detector inside the timing acceptance window. The events with lower velocity are triggered by high p_T muons produced in conjunction with the sleptons. Figure 4.4c shows the single muon trigger efficiency against the highest muon p_T in events.

Figure 4.5b shows that the missing E_T which activates the E_T^{miss} trigger is strongly associated with unequal total momentum of sleptons in the transverse plane. If the remaining p_T is carried away by neutrinos it is clear that the missing E_T trigger would be activated. The trigger has also been observed to activate in events with no high p_T

---

[1]The main part of each trigger name is briefly explained in section 3.2.5, the part of the name after the second underbar is unimportant. All variations of the triggers were used to get the loosest possible effective unprescaled trigger.

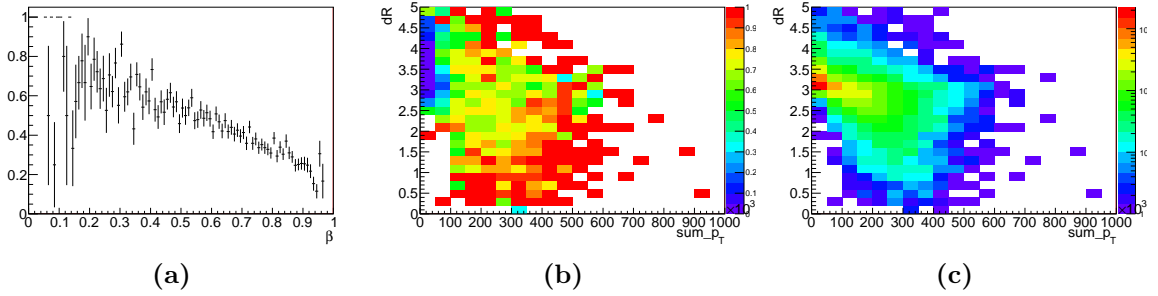**Figure 4.5.:** E_T^{miss} trigger efficiency plotted against: (a)lowest SMP β in event; (b)p_T of sum of slepton momentum vectors and ΔR of slepton momentum vectors. (c)shows the occupancy of bins in (b). (GMSB $\Lambda = 100$, $\tan\beta = 10$)
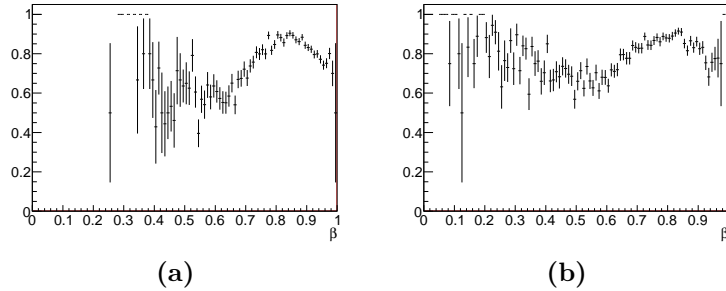
Figure 4.6.: Efficiency of combined single muon and E_T^{miss} triggers plotted against (a)highest SMP β (b)lowest SMP β in event. (dataset is GMSB $\Lambda = 100$, $\tan\beta = 10$)

neutrinos, in the direction of the net slepton momentum. Sleptons carry considerable momentum through the calorimeter, this momentum is measured in the muon spectrometer. The missing E_T trigger, using only calorimeter information, is thus activated if the net slepton momentum is large enough. The trigger efficiency is low when the p_T of the two momentum vectors is equal and opposite; this overwhelmingly happens when $dR \approx \pi$, i.e. when the particles are produced back to back in the xy-plane with the same η heading. Most sleptons are produced this way (fig. 4.5c), so the resulting efficiency of the E_T^{miss} trigger is fairly low.

Generally speaking, the efficiency of the E_T^{miss} trigger increases with decreasing slepton velocity (fig. 4.5a). Combining the single muon and E_T^{miss} triggers gives a good overall response, as shown in figure 4.6.

4.3.2. Datasets selected for analysis

There is no single datastream containing all events from both the single muon and E_T^{miss} triggers. Therefore two datastreams were selected for use in this study. Additionally, $Z \rightarrow \mu\mu$ events from data are required for calibration.

The datastreams used are:

- **physics_Muons** which contains events activating the muon triggers;

  - **SGLMU** focusses on the single muon triggers;

  - **ZMUMU** focusses on events containing $Z \rightarrow \mu\mu$ events;

- **physics_JetTauEtmiss** which contains events activating the E_T^{miss} trigger, amongst others.

Chapter 5.

SMP reconstruction and velocity measurement

Identifying SMPs requires being able to reliably reconstruct the tracks SMPs make through the detector and accurately measure their velocity in order to calculate the particle mass. The properties of charged SMPs are similar enough to muons that the standard muon tracking algorithms in ATLAS should, in most cases, reconstruct them. MuonBetaRefit is a package designed to reconstruct SMP tracks with improved efficiency and measure the velocity of muon-like tracks through further tuning of the muon tracking algorithms used in ATLAS.

Before discussing the reconstruction algorithms and procedures for measuring track velocity, section 5.1 will briefly describe the computing environments used during this process.

Section 5.2 describes the track identification algorithms, MOORE and MUID, used by MuonBetaRefit to reconstruct SMP tracks and section 5.3 describes the operation of MuonBetaRefit in detail. Section 5.4 then explains how velocity measurements can be drawn from the results of MuonBetaRefit.

Calibration of the detectors used by MuonBetaRefit beyond the level of standard ATLAS operation was also necessary. Section 5.5 examines why this is so and how it was performed. Lastly, section 5.6 demonstrates the performance of MuonBetaRefit in measuring track velocity and distinguishing SMPs from muons.

5.1. The ATHENA environment and analysis chain

The processes that measure track velocity and identify SMPs take place in two distinct computing environments; ATHENA and `ROOT`. ATHENA is the framework of algorithms used for reconstructing events at the ATLAS experiment, while `ROOT` is a more general computing framework geared towards physics analysis. Reconstructing raw data from the detector into muon tracks and refitting them requires numerous service algorithms and detailed detector information. Such reconstruction therefore must be done in the
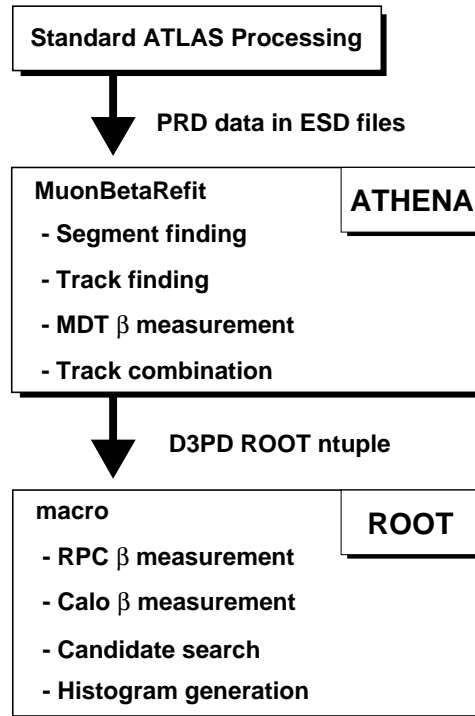
Figure 5.1.: Analysis chain used in study

ATHENA environment. Measuring velocity from simpler quantities such as hit position and time does not require such supporting information and can be done in a `ROOT` macro. This section describes the two environments and examines how their differences affect the ways in which velocity measurements are made.

5.1.1. ATHENA

ATHENA[22] is the software framework used by the ATLAS project to process data being produced by the detector. It is based on the blackboard[24] architectural model, a modular framework populated by algorithm classes to process data and distinct data classes containing the information being passed between algorithms. Blackboard systems such as ATHENA consist of several elements.

- The blackboard: a repository of information available to all processes.

- The algorithmic modules: procedures for processing data read from the blackboard and saving the results either to the blackboard or to file.

    - Athena also uses highly modular sets of tool classes, which are used by algorithms to perform a particular task. Data can be passed directly between these classes and the algorithm using them without utilizing the blackboard.

- The controller: an overseeing algorithm which specifies which algorithms are run, in what order, using what data.

To be able to reconstruct and fit tracks, detailed information about the detector geometry, magnetic fields and materials is required. ATHENA can create an environment with algorithms that produce this information. MOORE, MUID and MuonBetaRefit are all collections of algorithms and tools which run inside the reconstruction environment of the ATHENA framework. The final output of reconstruction and analysis in ATHENA is a database file written to disk, known as an ntuple.

5.1.2. `ROOT`

`ROOT` [23] is an object-oriented data analysis framework built to meet the needs of physicists performing data analysis, particularly in high energy physics. It provides an extensive library of classes and tools for data analysis such as function fitting, data storage and histogram plotting. These classes are all built around a strict inheritance hierarchy that allows for easy manipulation of large amounts of data at once.

The CINT interpreter can be used to directly input c++ commands to a command line interface, but for larger scale processing predefined macros are preferred. `ROOT` macros are c++ based scripts readable by `ROOT` which can tell it to perform certain actions. For this study an extensive set of histogram building and function fitting libraries were written using the `ROOT` framework in c++ and compiled. A `ROOT` macro was designed to use these functions to analyse the ntuples output from ATHENA.

The `ROOT` environment, unlike the ATHENA environment, has no intrinsic link to the ATLAS detector; there are no tools providing geometry information. Any processes that requires information about the detector not available in ntuples, such as track reconstruction, cannot be performed in the `ROOT` macro.

5.1.3. The analysis chain

ATHENA is responsible for finding and fitting tracks, but the final analysis of particle velocity takes place in a `ROOT` macro. Figure 5.1 shows the chain through which data from the detector is produced and analysed. Event Summary Data (ESD) files contain raw data from individual events and are produced by standard processing at ATLAS. D3PDs are simply a format of ntuple used to save data produced by ATHENA. All other terms in figure 5.1 are elaborated on through the course of this chapter.

Velocity measurements made using the MDT are based on refitting tracks using a range of β hypothesis to find the β that gives drift circles best fitting the track. By contrast, velocity measurements made using the RPC and calorimeter are based on a simple calculation of measured distance and time from the interaction point. The methodology is discussed in detail in sections 5.3 and 5.4. For now it is important to

note that while velocity measurements can be made by the RPC and calorimeter in `ROOT`, MDT based velocity measurements are intrinsically tied to MuonBetaRefit and can only be done inside ATHENA.

For both methods, accurate time measurements are necessary to make accurate velocity measurements. To ensure that this accuracy is optimized and that it is kept consistent throughout the 2011 data a system of calibration is utilized. This calibration is described in detail in section 5.5. Essentially it consists of shifting the measured times so that they have a peak at $t_0 = 0$ when measuring the time of flight of $\beta = 1$ muons.

The amount of processing that takes place inside ATHENA in order to reconstruct and refit tracks means that a `ROOT` macro can process the same number of events in a fraction of the time. It is therefore vastly preferable to make as many measurements in the `ROOT` macro as possible to avoid unnecessary and time consuming processing within ATHENA. This has implications for the calibration of the MDT. RPC and calorimeter calibration databases can be produced from an ntuple and then used to calibrate velocity measurements made using the same ntuple, taking a matter of hours for all data produced in 2011. MDT calibration databases are produced in the same way. However, to make velocity measurements, ATHENA must reconstruct tracks for each event from PRD (see section 5.2.1). For data corresponding to the whole of 2011 this can take weeks. Calibrating the MDT thus represents a major undertaking and is the main bottleneck in the calibration process.

5.2. Muon reconstruction in ATLAS

Algorithms reconstructing a particle trajectory from raw hit information are necessary when conducting a particle search. In this study, two of the muon algorithm packages in ATLAS, Muon Object Oriented Reconstruction (MOORE) and Muon Identification (MUID), are used and are discussed in this section. The two algorithms are complimentary. MOORE (section 5.2.2) finds tracks from hit information in the muon spectrometer. MUID (section 5.2.6) takes the tracks produced by MOORE and link them to tracks in the inner detector and calorimeter hits likely to be associated with the same particles. The different data classes ATHENA uses to pass information between MOORE, MUID and MuonBetaRefit are also discussed (section 5.2.1).

The tracks left by SMPs being searched for already share many features with muons, so MOORE only requires slight modification to be effective. This modification is described in section 5.3. MUID requires no modification and is only used to obtain calorimeter information and increase the reconstruction reliability by verifying a likely association with tracks in the inner detector.

More information on MOORE and the Muon Event Data Model can be found in references [19] and [20]. More information on MUID can be found in reference [21].

5.2.1. Data types

The ATHENA framework algorithms mainly pass data between themselves via the blackboard in specific classes for each type of information. Most reconstruction algorithms, such as MOORE, process these data classes from basic signals generated by detector elements into something more representative of particle behaviour.

The data class design for muons is called the Muon Event Data Model and can be briefly explained as providing the following data classes.

- **Hits** represent an individual detector element response, ranging from raw signal information to a calibrated estimate of a particle trajectory's intersection with the detector.

    - **Raw Data Object (RDO)** – A description of all the raw signal information obtained from detector elements.

    - **PrepRawData (PRD)** – An initial estimate of the particle trajectory's intersection with the detector, produced by detector specific algorithms from RDO.

    - **Reconstructed Input Object on Track (RIO on Track, or ROT)** – A copy of the PRD information copied for inclusion in segments and tracks. This information is often modified by the pattern finding algorithms. The original PRD should not be modified as this may bias later operations by different algorithms on the same hits.

- **Segments** – ROT patterns identified over a short distance, usually one station.

- **Tracks** – ROT patterns which can extend over the whole of ATLAS. Of interest are:

    - **Muon Spectrometer (MS) tracks** – Tracks which have been reconstructed only in the muon spectrometer.

    - **Standalone (SA) tracks** – MS tracks which have been extrapolated to the interaction point.

    - **Inner Detector (ID) tracks** – Tracks which have been reconstructed only in the inner detector.

    - **Combined (CB) tracks** – The result of combining SA, ID, potentially other tracks and other data to obtain the fullest possible description of a particle trajectory.

- **Collections** – Containers for storing multiple objects of the same type.

The ATHENA blackboard generally only stores these classes as collections, not individually. The pattern finding algorithms give tracks and segments estimates of the momentum

and overall trajectory of the particle as well as the original position information stored in the hits they contain.

An additional "Muon" class is also provided. This is a full representation of a muon particle and contains all information relating to its path through the detector. It may contain a number of different kinds of track as well as energy deposition information and overall estimates of particle properties such as momentum, velocity and mass.

5.2.2. Muon Object Oriented Reconstruction (MOORE)

MOORE is a package of algorithms which together build standalone tracks in the muon spectrometer from PRD hit information. The package is designed to be highly modular, with different algorithms providing separate services linked by the ATHENA controller.

Reconstruction takes place in the following distinct steps.

- **Pattern finding** searches for patterns of hits indicative of a common originating particle.

- **Segment making** builds segments from these patterns.

- **Track building** tries to collate the available segments into a full track.

The following sections describe how MOORE accomplishes each of these steps, the end result being a collection of MS-tracks. Following afterwards, MUID, which extrapolates these tracks into SA-tracks and attempts to build CB-tracks from them, will be described.

5.2.3. Pattern finding

The first step is to find patterns of hits likely to have been caused by a single particle and discard unrelated "noise" hits. This search is performed over the whole detector but requirements for identifying a pattern are comparatively loose and the patterns must be refined by later steps. MOORE finds patterns of hits using Hough transforms.

Hough Transforms

Hough transforms are techniques for identifying patterns in data, commonly used in image analysis. A Hough transform

$$P(\overrightarrow{x}) \rightarrow H(\overrightarrow{x}, \overrightarrow{\alpha}), \tag{5.1}$$

converts a point in some dimensional space ($\overrightarrow{x}$) to a curve in Hough space ($P(\overrightarrow{x})$, where $\overrightarrow{\alpha}$ are free parameters added by the transform. There are a special class of transforms which generate curves that cluster together at a point in the Hough space if the points
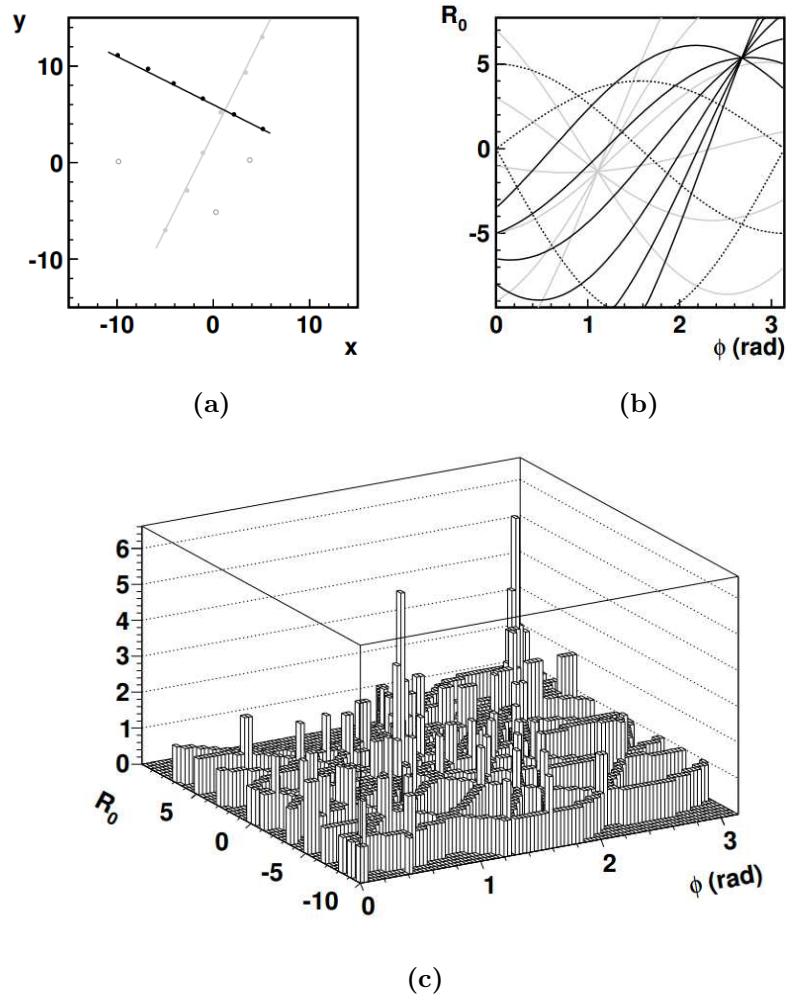
Figure 5.2.: Hough transform steps. (a) Data points in x and y. (b) Curves representing the points in Hough space, curves converge at the point which parametrises the line through the points. (c) curves plotted in a histogram, convergence is at the maximum bin.

from which they were generated share a symmetry particular to that transform. The point in Hough space at which the curves cluster provides the parameters of this symmetry.

One of the simplest examples of the Hough transform technique is a search for straight line symmetry amongst discrete points in a 2 dimensional space. We shall refer to the original 2 dimensional space as "normal space" and the space of the transform and free parameters as the "Hough space". The transform used in this case is

$$\phi(x, y, x_0) = \arctan\left(\frac{y}{x - x_0}\right), \tag{5.2}$$

where x and y are the point coordinates. The Hough space in this case is a 2 dimensional space of an angle (ϕ) relative to the y-axis in normal space and a position along the x-axis (x_0) in normal space. The curve this function generates represents ϕ for a straight line passing through the xy-point and intersecting the x-axis at x_0. Curves from points with a straight line symmetry should converge on the area in Hough space which correctly parametrises the straight line of their symmetry. Figure 5.2 shows how points in normal space can be converted by this Hough transform and how the curves describing them converge on the correct parameters. The convergence can be most easily found by making binned histograms of the curve and looking for bins with high occupancy.

The magnetic field in ATLAS' muon spectrometer is designed to bend muon trajectories in the RZ plane but have minimal impact on the XY plane. It is convenient then to analyse these two planes separately when looking for patterns. Initial patterns of hits are found in each plane separately first. Correlation between patterns in the two planes is searched for in order to merge the two sets of patterns into a single set of three dimensional patterns. These three dimensional patterns constitute the output of the pattern finding process and are passed into the Segment maker.

XY plane

In the muon spectrometer the magnetic field through the XY plane can initially be ignored, track trajectories are considered to approximate to a straight line. Any offset introduced by curvature from the inner detector solenoid is accounted for by the impact parameter. The Hough transform creates curves in a Hough space of azimuthal angle ϕ and impact parameter r_0 through:

$$\phi(x_{hit}, y_{hit}, r_0) = \tan^{-1}\left(\frac{x_{hit}}{y_{hit}}\right) + \tan^{-1}\left(\frac{\sqrt{r_{hit}^2 - r_0{}^2}}{z_{hit}}\right), \tag{5.3}$$

ϕ is the angle with respect to the x-axis and r_0 is the closest distance a line comes to the origin, i.e. the beam crossing point. x and y are the hit position coordinates and $r_{hit} = \sqrt{x_{hit}^2 + y_{hit}^2}$.

For each ϕ measuring hit in an event, a scan over viable r_0 gives Hough space coordinates which can be filled into a histogram. If a maximum can be found in this histogram, hits are compared with the trajectory it describes by measuring the minimum distance between hits and the trajectory in normal space. If the distance is less than 250mm then the hits are associated with that trajectory. If a trajectory has more than one hit associated with it, then it is registered as a ϕ-pattern and its associated curves are removed from the Hough space and the next maximum is searched for. This is repeated until no hits are left or until no maxima are found.
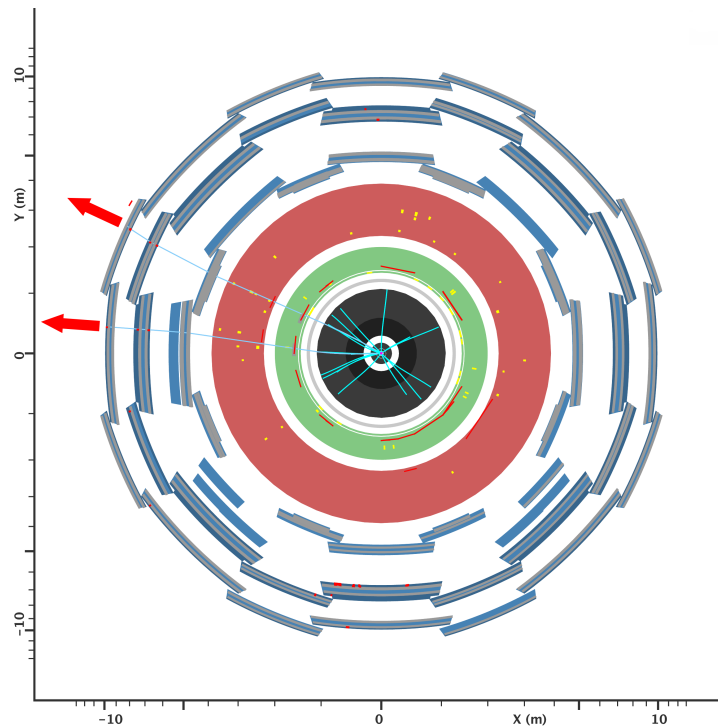
Figure 5.3.: Hit patterns of two muon tracks in the XY plane. Bending in the muon spectrometer (blue) is only significant in the RZ plane, so tracks can be approximated to straight lines

RZ plane

The magnetic field in the RZ plane is not negligible, meaning that a more complex model must be used than that for the XY plane. Bending occurs significantly in areas with strong magnetic fields as shown in figure 5.4, but not in other areas.

The magnetic field in the inner detector region, before the first reference surface, causes negligible bending in the RZ plane so trajectories are assumed to be linear. In the barrel, the trajectory past this point is modelled by a parabola constrained by the requirement that its position and derivative at the reference surface must match the linear trajectory. In the endcap the trajectory is more complicated because of the lack of bending field between the mid-station and outer-station. Until the trajectory meets the second reference surface the procedure is the same as for the barrel. After this point it is described by a linear trajectory with the parabola constrained to match it at the second reference surface similarly to the first. Both trajectory descriptions have only 3 parameters: the starting point of the track; the direction of its first linear section and the curvature of the parabola section. To further simplify the transform, the track is assumed to start exactly at the origin, without the introduction of an impact parameter,
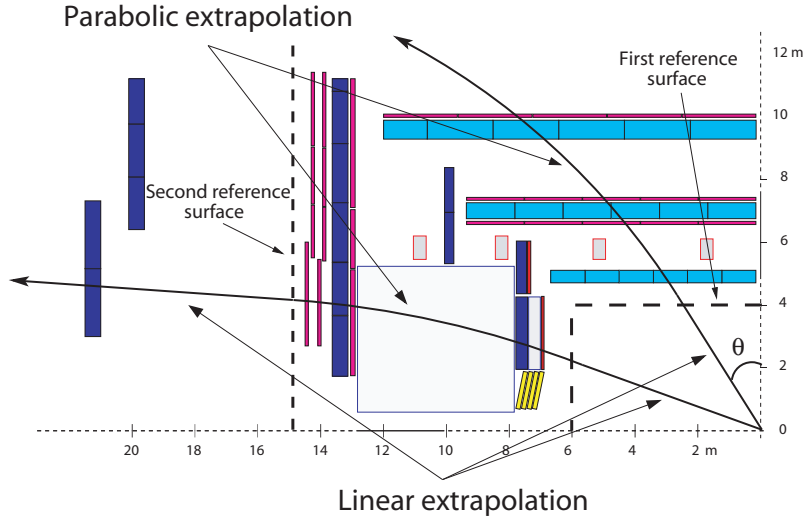
Figure 5.4.: Potential trajectories in the RZ plane. Bending is significant in the areas with
strong magnetic fields, in these areas parabolic extrapolation is used, in other
areas linear extrapolation is used.

giving a transform into θC Hough space

$$\theta = \theta(r, z, C), \tag{5.4}$$

where θ is the angle between the initial trajectory and the r-axis, r and z give the hit
position and C is the curvature of the parabola section.

For each η measuring hit, C is scanned and a Hough space histogram is generated.
Similar to the XY plane, a maximum is searched for and hits are associated if they are
closer than $scale \times 500$mm where $scale$ is a scaling factor introduced to compensate
for error propagation outwards in trajectory parameters caused by linking the pattern
sections together. Although constrained to $1 \leq scale \leq 3$, when between these values
scale is

$$scale = \frac{\sqrt{x_{hit}^2 + y_{hit}^2 + z_{hit}^2}}{5000(\text{mm})} \tag{5.5}$$

If more than one hit is associated with the trajectory described by the maximum in
Hough space, the trajectory is registered as a η-pattern and associated curves are removed
from the Hough space. Similar to the XY case this process is repeated until no hits are
left or until no maximum is found.

Pattern merging

The ϕ and η patterns must be merged into a three dimensional pattern before continuing.
Each possible pairing of ϕ and η patterns is examined. For each pair, first the hits from

the η-pattern are compared with the ϕ-pattern using a similar distance requirement to that described above in associating hits to trajectories in the RZ plane. If more than one η measuring hit is assigned to the ϕ-pattern, the hits from the ϕ-pattern are similarly compared with the η-pattern and matching hits associated with it. If a sufficient number of hits are combined between the two patterns, they are merged into a three dimensional pattern. If an η-pattern with no matching ϕ-pattern is found, it is converted to a three dimensional pattern using the ϕ information available in the hits of the η pattern.

5.2.4. Segment making

The next step is to take hits from the three dimensional patterns and attempt to make more refined patterns locally in each station. For each pattern, segments are searched for in each chamber individually, using only the hits from the current pattern in that chamber and the neighbouring chambers in the same station. Hits from neighbouring chambers that belong to different stations are not included; these hits form separate segments that are later merged in the track finding stage.
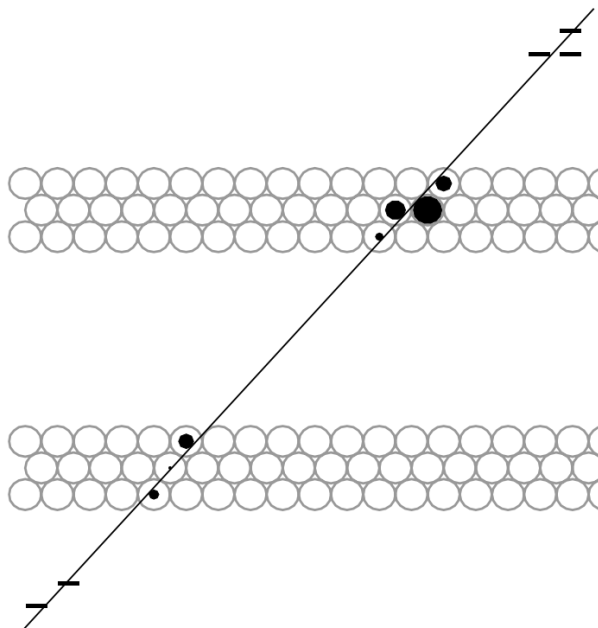

Figure 5.5.: Fitted segment in yz-plane of MDT chamber's local coordinate system. MDT drift circles and trigger hits from adjacent trigger layers are shown

The segment making procedure takes place in the yz-plane (see figure 3.18a) of the coordinate system local to the chamber (fig. 5.5) and consists of:

1. Seed line generation

2. MDT hit association to seed lines

3. Fitting seed lines and converting to segments

4. Segment refining

5. Trigger hit association to segments

Each of these steps is described in the following sections. After the process is complete, the final segments are passed into the track builder.

Seed line generation

For every possible pair of MDT hits, all possible tangents of their drift circles are taken as seed lines for a segment (fig. 5.6). The resulting large number of seed lines is quickly reduced as quality cuts are applied in later steps.

(a)　　　　　　　　　　　(b)
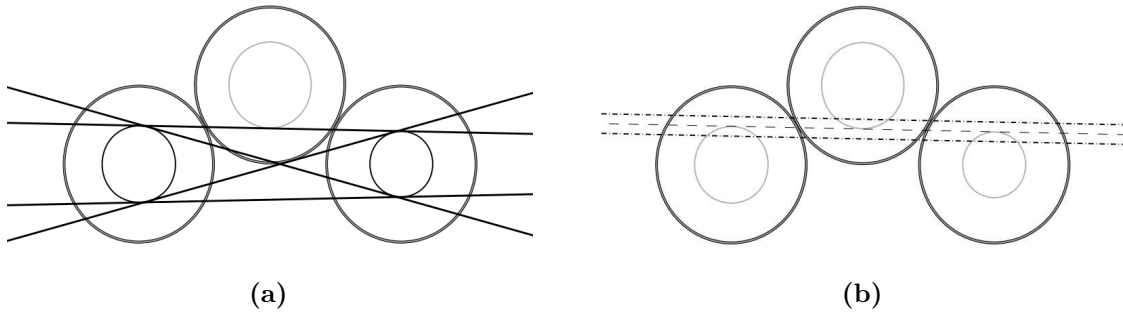
Figure 5.6.: Seed lines for the segment search. (a) All tangents used as potential seed lines for one pair of drift circles. (b) the seed line with a 1.5mm margin for hit association.

MDT hit association to seed lines

For each seed line, MDT hits are associated by comparing their position with the line. For each hit, $\Delta r = r_{rt} - r_{line}$ is calculated, where r_{rt} is the hit drift radius and r_{line} is the radius of closest approach of the current line to the hit's wire. Hits are classified according to

- $|\Delta r| < 1.5$mm: associated with the line and hit is called 'hit-on-track', number of hits counted by N_{trk}

- $\Delta r < -1.5$mm: potentially caused by a δ-electron from the muon and hit is called 'delta', number of hits counted by N_{delta}

- $\Delta r > 1.5$mm: unphysical situation and hit is called 'out-of-time', number of hits counted by N_{out}

The number of tubes the line crossed, which did not generate a hit, is also counted by N_{empty}. Lines are pre-selected by discarding those not satisfying

$$\frac{N_{delta} + N_{out} + N_{empty}}{N_{trk}} < 1.1 \qquad (5.6)$$

(a) hit-on-track   **(b)** δ-electron   **(c)** out-of-time   **(d)** empty tube
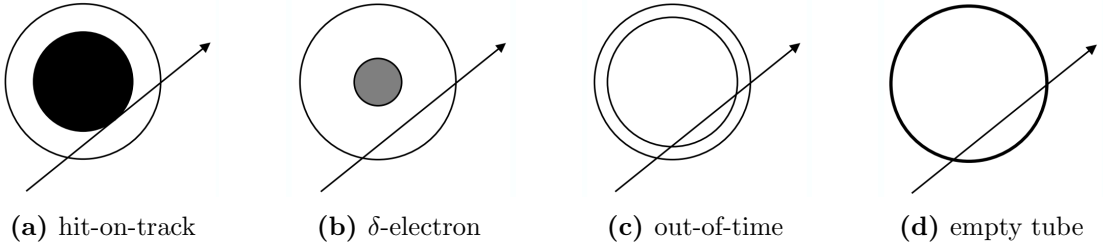
Figure 5.7.: Classifications of MDT hit possible when associating hits to seed lines (a) hit-on-track, (b) delta hit, (c) out-of-time, (d) empty tube

Fitting seed lines and converting to segments

Any lines with $N_{trk} > 3$ are fitted by minimizing

$$\chi^2 = \sum_{i=1}^{N_{trk}} \frac{(r_{line,i} - r_{rt,i})^2}{\sigma_{rt,i}^2} \qquad (5.7)$$

where σ_{rt} is the error on r_{rt} and i indexes each 'hit-on-track'. The lines are then promoted to segments, with their 'hits-on-track', 'delta' and 'out-of-time' hits associated with them.

To reduce the number of segments likely to describe the same particle, segments which are subsets of other segments are identified and removed. Segments are subsets if their line parameters are similar ($|\Delta\theta| < 0.05$, $|\Delta d| < 0.5$mm) and they have lower N_{trk} or, if N_{trk} is the same, higher χ^2.

Segment refining

Fitting the segments changes the line parameters and potentially invalidates hits previously classified as 'hits-on-track' as well as validating hits previously classified as 'delta' or 'out-of-time'. The classification is performed again, this time taking σ_{rt} into account.

- $|\Delta r| < 5\sigma_{rt}$: 'hit-on-track'

- $\Delta r < -5\sigma_{rt}$: 'delta'

- $\Delta r > 5\sigma_{rt}$: 'out-of-time'

N_{empty} is also re-calculated.

Segments with an unusually large χ^2/n_{dof} (> 10) are further refined by attempting to identify and remove individual hits likely to be causing an excess of χ^2 and then re-fitting the segment. After this refit, hits are re-classified as above. The procedure is repeated until the segment has $\chi^2/n_{dof} < 10$, when the segment is accepted, or until $N_{trk} < 3$ at which point the segment is discarded.

Trigger hit association to segments

To associate trigger detector hits with the segment generated from MDT hits the pull (p) is used.

$$p = \frac{d}{\sqrt{\sigma_{clus}^2 + \sigma_{seg}^2}} \qquad (5.8)$$

where d is the distance between the hit and the segment line in the local yz-plane, σ_{clus} is the error on the trigger hit cluster position and σ_{seg} is the error on the segment fit. The pull is essentially a separation measurement divided by an estimate of the error on that separation. Trigger hit clusters from layers overlapping the MDT chamber of the segment are associated if their pull relative to the line is sufficiently low.

- RPC hit clusters are associated if $|p| < 7$

- TGC hit clusters are associated if $|p| < 20$

5.2.5. Track building

The segments produced are each naturally associated with one of the three dimensional patterns from which their hits are obtained. The combination of segments associated with one of these patterns extends through the whole detector, but is too crude an estimate to be used as a track for physics analysis. MOORE must build the segment combinations into more reliable tracks with more rigorously measured parameters.

The main track fitting process takes into account all detector material and is relatively cpu-intensive. To reduce cpu-load, first, track candidates are produced by re-evaluating the segment combinations without using the main track fitter. Then tracks are fitted solely from the segments in the track candidates through the following process (visualized in figure 5.8).

1. **Resolving station overlaps**: Overlapping segments from neighbouring stations are merged.

2. **Seed selection**: A reliable segment is chosen to act as a seed for the track.
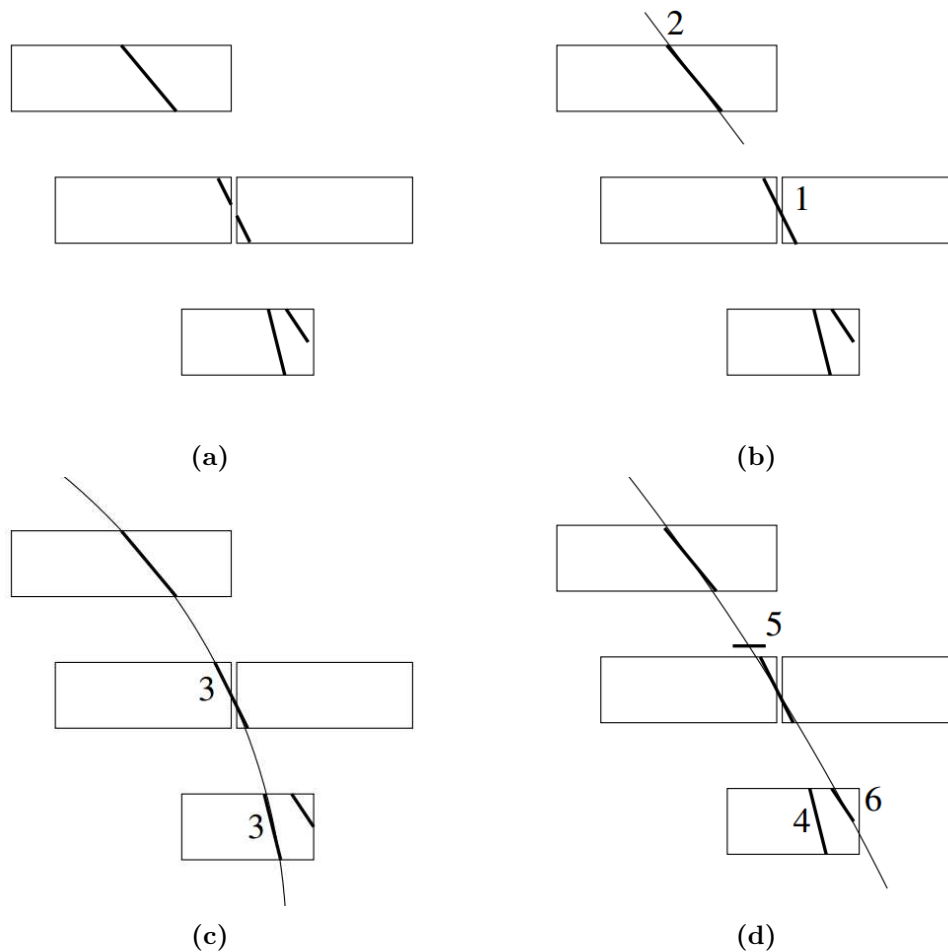
Figure 5.8.: Simple example of the steps in track fitting, numbers correspond to the steps listed. (a) Segments prior to track fitting. (b) Segment overlaps resolved and outermost segment selected as seed. (c) Segments added to see. (d) Track cleaning, hit recovery and segment recovery.

3. **Adding segments**: Segments are added based on the results of a fit to form a track.

4. **Track cleaning**: After building a track, outlying hits and segments are removed.

5. **Hit recovery**: Possible missed hits are added to the track.

6. **Segment recovery**: Possible missed segments are added to the track.

7. **Ambiguity solving**: The ambiguity of hits potentially belonging to multiple tracks is resolved.

After these steps the tracks are placed in a collection and output from MOORE. The following subsections describe the track candidate finding step and each of the further steps listed above in greater detail.

Track candidate finding

Segment combinations associated with three dimensional patterns are re-evaluated, removing segments which do not match others in the combination. This reduces the number of segments being passed into the relatively cpu-intensive full track fitter.

First, segments with $N_{empty}/N_{trk} > 1.2$ are removed and segments with no trigger hits associated are further constrained by removing any with $N_{empty}/N_{trk} > 0.8$. The remaining segments are ranked by:

1. **smaller number of segments in station**: isolated segments are preferable as seeds;

2. **smaller N_{empty} and number of missing trigger hits**: fewer missing hits indicate a better segment;

3. **higher momentum**: high momentum is indicative of a reliable segment originating from a muon. Momentum of a segment can be estimated from its angle relative to the interaction point.

The segments are selected as seeds, starting with the highest ranking, and other segments in the same combination are tested for compatibility with it. If the segments are compatible and neither belong to a track candidate then a new track candidate is generated. If they are compatible and one already belongs to a track candidate then the other segment is saved to that track candidate. If they are compatible and both belong to different track candidates then both are included in both track candidates, but the candidates remain separate.

Compatibility is tested by comparing the pull of a χ^2 fit of the two segments. The pull of a variable in this case is defined as

$$p = \frac{x_{meas} - x_{fit}}{\sqrt{\sigma_{meas}^2 + \sigma_{fit}^2}} \tag{5.9}$$

where x_{meas} is a measured parameter and x_{fit} is the fitted value, σ_{meas} and σ_{fit} are the errors on these values. The parameter x describes depends on the fitting model. The two segments are compatible if they they originated from the same pattern and the absolute pull of the two segments' position and direction parameters is $|p| < 5$.

For segments overlapping two neighbouring stations a straight line fit is used. For separate stations, the same model used in the pattern finding described in section 5.2.3 is used by the χ^2 fitter. If the segments are deemed incompatible through this fit, a straight line fit is also attempted.

The track candidate finding process can create many duplicate and near-duplicate tracks. The collection of candidates is cleaned by merging any pair of candidates with more than half of their contained segments being the same.

Resolving station overlaps

Up to this point, segments in neighbouring chambers but different stations have been considered separate. These segments are merged into a single segment ahead of the full track fit, provided they satisfy a straight line χ^2 fit.

Seed selection

The track building process requires a reliable segment to act as a seed. The track initially contains only the seed segment; the addition of further segments is described in the next section.

Segments from the outer stations generally suffer from less noise. The highest quality segment in the outermost station is therefore selected as a seed for the first track fit. The seed for the next track is selected using the same criteria from segments not already tried as seeds and not already included in a track. This can result in several tracks being created from a single track candidate.

Adding segments

Segments are tested for combination with the track using a track fitting algorithm. If the resulting absolute pull is less than 5, the segment is added. Segments are tested in order of the station they are located in and if successfully added, will be included in the track for the next fit. The station order used is: outer, middle, inner, extended.

The track fitter used for this study is the GlobalChi2TrackFitter. Other algorithms are also available. This fitter takes into account the material composition of ATLAS as well as other details of the detector geometry and is cpu-intensive.

Track cleaning

After tracks have been refitted, outlying hits and misreconstructed measurements are identified and removed. Whole stations may be removed from the track if their average pull is greater than 3.5 and removal of the hit with highest pull does not sufficiently lower the average. Tracks must keep a minimum of two stations after this process; otherwise they are discarded. MDT drift circles are checked to fix any positions generated on the opposite side of the circle to the track.

Hit recovery

Hits can occasionally be present, but missed by the pattern finding or segment making algorithms and not included in the track. A search for hits in strips and tubes crossed by

the track is conducted in all chambers with a hit included in the track. If a hit is found, it is classified by its absolute pull relative to the track. If $|p| < 3$ (MDT), $|p| < 5$ (not MDT), the hit is added to the track and a refit performed, otherwise it is added as an outlier. If a hit is not found, that detector element is classified as a "hole" in the track.

Segment recovery

Segments which were reconstructed correctly but belonged to a different combination may not have been added to the correct track. Any track with a missing segment in the outer, middle or inner station has a new segment search conducted in that station using the current track parameters. If a matching segment is found, it is included in the track and the track refitted.

All tracks must have hits from more than one station. Any track with more than 5 holes must have hits from more than two stations, otherwise it is discarded.

Ambiguity solving

After track reconstruction it is possible that a segment may belong to more than one track. This ambiguity is resolved by choosing the track with the best fit quality and assigning the ambiguous hits to it alone. Other tracks have these hits removed and their fits redone and their values recalculated, discarding any that fail the previously established requirements. Finally, tracks are compared in pairs for potential merging.

5.2.6. Muon Identification (MUID)

MOORE provides tracks constructed from hits in the muon spectrometer. To use information from the inner detector and calorimeter it is necessary to first associate that information with the MS-tracks. Checking that an ID-track exists to which the MS-track can be combined gives a further check that the track actually originates from a particle and is not a "fake" track.

It does this in two main stages:

- **MUID Standalone** extrapolates the MS-track through the magnetic field to near the interaction point. The extrapolation takes into account energy loss and multiple scattering by considering the muon spectrometer and calorimeter as a set of scattering planes. The energy loss can be estimated by parametrisation using the muon momentum and the depth of material passed through. Additionally, measurements from calorimeter cells containing the crossing point of the track with the plane are searched for and if greater than the parametrised estimate are used instead. This allows for greater accuracy in the reconstruction of isolated muons.

  The process outputs SA-tracks, which can be directly compared with ID-tracks.
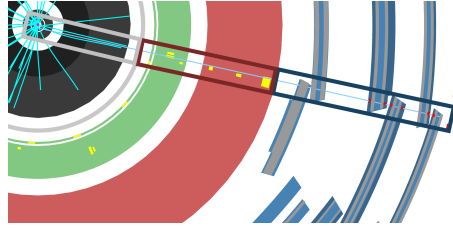
(a)
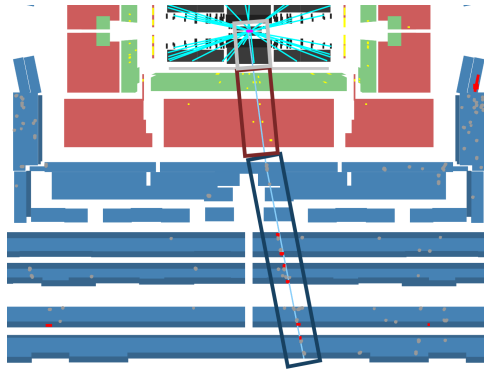
(b)

Figure 5.9.: Example of a muon spectrometer track (blue), that has been extrapolated (red) and matched to an inner track (grey). The same track is shown in the (a) xy-plane, (b) rz-plane.

- **MUID Combined** then searches for ID-tracks and calorimeter hits matching the SA-track. ID-tracks are matched to the SA-track using a χ^2 fitter, outputting a CB-track.

If MUID is successful we are left with one of each of the four track types outlined in section 5.2.1 (MS,SA,CB,ID) associated with a Muon class. Calorimeter measurements found during the backtracking procedure are also added. Failure to extrapolate MS-tracks into SA-tracks is rare for high p_T tracks. However, the combination process with ID-tracks is more prone to failure, either because an ID-track was not reconstructed or because it was not correctly associated with the SA-track. In this case only the MS and SA tracks are available.

5.3. MuonBetaRefit

MuonBetaRefit is an algorithm which measures the velocity of muon-like tracks using the MDT detectors. It modifies MOORE to search for tracks of slow moving particles and matches them with data from other parts of the detector using MUID. Although the

main velocity measurement made by MuonBetaRefit uses the MDTs, the hit information from the RPCs included in the fit can also be used to measure velocity. The calorimeter information added to the track by MUID can also be used. Velocity measurements from all these detector technologies is examined in more detail in section 5.4.

MOORE is modified by changing the time of flight assumption used when reconstructing MDT drift circles rather than using the standard $\beta = 1$ assumption for muons.

The operation of MuonBetaRefit can be split into three phases.

1. Seed tracks are found using muon spectrometer hit data

2. Seed tracks are refitted to find the velocity which produces hits that best fit the track

3. Refitted tracks are combined with data from inner detector and calorimeter

The first two phases uses MOORE algorithms while the third uses MUID.

5.3.1. Time of flight calculation

When reconstructing MDT drift circles it is necessary to know the time difference between when the signal was detected and when the particle arrived. For muons this is straightforward as the velocity difference between muons reaching the muon spectrometer and the speed of light is smaller than can be detected with the time resolution of the detector. As such, standard MOORE reconstruction makes the assumption that the time of flight is simply $t_{tof} = \frac{d_{detector}}{c}$, where $d_{detector}$ is the distance of the detector element from the interaction point.
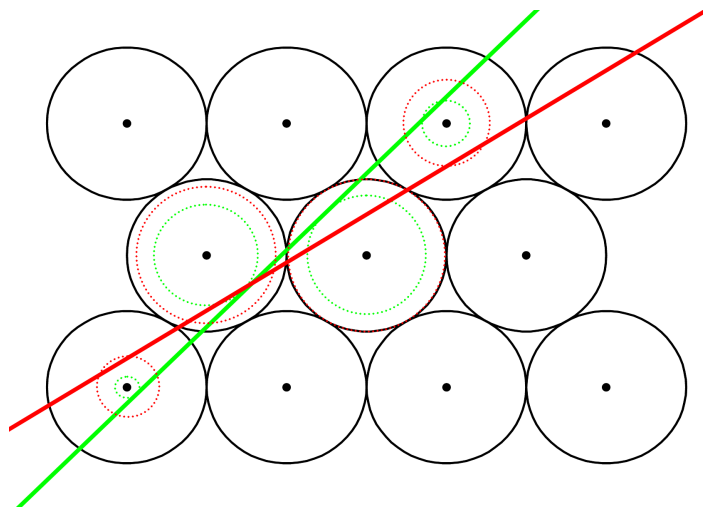

Figure 5.10.: Representation of MDT drift circles for a low β track. Correct track and drift circles with low assumed β shown in green, standard MOORE $\beta = 1$ assumption shown in red

The $\beta = 1$ assumption must be changed when reconstructing the drift circles of slower moving particles. This is done using the ToF tool. The ToF tool changes the time of flight assumption to $t_{tof} = \frac{d_{detector}}{\beta c} - k$ where k is the sum of any calibration constants used (section 5.5).

Drift circle radius is linked to the ToF by $r_{drift} = \frac{t_{hit} - t_{propagation} - t_{tof}}{v_{drift}}$ where t_{hit} is the hit time recorded, $t_{propagation}$ is the time taken for the signal to propagate along the MDT pickup wire and v_{drift} is the drift velocity of electrons inside the MDT tube. $t_{propagation}$ is calculated by MOORE from the position along the MDT wire at which the signal was detected. It is not changed by altering the β assumption and for the purposes of this study can be ignored, effectively merging it with t_{hit}.

Muon spectrometer detectors other than the MDT are not affected by changes in particle velocity unless the particle is slow enough to miss the signal timing acceptance window for that event. This corresponds to a velocity of approximately $\beta < 0.3$ for the RPC and $\beta < 0.5$ for the TGC.

5.3.2. Time-of-flight tool integration into MOORE

The ToF tool is integrated into the MOORE algorithms by adding it to clones of those algorithms at run time. A clone of drift circle reconstruction tool is made, directly implementing the ToF tool in its calculations. Clones are then made of every MOORE algorithm using the drift circle tool, with the tool replaced with the modified version. This cloning process is propagated through the whole tree of MOORE algorithms until modified versions of all necessary algorithms are obtained. The modifed MOORE algorithms used by MuonBetaRefit are:

- MooSegmentCombinationFinder, which converts PRD collections into collections of segment combinations as described in section 5.2.4.

- MooTrackSteering which to generates tracks from these segment combinations as described in section 5.2.5 as well as provide an interface to the track fitting algorithms.

This has the effect of changing the drift circles used by MOORE in the segment finding process described in section 5.2.4 and onwards without altering the functionality of MOORE in any other way.

5.3.3. Seed track generation

To find SMPs, we need to be able to identify tracks which, while muon-like, might not be successfully reconstructed by the standard MOORE algorithm because of their low velocity. MuonBetaRefit uses versions of the MOORE algorithms, wrapped in two

controlling algorithms, to generate seed tracks. The wrapper algorithms operate at the segment combination finding and track making levels.

The segment combination finding algorithm is called to find segments in the muon spectrometer, using a given β assumption. It reads muon spectrometer PRD hit data from events, sets the ToF tool β value and passes the PRD into the modified version of MooSegmentCombinationFinder. The segment collections generated are then returned.

The track making algorithm is called to find tracks in the muon spectrometer from these segment collections, using a given β assumption. It gets segment collections from the segment combination finding algorithm, using the β value supplied, sets the β value of the ToF tool again and passes the segments into the modified version of MooTrackSteering. The track collections generated are then returned.

Using these two algorithms allows the generation of tracks from raw hit data with any β assumption.

MuonBetaRefit starts with a collection of standard muon tracks produced by MOORE. It then generates seed track collections with β assumptions of $0.8, 0.6, 0.5, 0.4, 0.3$ in order. For each new collection of tracks generated, each track in the new collection is compared with each track in the current collection. If the momentum of the newer track is within $\Delta R < 0.1$ of that of the current track it is considered to be the same track. The version of the track with the lowest fit χ^2/n_{dof} is included in the current collection, the other is discarded. Tracks in the new collection with no duplicate versions already in the current collection are added to the end of the current collection.

5.3.4. Track refitting

After generating the seed tracks, they are individually refitted to find the velocity that gives the optimal fit. "Optimal" in this case is defined as the lowest fit χ^2/n_{dof} achievable. The main objective of MuonBetaRefit is to measure the velocity of slow tracks, but fast tracks, presumably muons, are also refitted to allow checks on the performance of the algorithm.

To reconstruct a track at a given β value, MuonBetaRefit manually recalculates the drift circles of every MDT hit in the track using the modified version of the drift circle reconstruction tool. The altered track is then fitted using the modified version of MooTrackSteering.

The prescription for refitting tracks depends on whether the velocity giving the best fit is significantly below 1.00. To determine this, the track is refitted at $\beta = 1.00$ and $\beta = 0.95$ and the fit χ^2/n_{dof} compared.

If $\beta = 0.95$ has lower χ^2/n_{dof} the track is potentially an SMP, in which case the true β value is unknown. Additionally, failure to refit a track may be due to the seed track finding algorithm omitting hits. As such, if the refitting process fails a new seed track is

generated at fixed low β values to search for hits that may have been omitted in the best fitting seed track. The procedure for finding the optimal β value of a potential SMP is as follows.

1. Track is reconstructed for $\beta = 0.20 \cdots 1.00$ in 0.10 steps.

2. The lowest χ^2/n_{dof} result and the two closest to it in β are taken and a simple quadratic fit of them as a function of β finds the first estimate of $\beta_{optimal}$.

3. Track is reconstructed for $\beta = \beta_{optimal} - 0.10 \cdots \beta_{optimal} + 0.10$ in 0.05 steps.

4. The lowest χ^2/n_{dof} result and the two closest to it in β are taken and a simple quadratic fit of them as a function of β finds the second estimate of $\beta_{optimal}$.

5. Track is reconstructed for $\beta = \beta_{optimal} - 0.02 \cdots \beta_{optimal} + 0.02$ in 0.01 steps.

6. All new χ^2/n_{dof} values are used to fit a quadratic via the least squares method to find the final estimate of the optimal β.

7. The track is reconstructed at the optimal β value and returned.

If either of the neighbouring values in step 2 or step 4 are non-existent due to the track failing to refit, the process fails. If any of the fits do not give a minimum value, give a minimum value at $\beta < 0$ or otherwise fail to converge, the process fails. If the process fails at first, a new collection of seed tracks is generated at $\beta = 0.6$ using all hit data within $\Delta\eta < 0.2$ and $\Delta\phi < 0.2$ of the current track. The new collection is searched to find a track with the same charge and closest momentum direction to the current track. The process is repeated on this new track. If the process fails again, the same is repeated, searching for seed tracks with $\beta = 0.8$. If this also fails then the refit is abandoned.

If $\beta = 1.00$ has lower χ^2/n_{dof} the track is likely to be a muon, in which case the true β value will be very near 1.00. It should have all usable hits already in the track so the refitting process is less involved than for tracks with lower apparent velocity. Altering β only changes the ToF assumption, so it is possible to have an unphysical velocity of

(a) β_{min}=0.963   (b) β_{min}=0.969   (c) β_{min}=0.967
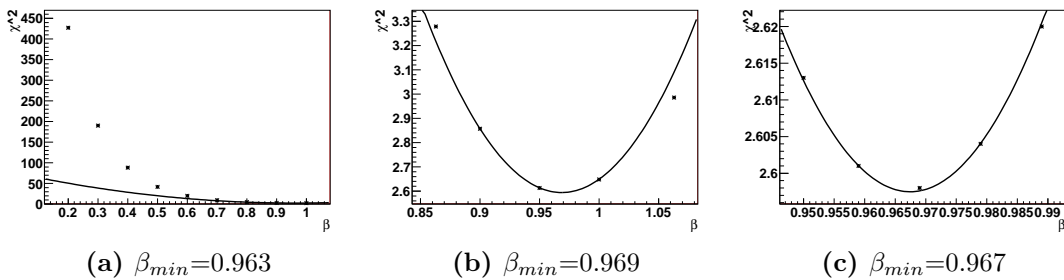
Figure 5.11.: Track refitting of a particle, likely a muon, in data. Particle had lower χ^2 when refitted at $\beta = 0.95$. The refitting steps are shown in separate subfigures: (a) steps 1 and 2, (b) steps 3 and 4, (c) steps 5 and 6.

$\beta > 1$ give the optimal fit, which is why β values up to 1.50 are tested. The procedure for finding the optimal β value of a muon-like track is as follows.

1. Track is reconstructed for $\beta = 0.95 \cdots 1.50$ in 0.05 steps.

2. The lowest χ^2/n_{dof} result and the two closest to it in β are taken and a simple quadratic fit of them as a function of β finds the first estimate of $\beta_{optimal}$.

3. Track is reconstructed for $\beta = \beta_{optimal} - 0.04 \cdots \beta_{optimal} + 0.04$ in 0.02 steps.

4. All new χ^2/n_{dof} values are used to fit a quadratic via the least squares method to find the final estimate of the optimal β.

5. The track is reconstructed at the optimal β value and returned.

If either of the neighbouring values in step 2 are non-existent due to the track failing to refit, the process fails. If either of the fits do not give a minimum value, give a minimum value at $\beta < 0$ or otherwise fail to converge, the process fails. If the process fails, the refit is abandoned.

Refitting the track to find the optimal χ^2/n_{dof} is the preferred method of obtaining tracks. However, this method may fail and cause the refit to be abandoned, even if other hit data from detectors other than the MDT is usable. If the refit is abandoned on a track with RPC hits, the velocity is measured from RPC times (section 5.4.2) and the track reconstructed at that β. If this reconstruction fails, or the track does not have RPC hits, then it is discarded.

5.3.5. Track combination

Refitted tracks are combined with data from the rest of the detector using MUID. No changes are necessary to MUID as its operation does not depend on the β of the track. It is simply set to match muon spectrometer tracks with inner detector tracks and calorimeter information.

1. Refitted track is extrapolated inwards using the MuidBackTracker tool.

2. Extrapolated track is matched with other data and converted to a combined muon object using the MuidMatchMaker tool.

If this combination succeeds, the combined muon is saved for use in analysis. If it does not succeed, the extrapolated track is saved for testing purposes, but is not used in the particle search described in chapter 6.

5.4. Velocity measurements

MuonBetaRefit provides one measurement of track velocity effectively only using the MDT hit information. There are often also hits in the tracks from other technologies which have sufficient time resolution to make velocity measurements. This section explains the different velocity measurements that can be made from the tracks refitted by MuonBetaRefit.

The β measurement resolutions of the various technologies differ significantly. Calibration and reconstruction issues also tend to affect each technology differently. The Calorimeter, while having a similar time resolution to the other two detectors, is much closer to the interaction point, which reduces its β measuring capabilities. The MDT measurement method is very different in nature from that of the RPC and Calorimeter and cannot be carried out in the same stage of the analysis. Additionally, problems with reconstruction of MDT hits can affect all hits in a track at once. The effect of this on results can be minimized by vetoing MDT β measurements with those made by the calorimeter or RPC.

To perform a combined β measurement using all technologies simultaneously it is necessary to appropriately weight all measurement relative to each other. The differences between the technologies and the way they make β measurements make applying a correct weighting scheme difficult. For these reasons the β measurements are made separately for each technology until the final stages of analysis. The combined β value can be calculated by simply taking a weighted average of the β measurements, with each measurement weighted by the inverse square of its expected error.

5.4.1. MDT velocity measurement

The track refitting process performed by MuonBetaRefit finds the optimal β for the MDTs. This is the MDT velocity measurement. If the refitting process fails then no velocity measurement can be obtained for the MDTs.

5.4.2. RPC velocity measurement

The RPC has an effective time resolution of 3.25ns and it consists of multiple layers of detector positioned several meters from the interaction point. This gives it enough sensitivity to accurately measure velocity and identify SMPs.

The RPC hits are given on a strip-by-strip basis. In order to obtain the correct time and position information, the time taken for the hit to propagate along the strip must also be considered. If a ϕ-measuring strip hit and η-measuring strip hit can be found in the same chamber, the line passing though the central lines of these two strips as well as the interaction point is calculated. The intersection of this line with each of those

strips then gives new hit positions, whose distance to the readout (d_{prop}) can be obtained (fig. 5.12). The hit time is modified by

$$t_{new} = t_{old} - \frac{d_{prop}}{v_{prop}} \tag{5.10}$$
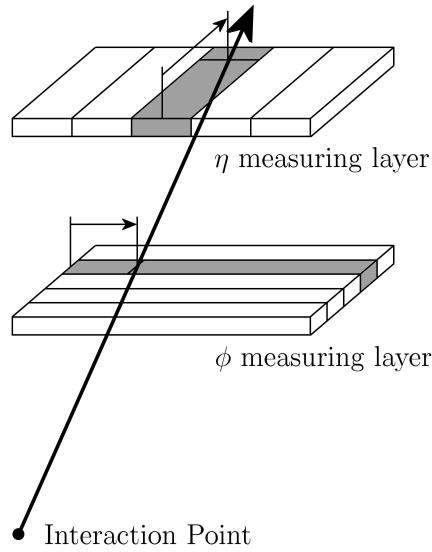
where v_{prop} is the estimated propagation speed ($2 \times 10^8 \text{m/s}$).

Figure 5.12.: RPC strip propagation distance determination in pair of strips making η and ϕ measurements.

The velocity measurement is made through a linear least squares fit of $r = \beta c \times t$, where r is the distance of the hit from the interaction point.

5.4.3. Calorimeter velocity measurement

The tile and liquid argon (LAr) calorimeters have a time resolution similar to the RPC and consist of multiple cells positioned between around two to five metres from the interaction point. This gives the calorimeter system enough sensitivity to measure β corroborating or disputing the measurements made by the RPC and MDT results, but not enough to be useful alone.

Tile and liquid argon calorimeter hits are read from calorimeter cells and require no special adjustments beyond the time calibration described in section 5.5.

The velocity measurement is made through a linear least squares fit of $r = \beta c \times t$, where r is the distance of the hit from the interaction point. The hit times are weighted

proportionally to the energy deposition of the hit. Hits with energy deposition lower than 250MeV are ignored.

5.5. ATLAS Time Calibration

The ATLAS detector is not primarily designed to make time measurements accurate to a few nanoseconds for their own sake but some detector technologies have the ability to do so as a by-product of their design. Additional calibration of the detectors is necessary to maximize the velocity measurement performance.

The timing of detector elements is known to "drift" over time, relative to the LHC clock. We make the assumption that this drift is due to slight differences in the design of the electronics, the temperature inside the detector and the way it is connected to the LHC clock. By this assumption, two modules of the same detector are unlikely to change in relative timing. If we calibrate each element of a detector technology to a standard for that technology, the relative timing of elements should not drift significantly from the standard, although the standard as a whole may drift relative the LHC clock.
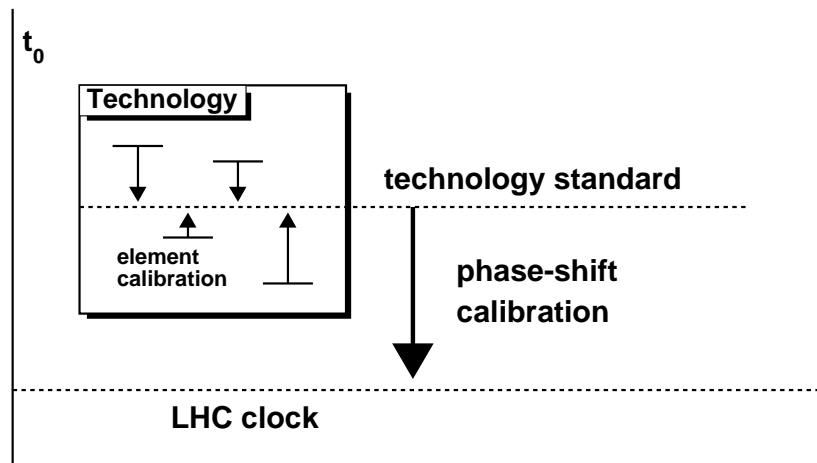

Figure 5.13.: Schematic of the procedure used for hit time calibration. The timing of an element is assumed not to change inside the timing standard for that detector technology. The standard itself, however, can vary relative to the LHC clock.

There are two parts to the time calibration, calibrating the individual elements of a detector technology to a single standard (element calibration) and calibrating this standard to match up with the LHC clock (phase shift calibration). This calibrates all detectors to a common timing standard where bunch crossings take place at $t = 0$ for all events. There is also a final shifting of the measured β value to centre the β distribution of a detector region with similar measurements to $\beta = 1$. This is done to account for remaining systematic problems with the β calculation, predominately in the calorimeter.

To simplify the time calculations, a local time variable $t_0 = t - \frac{r}{c}$ is defined, where r is the distance from the interaction point. A particle travelling in a straight line at $\beta = 1$ is expected to arrive at any position in the detector at $t_0 = 0$ for that position. To calibrate a detector, measured hit t_0s from particles with known true t_0s are required. $Z \to \mu\mu$ events are used to provide high quality muon tracks with known $\beta \approx 1$ ($t_0 = 0$). Track bending in the magnetic field at ATLAS has a negligible effect on the time of flight for muons with momentum this large.

5.5.1. Element calibration

We create a timing standard for each detector technology and calibrate each element of that technology to match it.

- The MDT, by design, needs good time resolution at the time of reconstruction because of how MDT drift circles are reconstructed. Since the timing requirements of this study are higher than the level available in standard reconstruction, further calibration is preferred.

- The RPC requires good time resolution for triggering, but this is performed at the hardware level and is not calibrated at the reconstruction stage. The RPC elements are approximately set up for particles to arrive at $t_0 = 100$ns and triggers on signals between 0ns < t < 200ns. The RPC cannot, therefore, be used in this study without calibration.

- The calorimeters have good time resolution for triggering and while this is performed at the hardware level the values are, unlike the RPC, usable without calibration. Calibration is still preferred in order in increase velocity measurement performance.

The MDT and RPC both had time calibration databases available at the time of this study from their respective groups. A custom database was generated for the calorimeters for the purpose of this study. The calorimeter database was generated by calculating the mean t_0 measurement ($\bar{t}_{0element}$) of each detector element for a dataset of $Z \to \mu\mu$ muon tracks. The hit time for a detector element can then be calibrated to the standard for that technology by

$$t_{\text{calibrated}} = t_{\text{uncalibrated}} - \bar{t}_{0\text{element}}. \tag{5.11}$$

The RPC and Calorimeter databases calibrate each strip and cell individually. The MDT database calibrates each chamber, as the tubes inside a chamber already need to be well calibrated with each other to reconstruct segments correctly.

5.5.2. Phase shift calibration

The timing standard of a technology, as established above, is calibrated to the LHC clock on a per-run basis. The time deviation that occurs during a run has been confirmed to be small. The databases are generated from histograms filled with element calibrated t_0 measurements from each technology. These histograms are generated on a per-run basis and the central value ($\mu_{technology-run}$) found by applying a Gaussian fit over the range of the central peak. The hit time for a detector element in a particular run can then be calibrated to the LHC clock by

$$t_{\text{calibrated}} = t_{\text{uncalibrated}} - \bar{t}_{0\text{element}} - \mu_{\text{technology-run}}. \tag{5.12}$$

5.5.3. β shift calibration

Calibrating the times as described in the last two sections assumes that the time measurements are relatively evenly distributed around a peak and that if this peak is moved to $t_0 = 0$ then the β measurement distributions will be corrected. These calibrations do not, however, account for any systematic bias towards t_0 measurements on one side of the peak.

In the calorimeter the peak represents particles creating electrons very close to the electrodes or scintillators, however there is a small bias towards measurements after the peak due to signal delays from the electron drift time. The drift time in the RPC is minimal and the MDT takes drift radius into account, largely eliminating the bias, but it cannot be directly corrected in the calorimeter.

The detector is split into η regions for each technology according to measurement accuracy, giving regions with similar levels of accuracy. A Gaussian is fitted to the β measurement distribution in each of these regions for each detector technology. The results of these fits, before applying the β shift, are shown in table 5.1 on page 89. It is clear from the table that this shift negligibly affects the MDT and RPC but has a noticeable effect on the calorimeter. β measurements from hits with fully calibrated t are shifted by the difference between the centre of this Gaussian and $\beta = 1$ to give the final, fully calibrated, β measurement.

5.5.4. Effectiveness of time calibration

Figure 5.14 shows the effect of the time calibration steps and the β shift on β measurements. The effect of calibration on β and hit t_0 distributions inside the η regions with different measurement accuracy is examined in detail in appendix B.

The calibration of detector elements is necessary for making measurements with the RPC and also greatly improves the accuracy of calorimeter measurements. Phase shift calibration also noticeably improves resolution for the RPC and the MDT, but there
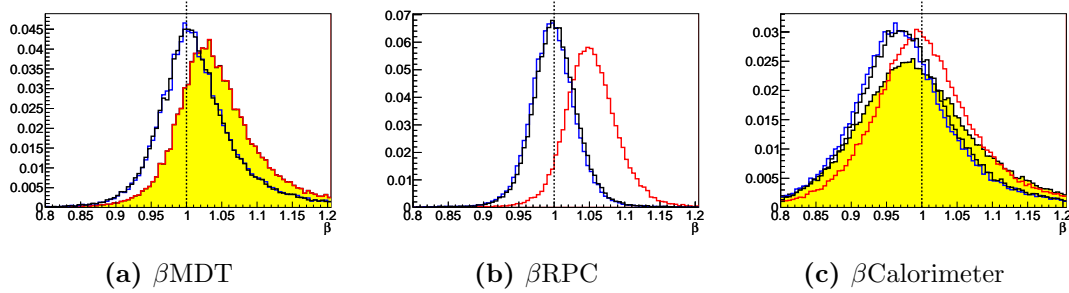
(a) βMDT   **(b)** βRPC   **(c)** βCalorimeter

Figure 5.14.: β measurements made with no calibration (yellow fill), element calibration (red line), element+phase shift calibration (blue line) and β shift (black line) for the (a)MDT, (b)RPC and (c)Calorimeter using the JetTauEtMiss stream. The RPC cannot make measurements with no element calibration. The histograms have each been scaled to have integrals equal to one.

seem to be some systematic problems remaining with β measurement in the calorimeter for tracks in E_T^{miss} triggered events.

Comparing the hit t_0 distributions for events triggered on the single muon trigger and the E_T^{miss} trigger reveals that calorimeter t_0 from E_T^{miss} triggered events is further biased towards late arrival (fig. 5.15). This bias on β is exacerbated by the relatively short distance of the calorimeter from the interaction point. The bias is small enough not to be observable in the overall β results in section 5.6 and is largely accounted for in searches by the background estimation process. As such, no attempt to correct it was made.
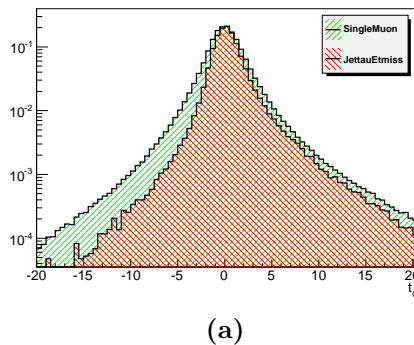

(a)

Figure 5.15.: Fully calibrated calorimeter t_0 measurements made on events with the E_T^{miss} (red) and single muon (green) triggers. The E_T^{miss} trigger has a noticeable bias towards late hit times despite having its peak correctly calibrated, the single muon triggered events have a much lower bias.

Overall, calibration gives a significant increase in β measurement accuracy, enables the use of the RPC and allows us to consider each measurement made of β to have

mismeasurement largely independent of those of other measurements. [1] The β measurement accuracy for the different detectors on data and Monte Carlo will be discussed in section 5.6.

5.5.5. Database scope and possible improvement of calibration

From the initial assumption that the timing of elements inside a single detector technology would not change significantly over time, one set of detector element calibration databases was generated for the entire 2011 run period. It is likely that this assumption was not entirely correct as the detectors were not left completely undisturbed for that entire period. Re-configuration of detectors, off-lining of chambers, hardware faults and other factors would have changed the timing of some detector elements to a degree. It is likely that better calibration could be obtained by conducting the calibration on a per-period basis. However there are numerous difficulties with implementing this more rigorous approach to calibration.

Firstly, it would have been much more difficult to manage many different versions of the large databases for the RPC and Calorimeter.

Secondly, the calibration databases would have taken too much time to generate. Although databases for the MDT and RPC could be generated in the same way as for the calorimeter, there are not enough $Z\rightarrow\mu\mu$ events to generate calibration databases with sufficient statistics on a per-period basis. The much larger single muon datasets could be used to increase statistics, however whilst reprocessing $Z\rightarrow\mu\mu$ datasets can take a few days, the single muon datasets can take weeks. The MDT β and time measurements cannot be taken outside of the reconstruction environment, so updating the MDT calibrations does require re-processing the entire dataset.

The calibration databases sometimes had to be updated if a bug was found, or an improvement implemented. Increasing the size of the calibration dataset to this extent would have added too much time to the study.

For similar reasons, the scope of calibration of detectors to the LHC clock was limited to a per-run basis. Performing calibration on a finer time scale would better account for drifts in timing during a run, but would require significantly more statistics.

5.6. β Measurement Performance

This section presents the performance of the methods of measuring particle velocity (β) described in section 5.4 with the calibrations described in section 5.5 taken into account.

---

[1]Without the phase shift calibration, mismeasurement of β is correlated between tracks and technologies in the same event by the phase shift.
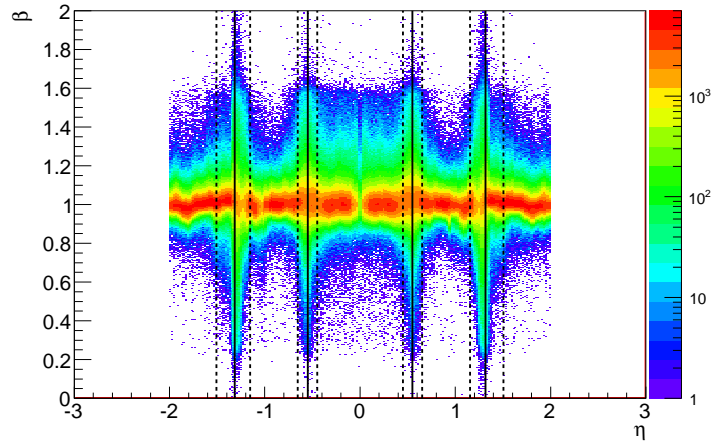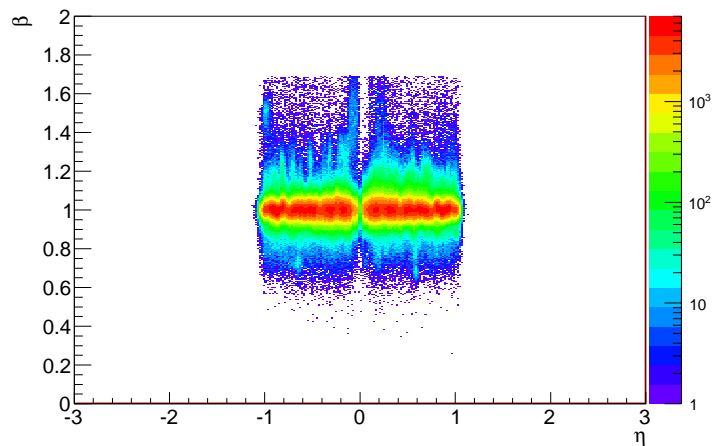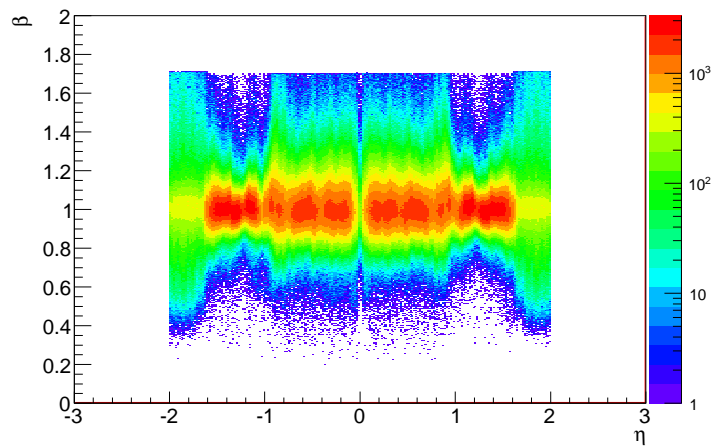
(a) MDTβ vs η

(b) RPCβ vs η

(c) Caloβ vs η

Figure 5.16.: Distributions of β measurements vs track η. (a) MDT measurements are unreliable around the 30° and 60° regions indicated by solid lines, dashed lines represent a $\pm 5°$ boundary. (b) RPC distribution does not have any unreliable regions. (c) Calorimeter measurements vary in resolution significantly, depending on the η region.

Before presenting the final performance, two preceding subsections describe additional considerations that must be taken. Section 5.6.1 explains issues with using the MDT to make β measurements when track $\theta \approx 30°, 60°$. Section 5.6.2 describes the smearing of MC that was conducted to have MonteCarlo results best match those obtained from data.

Section 5.6.3 will then show the accuracy of the algorithm on muon data, along with Monte Carlo muon results for comparison. Finally, the effectiveness at measuring the velocity of SMPs in Monte Carlo will then be analysed in section 5.6.4.

The calibration is done using $Z \rightarrow \mu\mu$ data and combined results from the whole of 2011 are used to analyse performance.

5.6.1. MDT β measurements at $\theta \approx 30°, 60°$

Figure 5.16 shows β measurements made with each technology plotted against the track η direction. β measurements made with the MDT are clearly unreliable in regions corresponding to $\theta \approx 30°, 60°$. Measurement accuracy varies depending on the detector region for the other technologies, but not to the same extent.

If there is no strong relationship between the goodness of fit of a track and the size of its drift circles, the MDT measurement will fail. The MDT tubes line up at 30° in the endcap and at 60° in the barrel so changes to the drift circle size for tracks travelling at this angle do not affect the fit quality as much as in other regions (fig. 5.17).

MDT β measurements from tracks with momentum direction $\theta = 30° \pm 5$ and $\theta = 60° \pm 5$ are thus discarded. The calorimeter covers both of these regions, but is
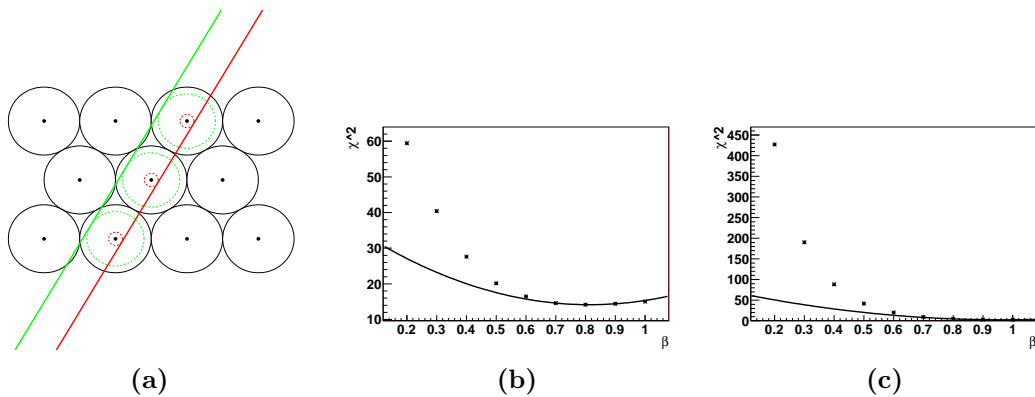

| (a) | (b) | (c) |

Figure 5.17.: (a) Diagram of drift circle reconstruction ambiguity. True muon track and drift circles (green) have similar fit quality to those of a low β fit (red). (b) Fit χ^2 vs β distribution for $\theta = 60°$ track. Maximum χ^2 is 60. (c) Fit χ^2 vs β from another region of the detector. Maximum χ^2 is 450. $\theta = 60°$ region has less well defined χ^2 distribution, a minimum at a higher χ^2 value and at the wrong β.

too close to the interaction point to provide accurate measurements of β alone. Since the $\theta = 60°$ region of the detector is covered by the RPC, β measurements can still be obtained from the muon spectrometer in that region. The $\theta = 30°$ region, however, is only covered by the TGC, which does not have sufficient time resolution to measure β. There is no way to make more accurate β measurements in this region.

5.6.2. Smearing of Monte Carlo simulation

Even with calibration, the β measurement resolution obtained in real data is not as good as that predicted by Monte Carlo simulation. The Monte Carlo does not suffer from calibration problems and hardware faults.

The simulation of the time measurement should reproduce the data behaviour as closely as possible in order to get accurate estimates of the signal acceptance when processing SMP Monte Carlo. This is done by smearing the time measurements by a random value drawn from a Gaussian distribution centred on zero of width (σ) tuned to smear the correct amount for each detector. The width is given by

$$\sigma_{smear} = \sqrt{\sigma_{data}^2 - \sigma_{MC}^2} \tag{5.13}$$

where σ_{data} and σ_{MC} are the widths of Gaussian functions fitted to the t_0 distributions from the data and Monte Carlo, respectively. Values of σ_{smear} are computed for each detector technology and are applied to track hits before MuonBetaRefit begins track refitting.
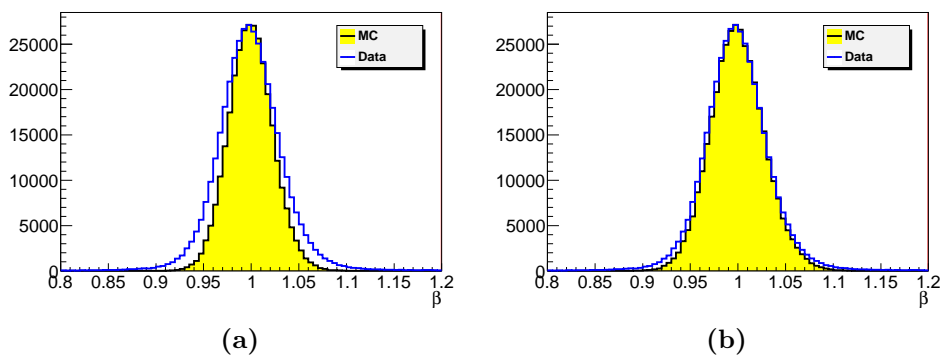

(a)   (b)

Figure 5.18.: RPC β measurements from data and Monte Carlo with (a) no smearing applied (b) time smearing applied to the Monte Carlo

Figure 5.18 shows the β measurements obtained before and after the smearing for the RPC. The effect is similar for measurements made by the other detector technologies. The smearing does not allow the Monte Carlo to simulate mismeasurement of β due to far outlying hit times but rather represents the limitations on time resolution of the technology by widening the peak.

Since the Monte Carlo is not used to estimate background in chapter 6, it is only necessary to smear it to the extent that rejection of GMSB signal due to mismeasurement of β is correctly estimated. An estimation of the maximum systematic error in signal acceptance that could be introduced by the remaining difference between data and Monte Carlo is made in section 6.4.

5.6.3. β measurement performance on muon data

Particles in the single muon datastream were analysed by MuonBetaRefit and β measurements were obtained from the MDT, RPC and calorimeter technologies. This section presents the overall β measurement capability of this method and examines the differences in measurement accuracy of the different detectors and different regions of the detector.

Figure 5.19 shows an overall map of the averages of β measurements made at different η and ϕ locations. Although there remain a few regions in the MDT and RPC that suffer from miscalibration, the β average is generally close to 1.0. The white areas of these histograms represent areas where that technology has no usable coverage.

From figure 5.16 it is clear that the β resolution of a detector depends on the η region of the detector. Different numbers of detector stations are available in different η regions. In general, the detectors in the barrel region are closer to the interaction point than in the endcap, reducing the leverage in β calculations. No significant variation in β resolution was observed in ϕ.

For analysis, each detector is split into individual η regions with similar β resolution. The β distributions inside these regions are presented in appendix A along with reasoning for the regions chosen. For the purposes here of demonstrating the β measurement properties and comparing with Monte Carlo the results across multiple η regions are merged. The MDT histograms are presented for the barrel region of the detector ($|\eta| < 1$) and the endcap region ($|\eta| > 1$) separately. Since the RPC β resolution only increases slightly with the increasing distance from the IP, its results are shown on a single histogram. The calorimeter β resolution varies significantly with η. This is not surprising as the calorimeter technologies used in different η regions also varies significantly. The calorimeter, however, plays a smaller part in the SMP study than the MDT and RPC (it is mainly used to veto measurements from the MDT and RPC) so results are shown on a single histogram.

Figure 5.20 shows linear histograms around the peak of the β measurement distributions for all detector technologies. The MDT β resolution is noticeably better in the endcap than the barrel due to the greater distance from the interaction point. The RPC has similar resolution to the MDT endcap. The calorimeter has far worse resolution than the MDT or RPC, but has its peak correctly calibrated to $\beta = 1$ in data. The Monte Carlo peak is slightly offset, although not to a degree likely to affect results.

The results of Gaussian fits to histograms in the η regions used for analysis are shown in table 5.1 (on page 89). The histograms were generated for run periods b-k and l&m
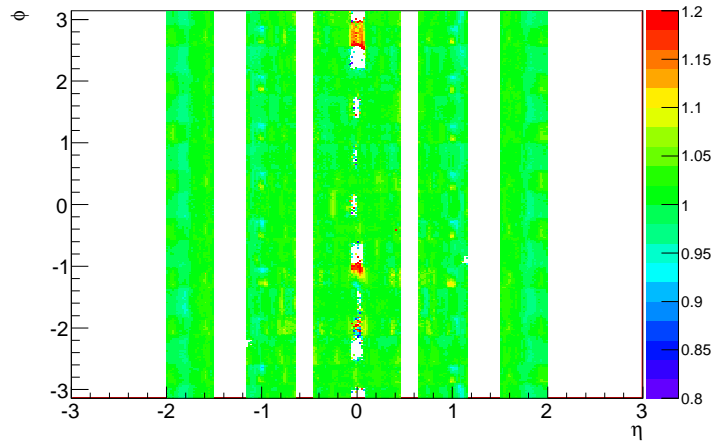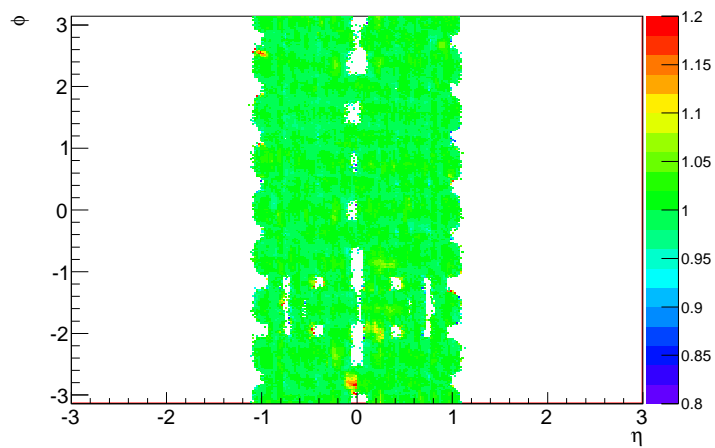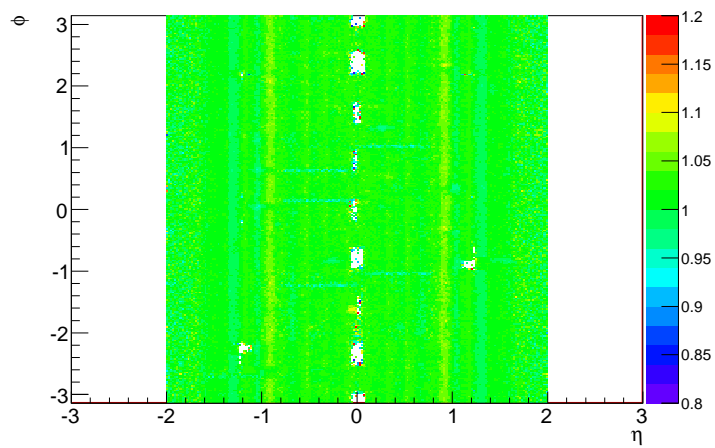
(a) MDT β map

(b) RPC β map

(c) Calorimeter β map

Figure 5.19.: Map of average β in η-ϕ for the (a)MDT (with $30°, 60°$ regions excluded), (b)RPC, (c)Calorimeter.

η_{low}	η_{up}	μ	σ
-2.0	-1.3	0.9943	0.02454
-1.3	-0.5	1.0005	0.02967
-0.5	-0.1	1.0051	0.03948
-0.1	0.1	1.0065	0.04135
0.1	0.5	1.0058	0.04007
0.5	1.3	1.0012	0.02991
1.3	2.0	0.9971	0.02432

(a) period b-k MDT

η_{low}	η_{up}	μ	σ
-1.2	-0.5	0.9972	0.02541
-0.5	-0.1	0.9974	0.03099
-0.1	0.1	0.9953	0.0309
0.1	0.5	0.9966	0.03107
0.5	1.2	0.9969	0.02549

(b) period b-k RPC

η_{low}	η_{up}	μ	σ
-2.0	-1.6	0.9737	0.09346
-1.6	-1	0.9882	0.0576
-1	-0.1	0.9839	0.09104
-0.1	0.1	0.9787	0.09758
0.1	1	0.984	0.09144
1	1.6	0.9879	0.05858
1.6	2.0	0.9734	0.09154

(c) period b-k Calo

η_{low}	η_{up}	μ	σ
-2.0	-1.3	0.9966	0.03409
-1.3	-0.5	0.9995	0.03538
-0.5	-0.1	0.9962	0.04381
-0.1	0.1	1.0046	0.04373
0.1	0.5	0.9981	0.04392
0.5	1.3	1	0.03537
1.3	2.0	1.0008	0.03287

(d) period l&m MDT

η_{low}	η_{up}	μ	σ
-1.1	-0.5	0.9953	0.0285
-0.5	-0.1	0.9949	0.03536
-0.1	0.1	0.9948	0.03553
0.1	0.5	0.9968	0.03484
0.5	1.1	0.9968	0.0288

(e) period l&m RPC

η_{low}	η_{up}	μ	σ
-2.0	-1.6	0.9761	0.09674
-1.6	-1	0.9895	0.05828
-1	-0.1	0.9838	0.09119
-0.1	0.1	0.98	0.09737
0.1	1	0.9845	0.09228
1	1.6	0.9881	0.05927
1.6	2.0	0.9712	0.09343

(f) period l&m Calo

Table 5.1.: Centre (μ) and width (σ) of Gaussian fits to the β measurement distributions from different technologies for tracks in different η regions ($\eta_{low} < \eta < \eta_{up}$) of the detector, data is almost entirely $\beta \approx 1$ muons. Due to adjustments made after period k, the muon spectrometer has different β measurement resolution in periods l&m. These values are taken after all time calibrations, but before the final β shift, the shift magnitude is (1-μ).

separately due to changes in the ATLAS hardware made after period k that affected β measurement accuracy. These histograms are made before applying the β shift described in section 5.5.3; their central value is used to calculate the shift applied. The widths of the Gaussian fits are used to weight β measurements from individual technologies when calculating the average β of a track.

The logarithmic distributions (fig. 5.21) show the "tails" of the measurement distributions. The MDT has significantly more tail predicted in the Monte Carlo than is observed in the data. The excessive tail at low β in the Monte Carlo is caused by a corresponding tail in high t_0 measurements. These outlying hits are included in tracks to a greater degree in the Monte Carlo than in data, the reason for which is not known. There is little difference in the tail between the endcap and barrel regions in the results from data. This follows, as the tail is mainly caused by total mis-reconstruction of drift circles, and as such would not be affected by distance from the interaction point. The tail of the RPC distribution drops more quickly than that of the MDT. This behaviour is expected due to the more rigidly defined time measurements made by the RPC. The calorimeter shows a significant tail, far more than the other technologies. This is caused by moderate tails in the t_0 distribution being exaggerated by the close proximity of the calorimeter to the interaction point along with the comparatively low number of hits.
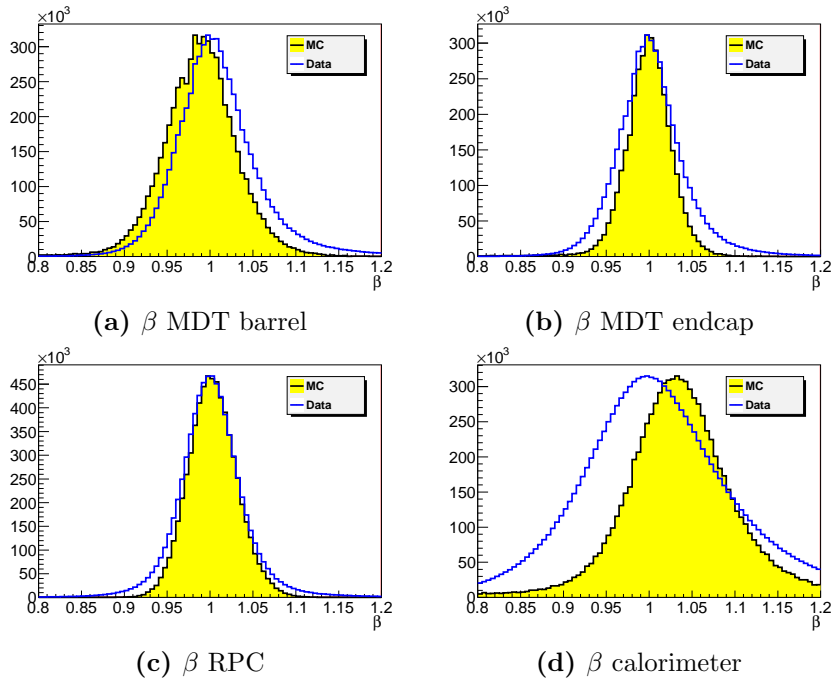
Figure 5.20.: Linear histogram of the central peak ($0.8 < \beta < 1.2$) in the distribution of β measurements made by the: MDT in the (a)barrel and (b)endcap; (c)RPC; (d)calorimeter.
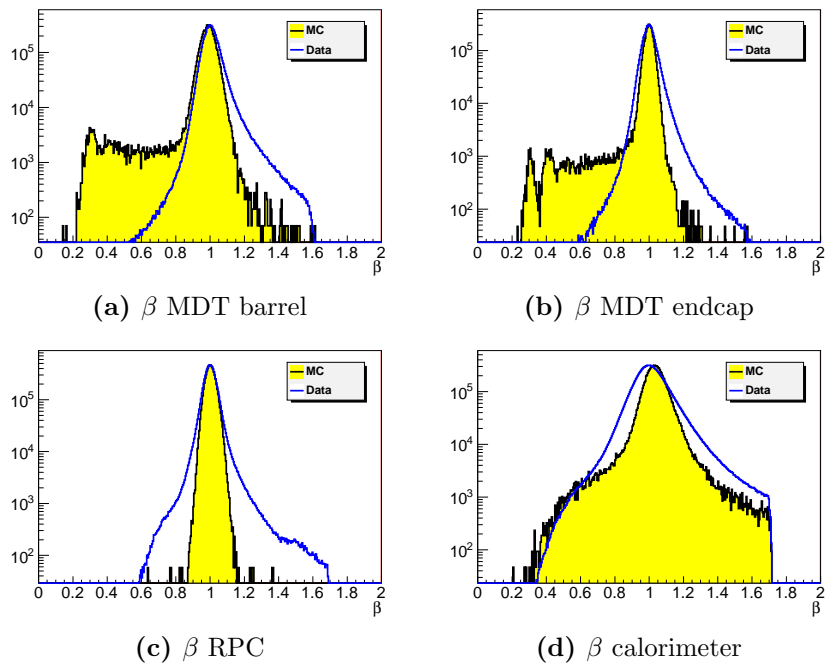

Figure 5.21.: Logarithmic histograms of the full range of β measurements made by the: MDT in the (a)barrel and (b)endcap; (c)RPC; (d)calorimeter.
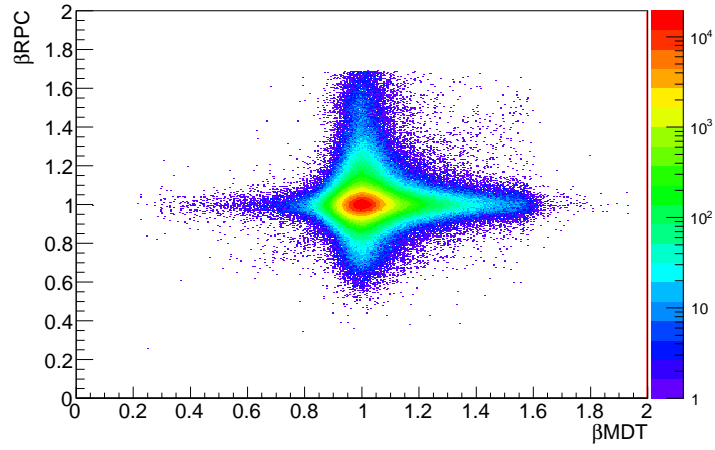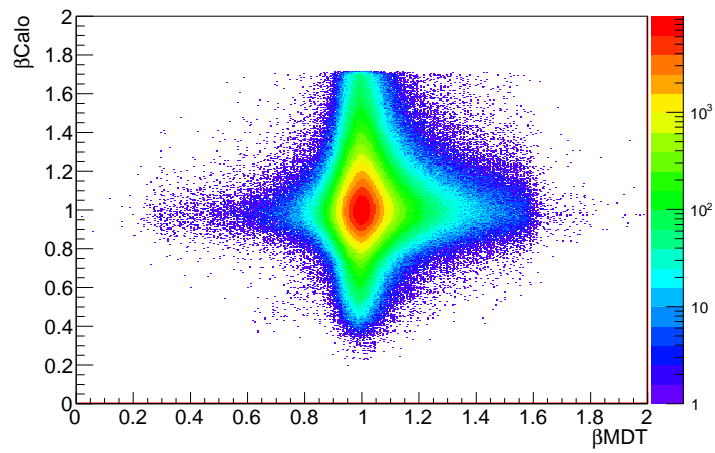
(a) βMDT vs βRPC

(b) βMDT vs βCalorimeter

(c) βRPC vs βCalorimeter

Figure 5.22.: Comparisons of β measurements made on a muon data sample by different technologies (a)MDT vs RPC, (b)MDT vs Calorimeter, (c)RPC vs Calorimeter. There is no evidence of correlation between βs measured by the different technologies
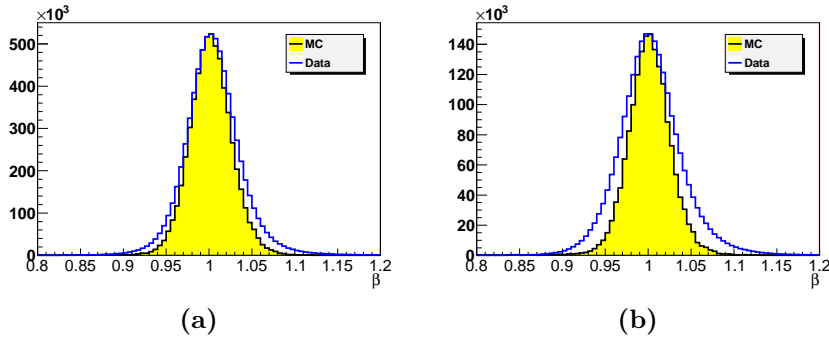
Figure 5.23.: Linear histogram of the central peak ($0.8 < \beta < 1.2$) of the combined β distribution in the (a) barrel and (b) endcap.

Figure 5.22 shows comparisons of the β measurements made by the different technologies for the same track using a $\beta \approx 1$ data sample. The measurements made by different technologies appear to be independent, aside from a small number of outliers. There are a small number of apparently correlating low β outliers visible at $\beta < 0.8$ in all plots. The measurements from the MDT and RPC are well correlated, but the outliers in calorimeter plots have a much lower measured β. The calorimeter would measures a lower β than the MDT and RPC due to its shorter distance to the interaction point if this were an issue with timing rather than an SMP signal. This correlation also appears to extend into the high β region, which could only be caused by a timing issue. Overall, these distributions show that mismeasurement of β by the various technologies can largely be considered to be independent.

Figures 5.23 and 5.24 show the results of combining the β measurements from the various technologies. The combination is performed through a weighted average with each β measurement weighted by $1/\sigma_{tech}^2$, where σ_{tech} is the width of the appropriate β distribution, as shown in table 5.1. An additional consistency cut is applied that at least two of the β measurements made are within $2\sigma_{tech}$ of the combined β measurement. The combined β measurement in data exhibits slightly better β resolution in the barrel than the endcap, due to the presence of both the RPC and MDT. The combined β resolution in the endcap is not noticeably improved over MDT resolution by the inclusion of the calorimeter. Requiring that the two β measurements available in the endcap are consistent, however, greatly reduces the tail of the distribution in both the barrel and the endcap.

5.6.4. β measurement performance on SMP Monte Carlo

Having studied the accuracy of β measurements on muon sources, we now move onto simulations of SMP particles. The sample used for reference in this section is of sleptons from the GMSB model with $\Lambda = 100, \tan\beta = 10$, which has long lived $\widetilde{\tau}$s with masses of 310GeV.
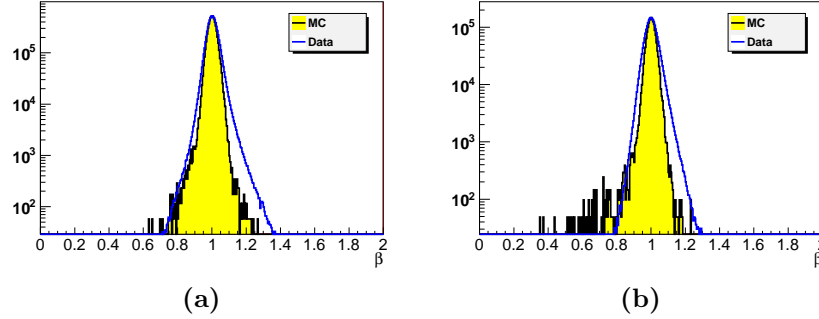
(a)   **(b)**

Figure 5.24.: Logarithmic plot of the full range of the combined β distribution in the (a) barrel and (b) endcap.

The mismeasurement of β is expressed as

$$d\beta = \frac{\beta_{measured} - \beta_{truth}}{\beta_{truth}} \tag{5.14}$$

Particles with lower β_{truth} have longer flight times to the detectors. This reduces the effect of detector time measurement error on the measured time of flight and increases β resolution. Expression 5.14 takes into account the higher β resolution detectors are likely to have on particles with low β_{truth}.

Figure 5.25 shows how the mismeasurement of β varies with a the true β of a particle. Looking at subfigures (a), (b) and (c) shows that the mismeasurement of all detectors is relatively constant through the IPβ_{truth} range. The RPC exhibits almost no outlying hits and high measurement accuracy, it can therefore act as a control for analysing the results from other technologies. The MDT shows decreased far-outlying mismeasurement at lower β_{truth}. These outliers are caused by complete mis-reconstruction of drift circles and have no relation to the real particle ToF, but must be inside the time window for MDT acceptance. The width of this window in $d\beta$ is suppressed by the denominator in equation 5.14; the outliers are correspondingly suppressed. Outliers in positive $d\beta$ appear to increase in $d\beta$ magnitude for the calorimeter with decreasing β_{truth}. This is due to $\beta \approx 1$ SM background being included in an SMP track.

For particles travelling at low β the rate of energy loss per unit distance is approximately proportional to $1/\beta^2$. The amount of energy lost by SMPs during transit through the calorimeter is thus heavily dependent upon their true β. Figure 5.25 subfigures (b) and (d) show the RPC mismeasurement of the β_{truth} reported at the interaction point and in the muon spectrometer. Comparing the two histograms shows that β_{truth} decreases noticeably for slower moving particles during transit through the detector, but not for faster moving particles. Most of the energy loss of a particle occurs in the calorimeter before reaching the muon spectrometer. Even the calorimeters themselves will measure a lower β than the particle had at the interaction point as it is measured over the entire length of the calorimeter, not just upon entry. The apparent mismeasurement of IPβ
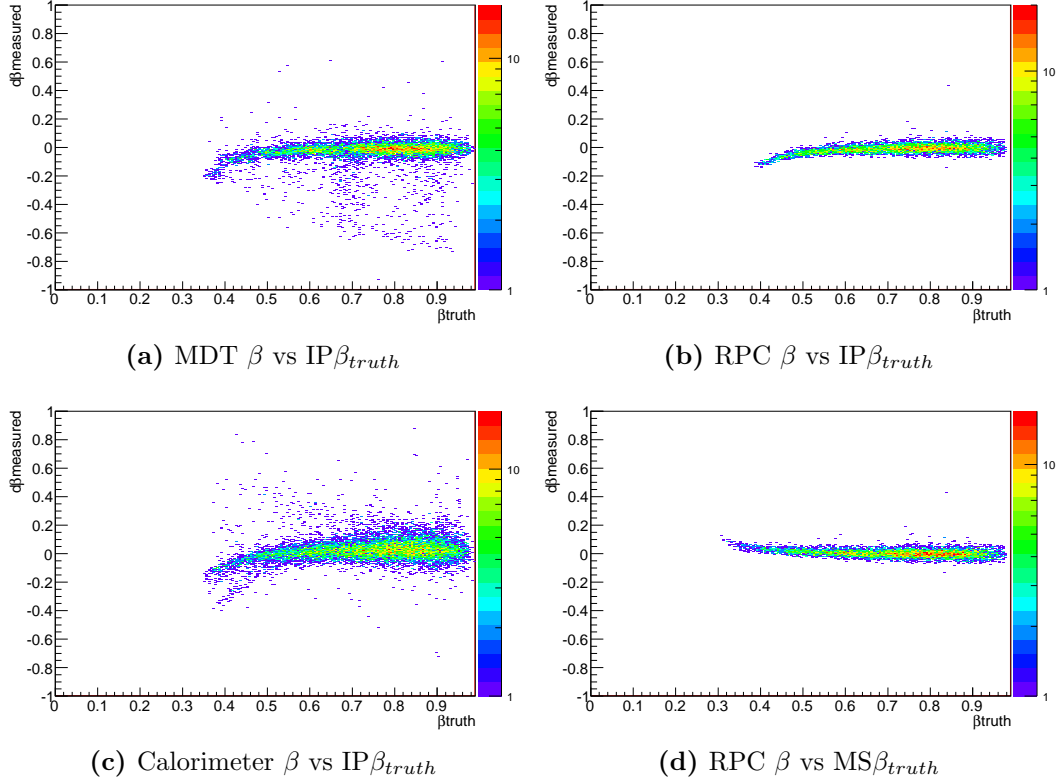
(a) MDT β vs IPβ_{truth}

(b) RPC β vs IPβ_{truth}

(c) Calorimeter β vs IPβ_{truth}

(d) RPC β vs MSβ_{truth}

Figure 5.25.: β mismeasurement plotted against particle true β at the interaction point (a)MDT, (b)RPC, (c)Calorimeter, (d)RPC mismeasurement vs particle true β in the muon spectrometer

observed for lower β_{truth} values then is not related to β measurement error, but is a natural consequence of ATLAS' geometry.

It may be possible to correct this underestimation of particle IPβ by accounting for particle energy deposition in the calorimeter or by simply shifting lower β measurements to match simulation. These methods, however, depend on the mass of the SMP, which is not known as a prior. The decision was made not to attempt to correct underestimation of IPβ in this study. Since the search is mainly concerned with finding slow moving particles, an underestimation of IPβ is not likely to affect signal acceptance.

5.6.5. Discriminating power

The SMP search in chapter 6 uses a β threshold of 0.95 to discriminate between SMP candidates and muons. Table 5.2 shows the percentage of β measurements below this threshold for fully calibrated muon data and $\Lambda = 100, \tan\beta = 10$ sleptons, the results are separated into the previously established η regions of the detector.

		muon			SMP		
η_{low}	η_{up}	$\beta < 0.99$	$\beta < 0.95$	$\beta < 0.90$	$\beta < 0.99$	$\beta < 0.95$	$\beta < 0.90$
-2.0	-1.3	37.62	8.91	0.62	97.05	83.11	59.25
-1.3	-0.5	37.41	9.08	1.11	99.55	97.17	87.18
-0.5	-0.1	38.38	12.22	1.79	99.45	98.61	94.54
-0.1	0.1	36.66	11.26	1.47	99.43	97.13	91.76
0.1	0.5	38.37	12.33	1.69	99.77	98.66	92.24
0.5	1.3	37.94	9.58	1.19	99.46	96.73	84.30
1.3	2.0	37.08	8.43	0.54	99.06	90.31	67.81

(a) MDT

		muon			SMP		
η_{low}	η_{up}	$\beta < 0.99$	$\beta < 0.95$	$\beta < 0.90$	$\beta < 0.99$	$\beta < 0.95$	$\beta < 0.90$
-1.2	-0.5	38.15	9.02	1.71	99.44	96.64	85.29
-0.5	-0.1	39.96	12.12	2.28	99.51	98.03	90.95
-0.1	0.1	39.16	11.49	2.14	99.70	97.56	90.24
0.1	0.5	37.73	9.93	1.65	99.76	97.94	92.20
0.5	1.2	36.21	7.40	1.43	99.38	96.58	86.20

(b) RPC

		muon			SMP		
η_{low}	η_{up}	$\beta < 0.99$	$\beta < 0.95$	$\beta < 0.90$	$\beta < 0.99$	$\beta < 0.95$	$\beta < 0.90$
-2.0	-1.6	44.93	33.27	22.78	87.88	84.85	81.82
-1.6	-1	42.18	20.19	5.96	92.52	80.58	62.52
-1	-0.1	43.37	27.93	13.40	92.24	85.89	74.61
-0.1	0.1	43.60	29.21	15.26	93.58	87.58	78.80
0.1	1	43.32	27.91	13.37	92.28	86.25	75.60
1	1.6	42.14	20.26	5.90	91.68	80.32	62.41
1.6	2.0	44.57	32.57	22.07	94.44	88.89	72.22

(c) Calo

Table 5.2.: Percentages of β measurements made in the MDT, RPC and calorimeter's η regions below the β thresholds. SMP is GMSB_100_10 $\widetilde{\tau}$

Some slepton signal is lost due to measurement inaccuracy but most loss of signal is due to sleptons genuinely travelling faster than $\beta = 0.95$. A slepton with β measured lower than 0.95 by one detector is likely to have all other β measurements lower than 0.95. For muons, however, $\beta < 0.95$ results are random as they can only be returned through mismeasurement. Requiring that more than one detector technology measures $\beta < 0.95$ should reduce the muon background fraction to 2.6% even in the worst case (MDT and calorimeter only, $-0.1 < \eta < 0.1$).

5.6.6. Concluding remarks on β measurements

β measurements are required to be accurate to correctly estimate particle mass as well as reduce muon background. It is clear that most of the β measuring resolution will come

from the MDT and RPC technologies. The calorimeter may still be used, but must be weighted so as not to upset the other results.

The most useful application of the calorimeter in this search may be through giving all the technologies the ability to veto the SMP candidacy of a track. As all the different technologies give independent mismeasurement in β, we can reduce the background by requiring that all technologies independently reconstruct a β below the $\beta = 0.95$ threshold. The majority of SMPs will have velocities lower than the threshold so signal acceptance should not be significantly affected.

Chapter 6.

Charged stable massive particle search

A search for pair produced GMSB sleptons is now conducted using the methods for β measurement described in chapter 5. The essence of the search is to find muon-like tracks with abnormally low velocity and re-calculate the particle mass, looking for irregularities. Cross section upper limits will then be calculated at the 95% confidence level and compared with the theoretical cross sections. Datasets and selection criteria applied are described in sections 6.1 and 6.2. Expected background for this search method is discussed in section 6.3. Results of this search, the statistical calculation method used and the cross sections which can be excluded are presented in sections 6.5, 6.6 and 6.7.

6.1. Datasets and simulation samples

The datastreams useful in a search for the GMSB $\tilde{\tau}$ are explained in section 4.3. Datasets corresponding to data taking throughout 2011 using the appropriate datastreams are used. With [*] representing all run periods in 2011, the specific datasets used in analysis are: (see also section 4.3.2 for nomenclature)

- data11_7TeV.period[*].physics_Muons.PhysCont.DESDM_SGLMU.pro10_v01/

- data11_7TeV.period[*].physics_JetTauEtmiss.PhysCont.DESDM_RPVLL.pro10_v01/

Calibration databases are obtained from

- data11_7TeV.period[*].physics_Muons.PhysCont.DESD_ZMUMU.pro10_v01/

The simulation samples used are detailed in section 4.1.

6.2. Data selection

Selection criteria for data is be defined to ensure that background is rejected as much as possible. Since the main source of background is β mismeasurement, background can be greatly reduced by only accepting β measurement results from reliable tracks. Standardising the selection of data to a defined set of triggers allows accurate estimates of signal acceptance to be derived from simulations.

After excluding runs for which no calibration constants could be calculated and applying the most recent Good Run List the total integrated luminosity is 4.06fb^{-1} out of the 5.25fb^{-1} ATLAS recorded integrated luminosity.

Selection criteria are defined at the event, track, β-measuring technology and β levels. Event selection manages the results of trigger algorithms and cuts events taken during periods with known hardware problems. Track selection removes tracks not passing very basic criteria for sleptons identification. Tracks passing through areas of the detector from which reliable β measurements cannot be made are also cut. Technology selection removes unreliable β measurements from a track based on how much information was available from the technology when making the measurement. β selection establishes whether the remaining β information is sufficient and defines the final set of criteria for a track to be a slepton candidate.

6.2.1. Event selection

When selecting datasets in chapter 4 single muon and E_T^{miss} triggers were found to be effective at identifying events with charged SMPs. The specific single muon and missing E_T^{miss} triggers used are defined in section 4.3.1.

Events read from the Single Muon stream are required to have passed the single muon trigger. This trigger finds tracks in the muon spectrometer with measured $p_T > 18\text{GeV}$ in the range $|\eta| < 2.4$.

Events read from the Jet-Tau-E_T^{miss} miss stream are required to have passed the missing E_T trigger, but to have failed the single muon trigger. This avoids the possibility of counting an event twice if it was present in both streams.

A generic Good Run List indicating that the whole detector is functioning normally is applied, specifically

- data11_7TeV.periodAllYear_HEAD_CoolRunQuery-00-04-08_All_Good

6.2.2. Track selection

To increase the reliability of track reconstruction, tracks produced by MuonBetaRefit are required to have been successfully combined with inner detector tracks and to contain hits from at least two muon spectrometer stations.

The CSC is not used to make β measurements and the lack of an inner-station MDT detector at $|\eta| > 2$ results in decreased measurement resolution. A transverse momentum cut is also applied to track momentum to remove the majority of QCD background. Tracks with momentum vector $|\eta| > 2$ or $p_T < 30\text{GeV}$ are removed.

All events are scanned to search for pairs of tracks with a combined invariant consistent with that of the J/ψ meson ($m = 3.01 \pm 0.3\text{GeV}$) or Z boson ($91.2 \pm 5\text{GeV}$), both of which can decay into muon pairs. Tracks must not have been flagged as being part of a J/$\psi \to \mu\mu$ or $Z \to \mu\mu$ pair.

6.2.3. Technology cuts

Tracks passing the event and track selection must have a combined β value from which to calculate particle mass. Each technology is required to pass cuts specific to it for the measured β value to be included in calculating the combined β measurement. β measurements passing these cuts will be called "valid" β measurements.

MDT specific cuts

- More than 10 MDT hits must be present in the track.

- The MDT hits must come from more than one muon spectrometer station.

- The track momentum must not have $\theta = 30° \pm 5, 60° \pm 5$ in order to avoid the issues described in section 5.6.1.

RPC specific cuts

- More than 5 RPC hits must be present in the track.

- The RPC hits must come from more than one muon spectrometer station.

Calorimeter specific cuts

- More than 2 calorimeter hits with deposited energy greater than 250MeV must be present in the track.

6.2.4. β cuts

Prior to applying cuts using the actual β measurement values, all valid β measurements are combined through a weighted average. The weighting of each β is $1/\sigma_{tech}^2$ where σ_{tech} is the width of the β distribution for that technology in the η region the track passes through. The values of σ_{tech} are taken from the distributions used to generate the β PDFs described in section 6.3 and can be found in table 5.1.

β consistency cut

Accepting the combined β requires that more than one technology was used in its calculation and that all technologies used had measured β within $2\sigma_{tech}$ of the combined β. This requirement means that while the calorimeter contributes little to the combined β, due to its low accuracy, it does act as a veto for the other technologies, particularly for the MDT in the endcap and the RPC in the $\theta = 60° \pm 5$ region.

Candidate Cut

A track is considered an SMP candidate if it has a combined β which passes the consistency cut and all valid technology βs are less than a slow particle threshold set at $\beta = 0.95$.

6.3. Background estimation

For this search the background is assumed to be entirely composed of high p_T muons with mismeasured β. The Monte Carlo simulation does not match the β resolution observed in data well enough to accurately predict background and the exact processes producing the muons are unknown. A purely data driven approach is instead taken to estimate the background in this study.

6.3.1. Method

This simulation is done through a set of β probability density functions (PDFs) generated from measured β distributions. The PDFs are generated separately for each technology and split into the regions in η observed to have differing β measurement resolutions. The β distributions in these regions are obtained from tracks passing the event and β cuts as described in section 6.2. The track cuts are, however, modified by reducing the p_T cut to 10GeV and allowing J/$\psi \rightarrow \mu\mu$, Z$\rightarrow\mu\mu$ tracks. The η regions used and the distributions inside the regions are presented in appendix A. The results of Gaussian fits of these distributions are shown in table 5.1 and the percentages below the β thresholds

are shown in table 5.2. PDFs are generated for run periods b-k and l&m separately due to the difference in β resolution between these groups.
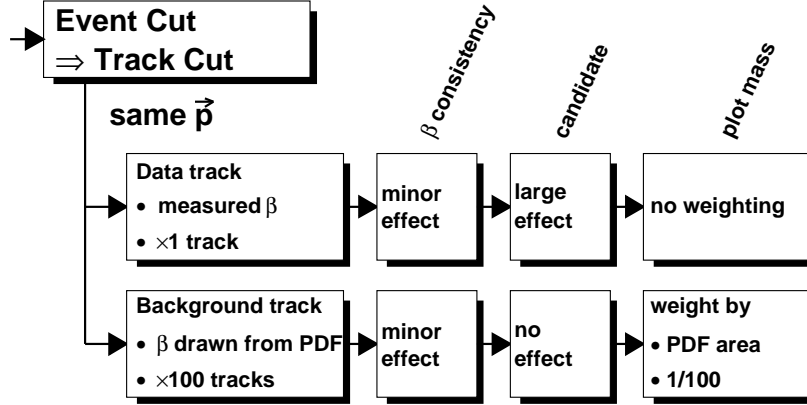

Figure 6.1.: Schematic of the procedure used for background estimation.

The tracks comprising the background estimate are copies of data tracks passing the event and track selection filters during the SMP search (fig. 6.1). For every track passing this level, before applying β cuts, 100 copies of the track are made with the same momentum vector, but with all valid measured β values replaced by random values drawn from the appropriate PDFs. To avoid unnecessary processing, all β values are drawn from the PDFs below the $\beta = 0.95$ threshold. Each β measurement is then weighted by the fraction of its PDF $0 < \beta < 0.95$ represents. The weight of a background track is then

$$weight_{track} = \frac{\prod_{valid\beta} weight_{\beta}}{N_{copies}(100)}. \tag{6.1}$$

The background estimate tracks are treated identically to the measured tracks from this point onwards, other than the reduced weighting when filling histograms. Any which happen not to pass β consistency cuts are discarded.

6.4. Systematic error estimations

Sources of potential systematic error on the signal and background estimates have been identified. The magnitude of the systematic error from these sources depends on the nature of the search. This section describes the sources of systematic error and the way in which it is estimated for the signal and background. Each search result histogram will have the result of these calculations quoted and error bars corresponding to the combined systematic error plotted.

6.4.1. Signal systematic error

The systematic error on the signal is principally due to remaining differences in the β measurement resolution in data and Monte Carlo simulation. In general the Monte Carlo has better β resolution than the data. This leads to better signal acceptance for SMPs with true velocity only slightly lower than the $\beta = 0.95$ threshold and a tighter m_{rec} distribution. The time measurement smearing described in section 5.6.2 largely addresses this problem, but a perfect replication of the resolution observed in data was not attained.

To estimate the worst possible effect this could have on results, the β measurements made in simulation were additionally smeared by a Gaussian with width equal to the corresponding β measurement distribution in data. As the widths are calculated from $\beta = 1.00$ muons, the width is scaled to match the SMP β through:

$$\sigma_{smear} = \sigma_{tech} * \frac{\beta_{rec}}{1.00}. \tag{6.2}$$

The difference in signal acceptance between the data with only time smearing and the data with additional β smearing is calculated for each signal dataset. This smearing necessarily reduces the β measurement accuracy in Monte Carlo to worse than is observed in data. As such, the quoted systematic error is the calculated difference in signal acceptance divided by two.

6.4.2. Background systematic error

The background estimation method makes several assumptions; that each β mismeasurement is random and independent and that the measurement error is constant over the time and detector spaces represented by the PDFs. There is also the implied assumption when generating the PDFs that the background is overwhelmingly larger than the SMP signal when the p_T cut is lowered to 10GeV. Limits set by previous studies justify this last assumption[25]. The assumptions of independence and consistent randomness, however, cause systematic error in the background estimation.

The following sources of systematic error have been identified for the background estimation.

- Statistical limitations of distributions used to make PDFs.

- Correlations in measurement error with η due to shared detector geometry.

- Global shifts in detector timing not accounted for by calibration.

The accuracy of the PDFs used for background estimation is limited by the number of measurements in the distributions from which they were generated. The effect of this statistical limitation was estimated by raising and lowering the distributions by their

statistical certainty. Two sets of PDFs were generated from distributions, one of which had each bin value (n) raised by $\sqrt{n}$, the other lowered by $\sqrt{n}$. The statistical error on background histograms is estimated by taking the average absolute difference between the histograms generated using the modified PDFs and the standard PDF. For a background histogram the quoted systematic error resulting from limited PDF statistics is:

$$e_{PDFstat} = \frac{\sum\limits_{\text{bin}} |n_- - n_0| + |n_+ - n_0|}{2 \sum\limits_{\text{bin}} n_0}, \tag{6.3}$$

where n_0, n_- and n_+ are the bin contents of histograms generated using standard, increased and decreased PDFs respectively.

The β resolution of detectors varies inside each η region. The resolution is related to both the timing resolution and distance from the interaction point, since increased distance leads to increased β measurement resolution. Because of the cylindrical design of ATLAS, track η is strongly related to detector distance from the interaction point. This geometric feature is approximately shared by all detector technologies, slightly invalidating the assumption of random mismeasurement between technologies. The effect of variation of β resolution inside η regions was estimated using two additional sets of PDFs with finer η regions. One set of PDFs was generated by splitting the standard η regions in half, one set was generated by splitting them into quarters. Similar to that resulting from PDF statistics, the quoted systematic error is the average absolute difference between the split histograms and the main histogram.

As outlined in the calibration section, the global timing of ATLAS detectors drifts over time. Shifts taking place over a greater timescale than the run length are accounted for by calibration. Smaller shifts do occur during runs, but are of the order of $0.1 ns$, introducing only minute shifts of order $d\beta \approx 0.002$. The effects of this on result histograms are neglected.

6.5. Search results

Two search channels, one-candidate and two-candidate, are used. In both cases the reconstructed mass of a track is

$$m_{rec} = \frac{p}{\beta \times \gamma}, \tag{6.4}$$

where γ is the Lorentz factor. The β measurement for a track is the combined β value calculated to apply the β consistency cut (see section 6.2.4).

The one-candidate search is a more general search for SMPs and is applicable to other models than GMSB sleptons, but has large amounts of background, even with tight cuts. This background makes it difficult to draw any significant limits on cross

sections from the search results. The results are shown to illustrate background levels and candidate m_{rec} distribution before moving onto the two candidate search. If the β mismeasurement is random, as is assumed, the distributions of these two searches should be closely related.

The two-candidate search is more strongly focussed on pair produced GMSB sleptons and excludes more background, making it possible to draw stronger physical limits from the results. Assuming that the β measurements in each track are independent, requiring two candidates should reduce the background significantly, without heavily impacting signal acceptance.

6.5.1. One candidate search

A simple search for SMPs can be performed by plotting the reconstructed mass of all candidates and counting the number above a threshold. Mass plots from one candidate
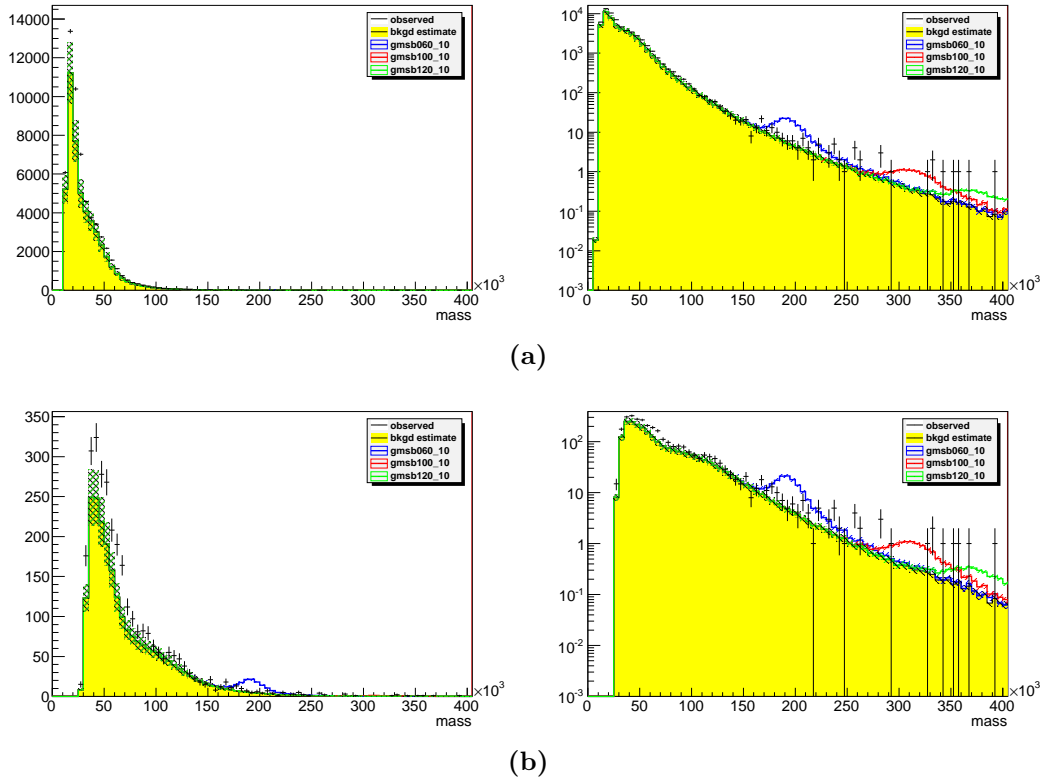
Figure 6.2.: One-candidate search. Linear and logarithmic plots of reconstructed mass from data, background and signal+background tracks passing search criteria with: (a)standard p_T requirements; (b)tightened p_T requirements. The hatching represents the sum of the errors calculated.

searches using the cuts defined in section 6.2 as well as searches with the p_T requirement further tightened to 70GeV are shown in figure 6.2.

The systematic error on the background estimation resulting from PDF statistics was calculated to be 2.0%. The systematic error resulting from the β-η correlation was calculated to be 13.5%. The estimated systematic error on the signal histograms varies from around 3% to 3.5% for all GMSB datasets, an error of 3.5% is therefore used for all datasets.

For our models of interest the expected background in the signal region is typically equal to or greater than the signal. The one candidate search can therefore only impose weak limits on measured cross sections unless combined with more stringent, model specific cuts designed to reduce the muon background. It is possible to use the one-candidate search as an additional channel to complement the two-candidate search, yielding a slight increase in confidence limit setting power. Doing so without introducing systematic effects, however, is not straightforward and will not be attempted in this study.

(a)

(b)

(c)
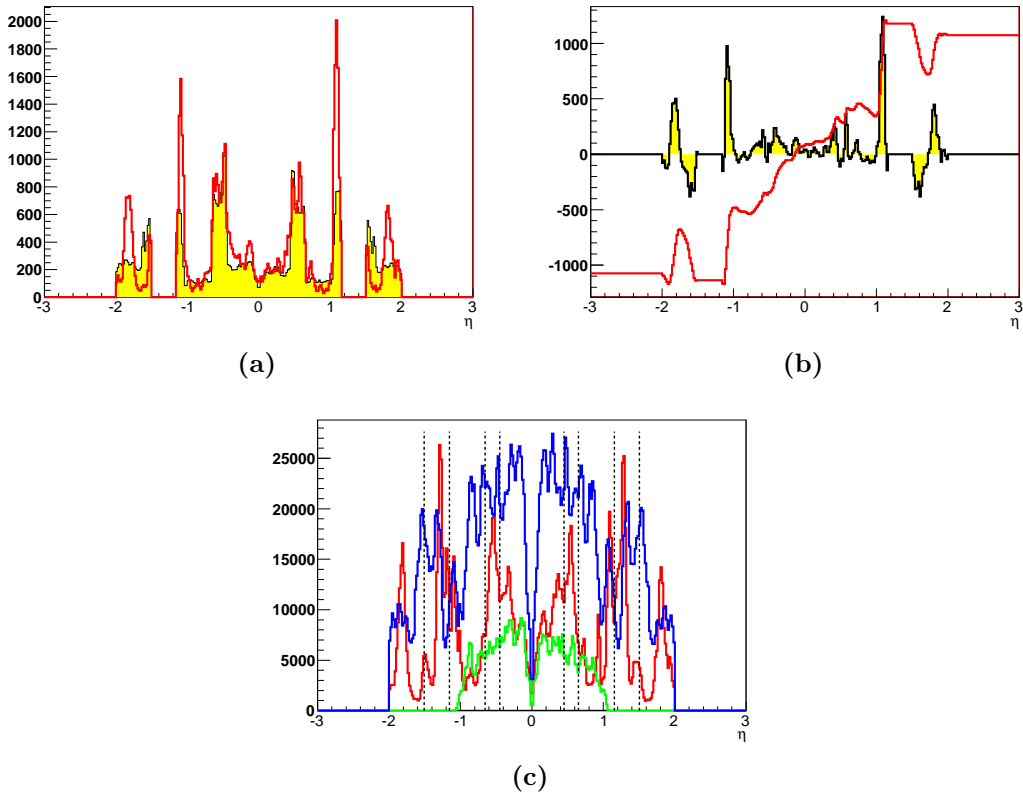
Figure 6.3.: Candidate η distributions. (a) Background (yellow) overlaid with data (red). (b) Data minus background distribution (yellow), cumulative difference overlaid (red). (c) Distribution of $\beta < 0.95$ results from the different technologies; MDT (red), RPC (green) and calorimeter (blue).

Figure 6.3 shows the distribution of candidates in η from data and from the background estimation. The distribution of $\beta < 0.95$ measurements in η for the various technologies is also shown for reference. Candidate distributions for both the data and background show spikes at $|\eta| \approx 1.6$, $|\eta| \approx 1.1$ and $|\eta| \approx 0.5$. The apparent spike at $|\eta| \approx 1.6$ is actually due to the number of tracks being suppressed by the HEC at $\eta > 1.6$, which does not produce measurements that pass technology cuts as reliably as the tile calorimeter. Thus, despite the higher percentage of candidates in the HEC region, the actual number is lower. The spike at the $|\eta|$ transition region is due to the lack of RPC coverage and, in data, the lower β measurement accuracy in the transition region between the endcap and the barrel. Over half of the data candidate excess over background originates from the shared decrease in resolution of the MDT and calorimeter in this region. The spike at $|\eta| \approx 0.5$ is simply due to the lack of usable MDT coverage.

Overall, the background is slightly underestimated, particularly at low m_{rec}. However, the shape of the distribution at higher m_{rec} is well reproduced. For the two candidate search, the accuracy of the distribution at higher m_{rec} is of primary importance.

6.5.2. Two-candidate search

This search requires exactly two SMP candidates in an event and takes the m_{rec} of the candidate with lower m_{rec}. The candidacy of a track is determined using the cuts defined in section 6.2; no additional tightening of cuts is applied to the tracks. For the background estimation, every event with more than 1 track passing the basic track selection cuts uses each possible track pairing once, weighting the pair by

$$w_{ij} = w_i w_j \prod_{k=0, \neq i, \neq j}^{n} (1 - w_k) \qquad (6.5)$$

where $w_{i,j,k}$ is the track weight determined by the PDF β weighting.
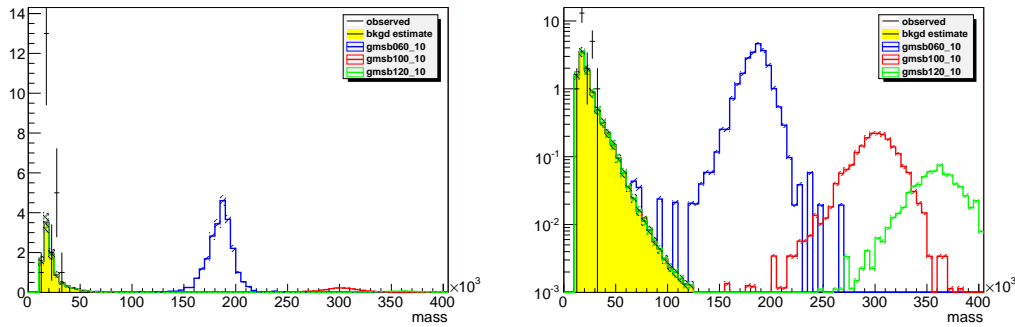

Figure 6.4.: Two-candidate search. Linear and logarithmic plots of reconstructed mass of lower mass track from data, background and signal+background pairs passing search criteria. The hatching represents the sum of the errors calculated.

Cut Level	1 track	squared	2 tracks
Basic	5410743	100%	107346
Consistency	85.0%	72.2%	73.6%
Candidate	1.05%	0.011%	0.033%

(a) Data, observed values

Cut Level	1 track	squared	2 tracks
Basic	5410743	100%	107346
Consistency	84.7%	71.8%	72.8%
Candidate	0.862%	0.00743%	0.0121%

(b) Data, expected background

Table 6.1.: Rates at which the one and two candidate cuts are passed by data and background. "Basic" requires that the tracks have passed the standard track selection and have at least one valid β measurement. "Consistency" requires that the tracks pass the β consistency cut. "Candidate" requires that the tracks pass the candidate cut. The 1 track column shows results for events with exactly 1 "Basic" track, squared shows the square of the 1 track column values, 2 tracks shows results from events with exactly 2 "Basic" tracks.

(a) $\tan \beta = 5$ (b) $\tan \beta = 10$ (c) $\tan \beta = 30$
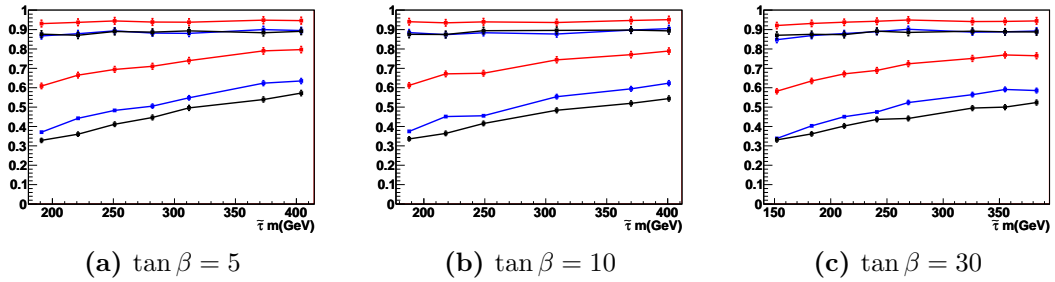
Figure 6.5.: Fractional acceptance of SMPs models analysed using the same method as in table 6.1. The one-candidate search us shown in red, its square in blue and the two-candidate search in black. The upper line represents the "Consistency" fraction, the lower line "Candidate" fraction.

An additional ΔR cut is applied, requiring the momentum of the candidates to be separated by $\Delta R > 0.2$, to avoid contamination by muons travelling through the same MDT chamber, potentially invalidating the assumption of random mismeasurement between tracks. This additional cut reduces acceptance of slepton pairs by approximately 0.1%. The high invariant mass of processes creating sleptons means that their separation is typically much larger.

The systematic error on the background estimation resulting from PDF statistics was calculated to be 3.0%. The systematic error resulting from the β-η correlation was calculated to be 13.5%. The estimated systematic error on the signal histograms varies from around 6% to 7.5% for all GMSB datasets, an error of 7% is used for all datasets.

Figure 6.4 shows the results of the two candidate search. Comparing with figure 6.2 it is clear that the two candidate requirement dramatically reduces background over single candidates. The excess at low m_{rec} is more pronounced in the two candidate search than in the one candidate, but the m_{rec} is still lower than any mass threshold that would be set. The estimation of near zero background over the rest of the mass axis is expected to be accurate as no excess was observed elsewhere during the one candidate search.

The two candidate requirement also reduces signal acceptance, but to a much lesser extent. Table 6.1 shows the background, signal and data rates of the one and two candidate searches. The two candidate search background agrees approximately with $\frac{B_{2candidate}}{N_{2track}} \approx (\frac{B_{1candidate}}{N_{1track}})^2$ with some underestimation of the background, as expected.

6.6. Confidence limit calculation

Confidence limits are used to define the certainty to which a result is confirmed. Typically, exclusion limits are quoted at the 95% confidence level. Here the 95% confidence upper limit on cross sections for GMSB models producing pairs of long lived sleptons is calculated. This section describes how the confidence levels for an arbitrary result can be calculated using the modified frequentist (CL_s) method[17].

The confidence limit of exclusion is $CL_{exclusion} = 1 - CL_{observed}$. For a 95% exclusion confidence a signal confidence level of < 0.05 is required.

6.6.1. The CL_s method

The CL_s confidence level is defined as

$$CL_s \equiv \frac{CL_{sb}}{CL_b}, \tag{6.6}$$

where CL_{sb} and CL_b are the respective confidence levels on the signal plus background and background only hypotheses. These confidence levels can be expressed as integrals of the probability function P over the area of the likelihood ratio Q covered by the observed value,

$$\frac{CL_{sb}}{CL_b} = \frac{\int_{-\infty}^{Q_{obs}} \frac{\mathrm{d}P_{sb}(Q)}{\mathrm{d}Q}\mathrm{d}Q}{\int_{-\infty}^{Q_{obs}} \frac{\mathrm{d}P_b(Q)}{\mathrm{d}Q}\mathrm{d}Q}. \tag{6.7}$$

If we define s_i and $S_i(x)$ as the expected amount of signal and corresponding probability distribution function in channel i, similarly b_i and $B_i(x)$ for the background and d_i as the number of candidates observed in data, then the likelihood ratio is formally

$$Q = \frac{\prod_{i=1}^{N_{chan}} \frac{e^{-(s_i+b_i)}(s_i+b_i)^{d_i}}{d_i!} \prod_{j=1}^{d_i} \frac{s_i S_i(x_{ij})+b_i B_i(x_{ij})}{s_i+b_i}}{\prod_{i=1}^{N_{chan}} \frac{e^{-(b_i)}(b_i)^{d_i}}{d_i!} \prod_{j=1}^{d_i} \frac{b_i B_i(x_{ij})}{b_i}}, \tag{6.8}$$

where x_{ij} is the discriminating value for channel i of the candidate indexed by j.

6.6.2. CL_s method for counting experiments

In the case of counting experiments, the S_i and B_i distributions are assumed to be the same, so the $\prod_{j=1}^{d_i}$ sections of equation 6.8 can be eliminated. Additionally since we are no longer integrating over a continuous spectrum for Q but over discrete possible observed values of d, equation 6.7 is altered to the form

$$CL_s = \frac{CL_{sb}}{CL_b} = \frac{\sum_{n=0}^{d} P_{sb}(n)}{\sum_{n=0}^{d} P_b(n)}.$$ (6.9)

The $P_{sb}()$ and $P_s()$ functions are now assumed to be Poissonian probability distributions, giving

$$CL_s = \frac{\sum_{n=0}^{d} \frac{e^{-(s+b)}(s+b)^n}{n!}}{\sum_{n=0}^{d} \frac{e^{-(b)}(b)^n}{n!}}$$ (6.10)

An identical result can be obtained by computing the Bayesian credible interval for a similar experiment.

6.7. Cross sections

Using the obtained search results and the established method of computing confidence levels, the 95% confidence limits on cross sections excluded by this search can now be calculated. This section describes how the computation of upper limits on cross sections is performed and compares the limits obtained with theory and the results of other groups.

6.7.1. Calculation method

The limits are set through a counting experiment on the mass axis of the two candidate search results histogram (fig. 6.4) using the CL_s method of computing confidence levels.

The computing procedure first takes the two candidate mass histograms from observed data, expected background and one of the signal models with the aim of finding the lowest factor by which the signal histogram can been scaled and still have and observed $CL_s < 0.05$ on the signal from the data. The number of data, signal and expected background events is found by integrating the histograms above a mass cut. The value of this mass cut is optimized for each model by first scanning over the mass axis and finding the cut that gives the lowest expected scale factor. The expected scale factor can be calculated by using the expected background value in place of the actual number of observed events.

To find the scale factor for which $CL_s = 0.05$, the number of signal events is scaled over a series of iterations, increasing the scaling in the next iteration if $CL_s > 0.05$ or decreasing it if $CL_s < 0.05$ until the CL_s is within 10^{-5} of 0.05. During these iterations, the effect of error is simulated by repeating the measurement 10^6 times, each time altering the value for expected signal and background with random values from a set of Gaussians, each estimating a source of error. The final CL_s value is the average of the results from these repetitions.

The scaling factor (f_{scale}) can be thought of as

$$f_{scale} = \frac{n_{CL_s}}{\epsilon \times A \times n_{MCevents}} \tag{6.11}$$

where n_{CL_s} is the number of candidates required for $CL_s = 0.05$, ϵ is the trigger/reconstruction efficiency and A the geometric acceptance of the detector, although these quantities are never calculated individually. Altering f_{scale} effectively simulates different numbers of signal events on a continuous scale.

The minimum cross section excluded at 95% for that model is then

$$\sigma = \frac{f_{scale,min} \times n_{MCevents}}{\mathcal{L}} \tag{6.12}$$

where $\mathcal{L}$ is the integrated luminosity (4.06fb^{-1}).

6.7.2. Results

Cross section limits were obtained for each of the signal models, the results are shown in table 6.2

The models with $\Lambda \leq 90$ are excluded by this search, which excludes $\widetilde{\tau}$ masses below 250GeV for the range of $\tan\beta$ used. A more detailed analysis of the parameter space excluded by the search is made in the next section.

6.8. Comparison with other studies

The SMP analysis group at CERN performed their own study searching for SMPs in data collected at ATLAS in 2011[26]. This section compares the results of the slepton search of this study with those of the study performed by the SMP group.

Figure 6.6 shows the cross sections excluded by this study and by the SMP group along with those predicted at NLL+NLO. Long lived $\widetilde{\tau}$ lighter than 260GeV can be excluded up to $\tan\beta = 30$, those lighter than 285GeV can be excluded for $\tan\beta < 10$.

Figure 6.7 shows the Λ, $\tan\beta$ parameter space excluded by this study and the SMP group.

This study sets weaker limits on $\widetilde{\tau}$ production than the study performed by the SMP group, but the difference is not large. One simple reason for the lower limits obtained is the lower luminosity that could be utilized. Reduced availability of $Z\rightarrow\mu\mu$ datasets meant that around 0.5fb^{-1} of potentially usable muon data was lost due to lack of any run calibration. The SMP group method also utilizes a one candidate channel in addition to the two candidate channel to further improve the limit setting power. Other potential factors include optimization of cuts and a potential difference in simulated signal acceptance from the reconstruction algorithm.

The principle advantage of MuonBetaRefit is its usage of standard ATLAS reconstruction algorithms with only minor modification. The SMP group by comparison uses

Λ	$\tan\beta$	$m_{\widetilde{\tau}}$	$\epsilon \times A(\%)$	m_{cut}	σ_{95CLs}	σ_{theory}
50	5	161	10.7	90	7.03	
50	10	158	10.1	90	7.34	
50	30	122	9.3	75	8.08	
60	5	191	12.4	110	6.06	43.8
60	10	188	12.0	90	6.24	47.7
60	30	152	11.6	100	6.48	61.8
70	5	221	14.1	105	5.33	18.4
70	10	218	13.6	100	5.51	20.0
70	30	183	13.5	105	5.54	26.4
80	5	251	16.1	100	4.65	8.65
80	10	249	15.7	110	4.77	9.55
80	30	212	15.2	105	4.93	
90	5	282	17.1	120	4.38	4.47
90	30	241	16.2	105	4.62	6.80
100	5	312	18.9	150	3.96	2.48
100	10	309	18.4	120	4.08	2.80
100	30	269	16.7	125	4.49	3.84
120	5	373	20.0	100	3.75	0.86
120	10	370	19.5	130	3.85	0.92
120	30	326	20.1	160	3.74	
130	5	404	20.1	115	3.60	0.53
130	10	401	20.5	210	3.66	0.63
130	30	355	20.9	185	3.59	0.89
140	30	383	21.3	150	3.51	0.58
150	5	465	21.3	195	3.52	
150	10	462	20.9	125	3.59	
150	30	411	23.5	145	3.20	

Table 6.2.: Cross sections excluded at 95% CL for all GMSB models used, masses are in GeV, ϵ is efficiency, A is signal acceptance. Expected cross sections were also calculated but were in almost all cases identical to the observed cross sections at 3 significant figures.

(a) $\tan\beta = 5$ **(b)** $\tan\beta = 10$ **(c)** $\tan\beta = 30$
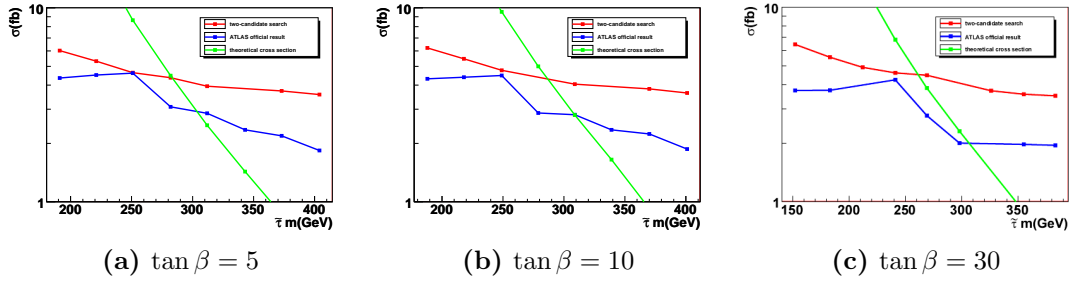
Figure 6.6.: Cross sections excluded by this study (red) and the SMP group (blue), along with theoretical cross sections calculated at NLL+NLO (green), plotted against $\tilde{\tau}$ masses for a fixed value of $\tan\beta$
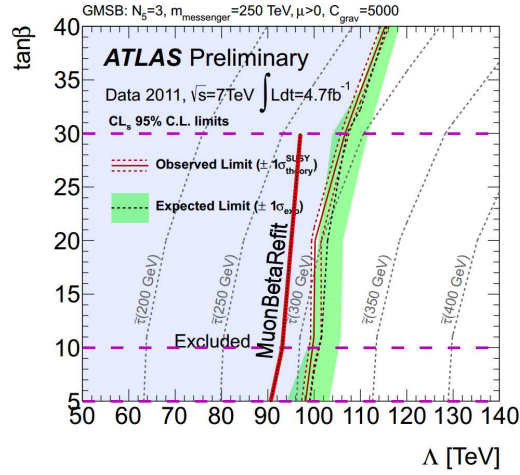

Figure 6.7.: Excluded parameter space from SMP group with the result obtained from MuonBetaRefit overlaid in red. $\tan\beta$ planes detailed in figure 6.6 are also highlighted

entirely purpose built software, generally not understood by the ATLAS community at large.

Chapter 7.

Summary

Charged long-lived stable massive particles (SMPs) are predicted to exist by several theorised extensions to the Standard Model of particle physics. These particles, if produced at the LHC, would be expected to behave as heavy "muon-like" tracks and would be detectable as such in the ATLAS muon spectrometer. MuonBetaRefit reconstructs and flags these tracks using slightly modified versions of the ATLAS muon spectrometer reconstruction algorithms rather than a purpose built set of algorithms.

An assumed time of flight is necessary to reconstruct track segments in the muon spectrometer's MDT detectors; in standard reconstruction this corresponds to an assumed velocity of $\beta = 1$. This leads to SMP tracks of particles travelling at $\beta < 1$ being misreconstructed. The MuonBetaRefit package was developed to perform track reconstruction without a predefined β assumption, allowing more accurate reconstruction of SMP tracks. Finding the best fitting β assumption leads to a measurement of track velocity from the MDTs. Additional velocity measurements were also able to be made using time of flight information from the muon spectrometer's RPC detectors and the calorimeter technologies.

The velocity measurements made by MuonBetaRefit are sensitive to the timing accuracy of the detector elements. Calibration of the detector beyond the ATLAS standard was performed to maximize β measurement accuracy. This calibration was performed in two stages, an element-calibration to calibrate each detector element to a single standard for the technology and a phase-shift calibration to calibrate each standard to the LHC clock.

To test the performance of the MuonBetaRefit package, an SMP search was conducted in the framework of setting a lower limit on the mass of long lived GMSB $\widetilde{\tau}$ particles. This search was performed using data collected at ATLAS throughout 2011. SMP candidates were identified by selecting tracks refitted by MuonBetaRefit with momentum $p_T > 30\text{GeV}$ and $|\eta| < 2.0$ and all reliable β measurements consistent with each other and lower than a threshold of $\beta = 0.95$. An estimate of the background present from muons with mismeasured velocity was obtained through a data driven approach. By searching for pairs of SMP candidates, background from muon tracks was suppressed enough to draw cross section limits.

The calculated cross section limits exclude long lived GMSB $\widetilde{\tau}$s with mass lower than 260GeV in the parameter space region $\tan\beta < 30$. $\widetilde{\tau}$ lighter than 285GeV can also be excluded for $\tan\beta < 10$. These exclusion limits are of similar strength to those set by the ATLAS SMP group using 2011 data.

In conclusion, the MuonBetaRefit package uses proven ATLAS muon reconstruction algorithms to identify SMP tracks in the ATLAS muon spectrometer by measuring velocity. Its performance has been shown to be sufficient for charged SMP searches, such as for the GMSB $\widetilde{\tau}$. MuonBetaRefit has the advantage over bespoke analysis algorithms of being based on software widely used and understood in the ATLAS community.

Appendix A.

Variation of β with η

The β and hit t_0 distributions across the η regions of the detector separated for analysis are presented. The aim is to show the difference in resolution between the established η regions and the variation present across those regions.

Overall histograms showing β and t_0 against η, highlighting the different η regions used, will be presented for each technology. This is followed by histograms of distributions for each η region of each technology. The overall β and t_0 distributions of each η region are overlaid with the distributions of each quarter of the region. Since the A and C sides of the detector share similar geometry, the distributions from opposing η regions will be merged into regions of $|\eta|$. All one-dimensional histograms have their integrals normalized to one for straightforward comparison.

The same dataset used in chapter 6, corresponding to data accumulation throughout 2011, is used.
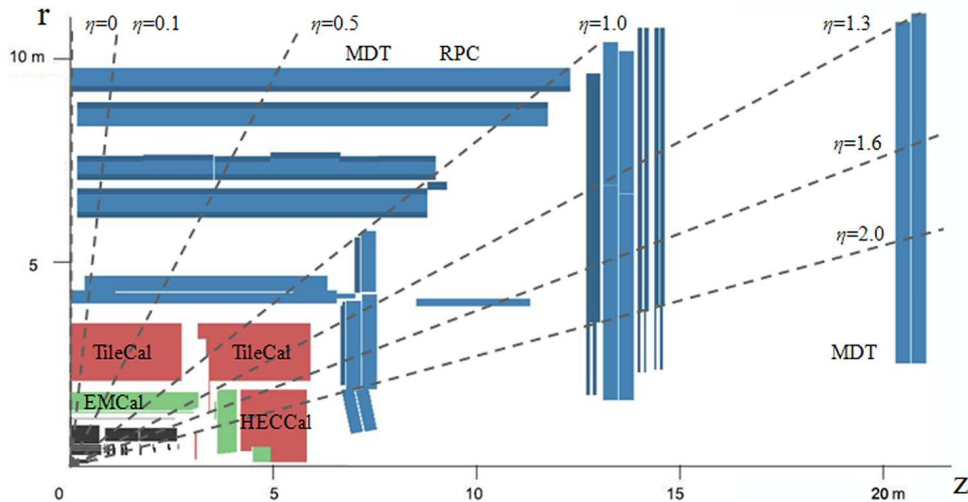
Figure A.1.: Profile of ATLAS detector in rz-plane with η lines used to divide detector regions drawn

Figure A.1 shows the lines in η which divide the regions used. The lines used are different for each detector technology. The following sections explain the reasoning behind the divisions used for each technology.

A.1. MDT

The MDT is split into seven η regions. The regions are largely dictated by the pairs of regions at $30° \pm 5$ and $60° \pm 5$ where no accurate β measurements can be drawn. An additional region describing the area where the two sides of the barrel join, and detector coverage is minimal, is also established. The η boundaries of these regions are $-0.10 < \eta < 0.10 < |\eta| < 0.50 < |\eta| < 1.3 < |\eta| < 2.00$ and are shown in figure A.2.

Measurements in $30° \pm 5$ and $60° \pm 5$ regions are always excluded from analysis, unless explicitly plotted against η. The η regions on either side are, however, defined as joining at $\eta = \pm 1.3$ and $\eta = \pm 0.5$ for simplicity. To avoid needless histograms of distributions from unused regions, the histograms for the MDT start and end at the boundaries of the excluded regions.

A.2. RPC

The RPC is split into five η regions. The β measurement resolution varies continuously with η as the distance from the interaction point changes. The two main pairs of η regions represent two higher $|\eta|$ regions where the distance is highly dependent on η and two lower $|\eta|$ regions where it is less dependent. There is also the central barrel η region where there is low coverage. The η boundaries of these regions are $0.10 < \eta < 0.10 < |\eta| < 0.50 < |\eta| < 1.2$ are shown in figure A.7.

A.3. Calorimeter

The calorimeter is split into seven η regions. The regions correspond to a pair of regions at high $|\eta|$, mainly covered by the HEC calorimeter and two pairs of regions covered by the barrel and extended barrel regions of the tile calorimeter at lower and higher $|\eta|$ respectively. All regions are additionally covered by the EM calorimeter. The calorimeter also has a central barrel η region with low coverage. The η boundaries of these regions are $0.10 < \eta < 0.10 < |\eta| < 1.00 < |\eta| < 1.6 < |\eta| < 2.00$ are shown in figure A.11.

(a)

(b)
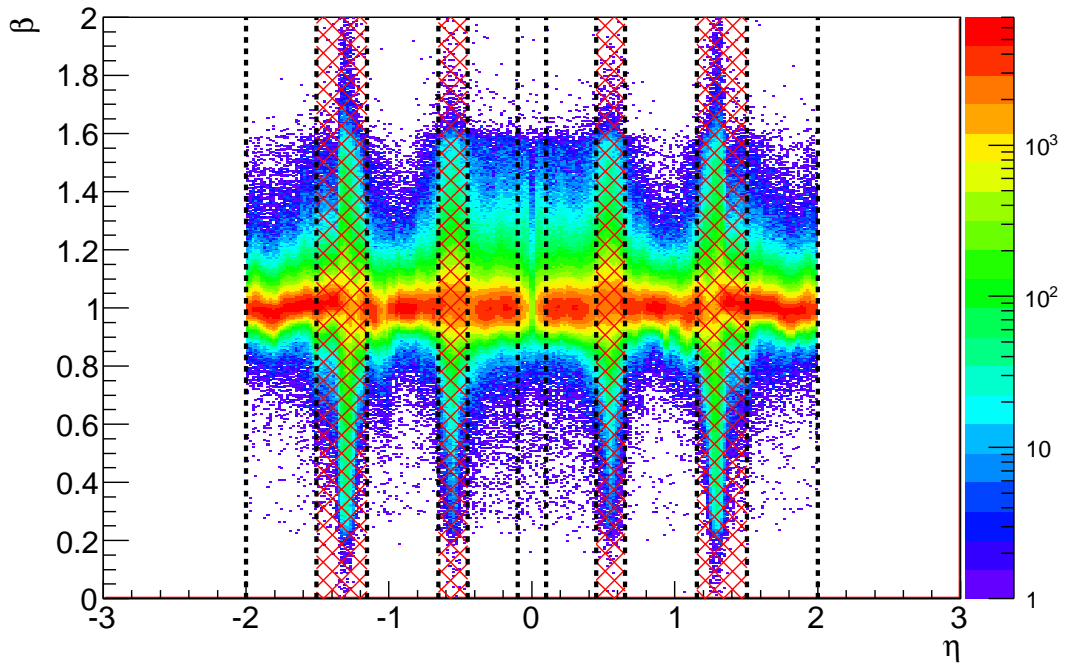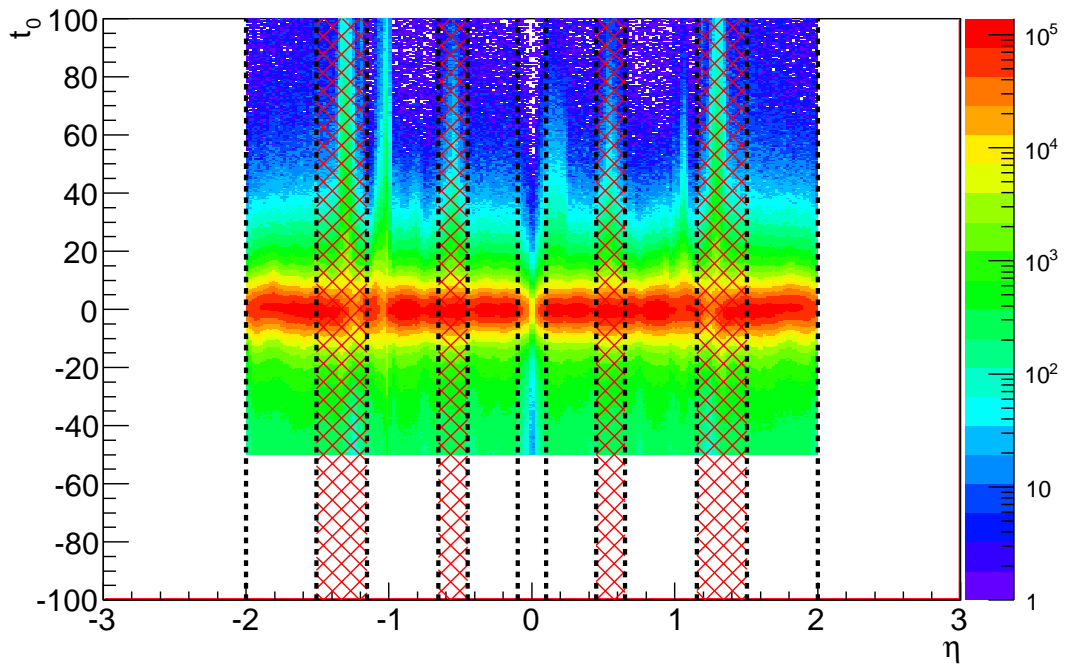
Figure A.2.: MDT (a)β (b)t_0 vs η showing η regions. Regions excluded from analysis are hatched in red.
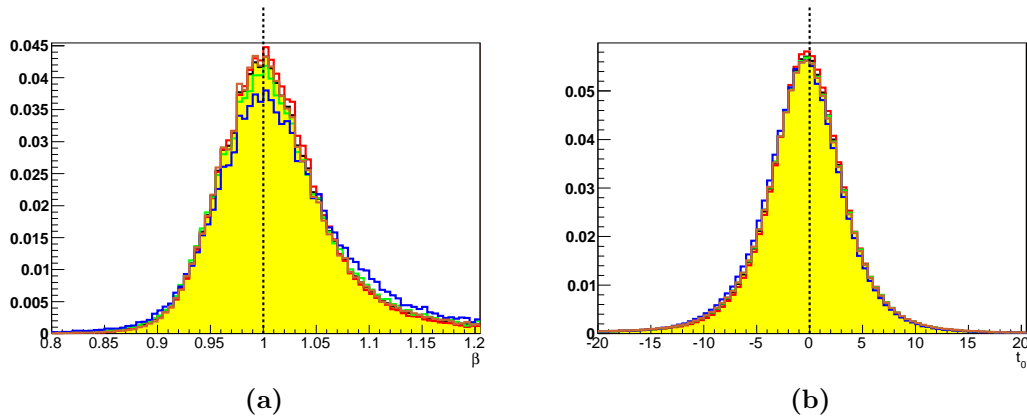
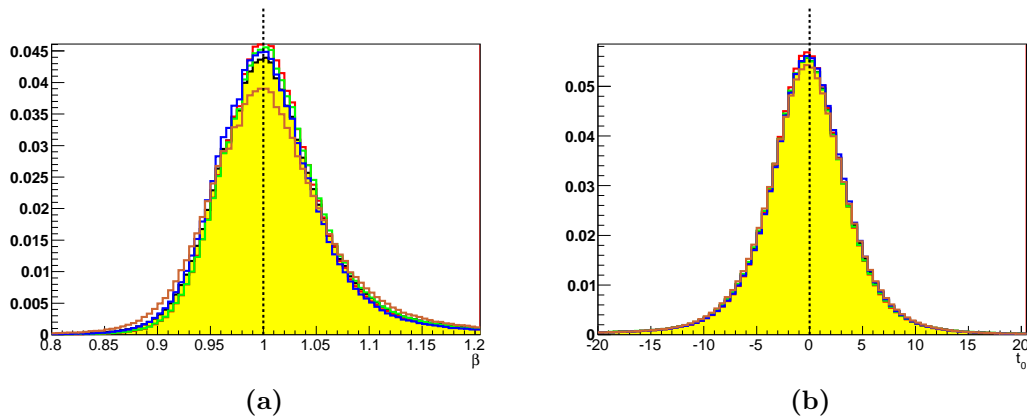**Figure A.3.:** MDT (a)β (b)t_0 in $-0.10 < \eta < 0.10$ region (yellow). Overlaid lines are sub-distributions for $-0.10 <$ η $< -0.05 <$ $\eta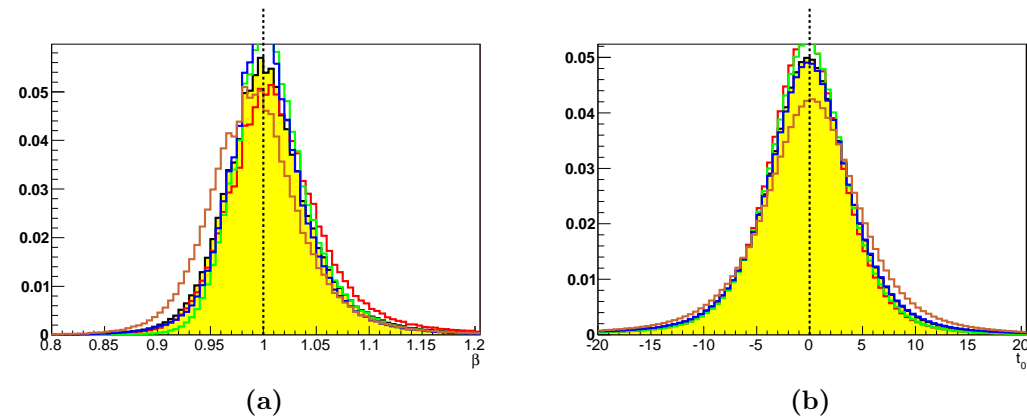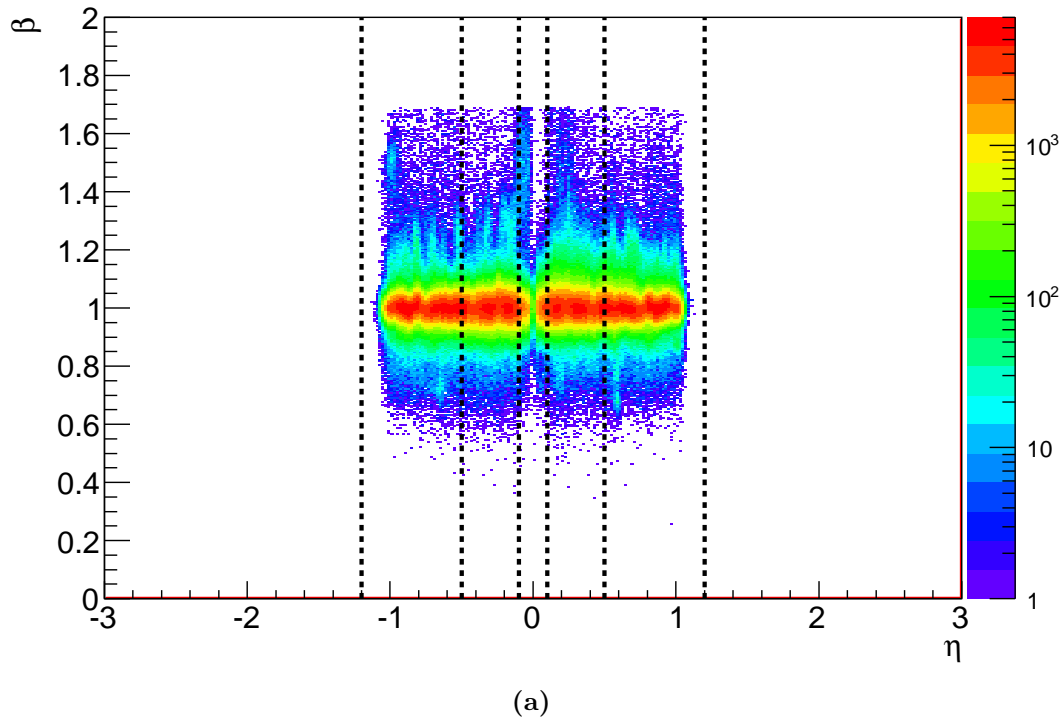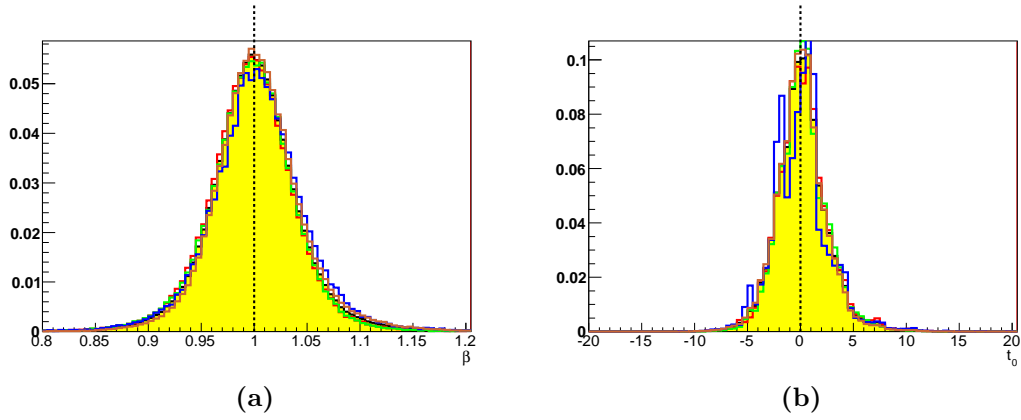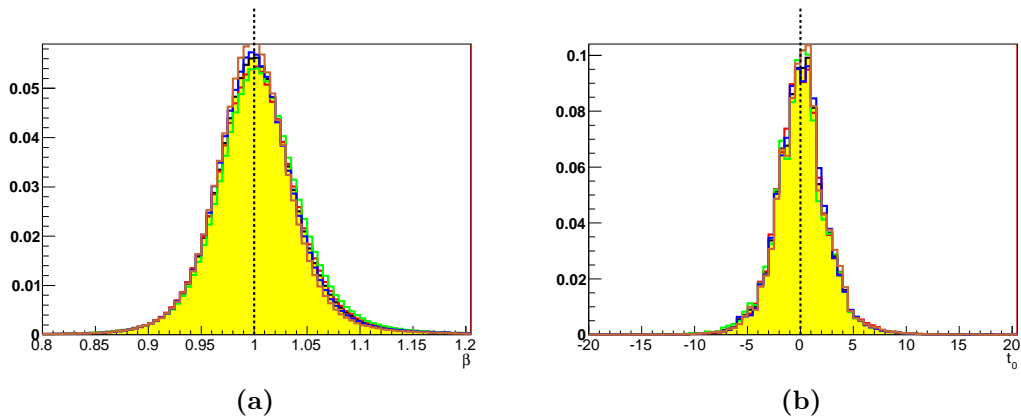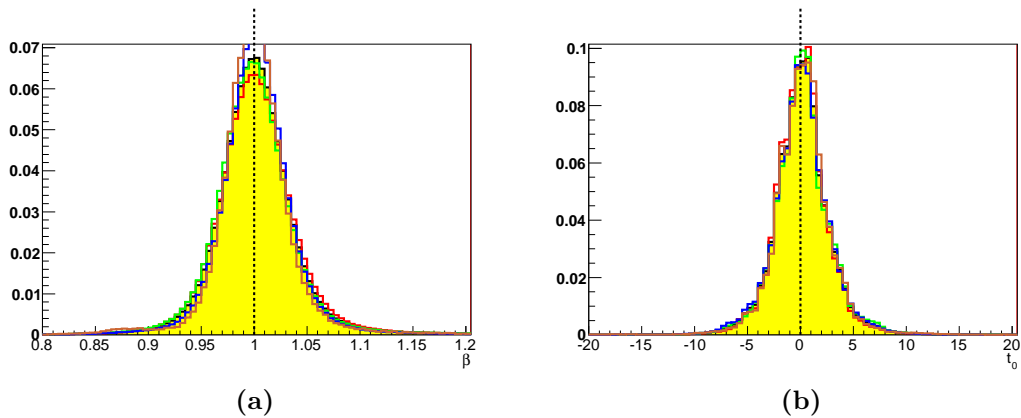$ $< 0.00 <$ η $< 0.05 <$ η < 0.10.

Figure A.4.: MDT (a)β (b)t_0 in $0.10 < |\eta| < 0.45$ region (yellow). Overlaid lines are sub-distributions for $0.10 <$ $|\eta|$ $< 0.19 <$ $|\eta|$ $< 0.28 <$ $|\eta|$ $< 0.36 <$ $|\eta|$ < 0.45.

Figure A.5.: MDT (a)β (b)t_0 in $0.65 < |\eta| < 1.15$ region (yellow). Overlaid lines are sub-distributions for $0.65 <$ $|\eta|$ $< 0.78 <$ <span style="color:or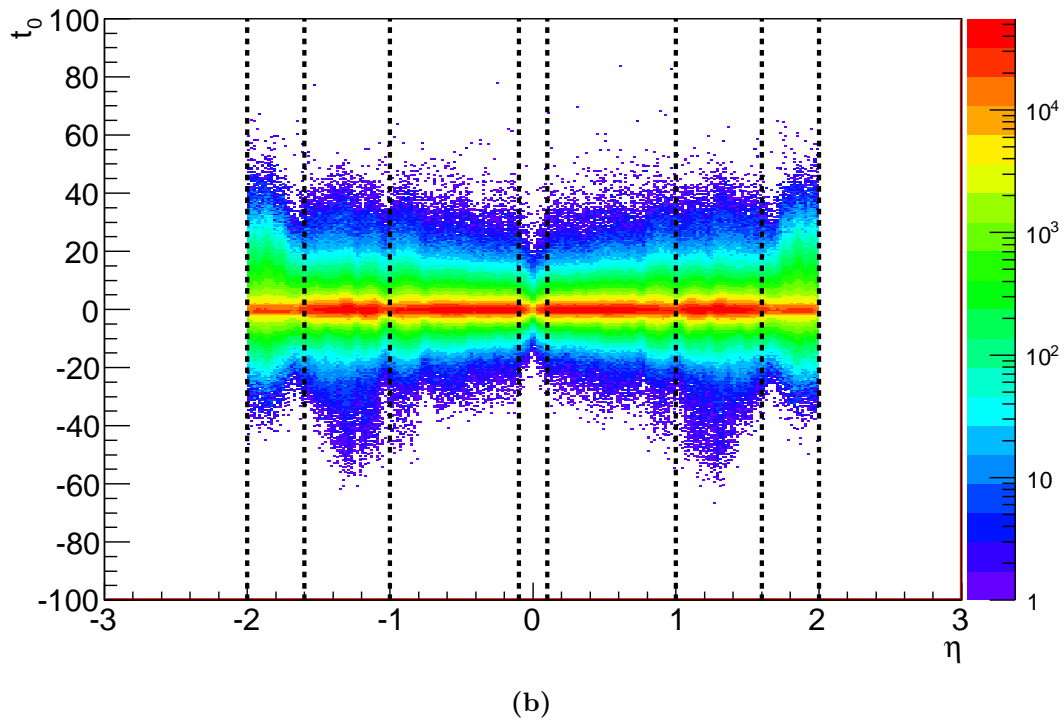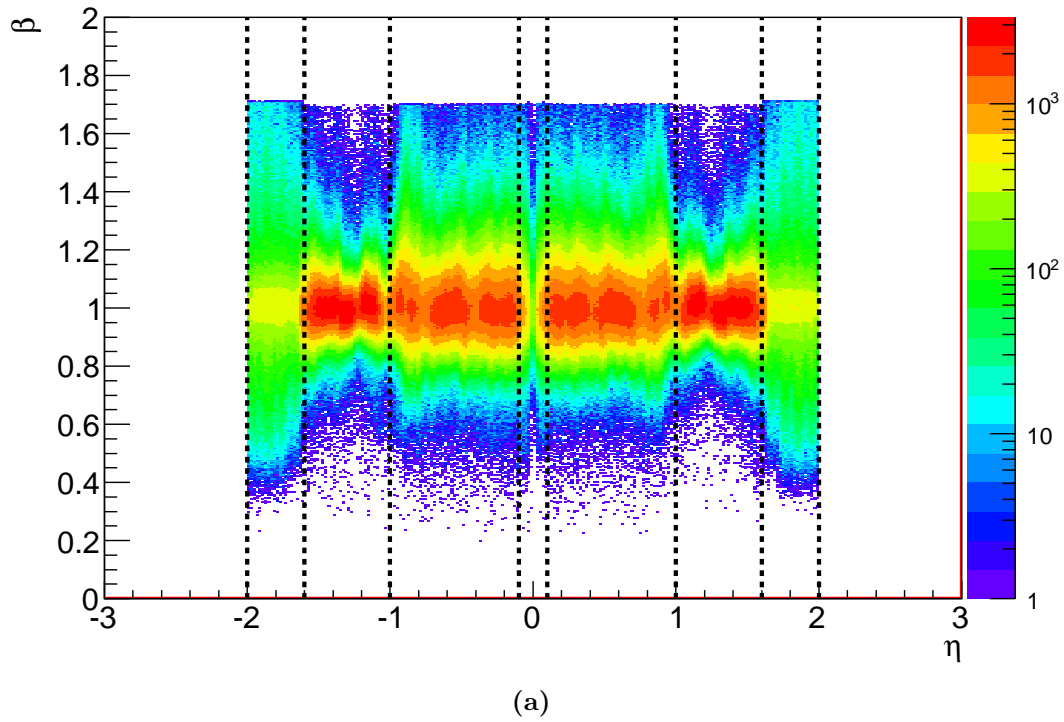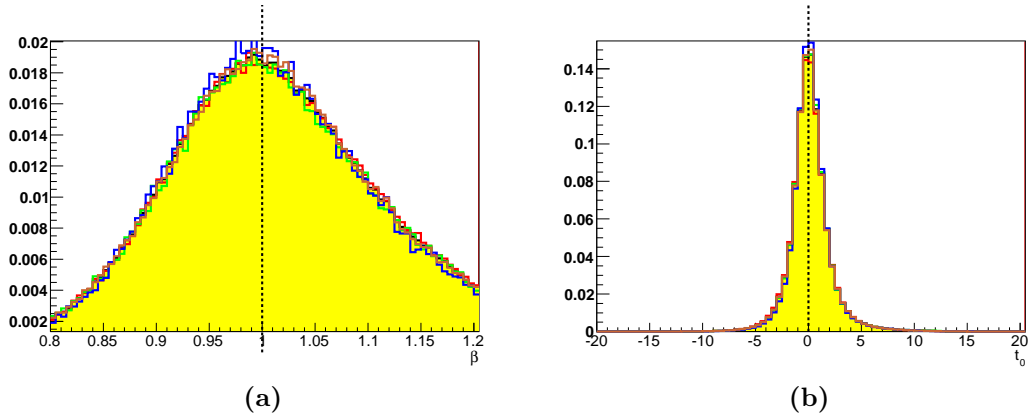ange">$|\eta|$ $< 0.90 <$ $|\eta|$ $< 1.03 <$ $|\eta|$ < 1.15.

(a)   (b)
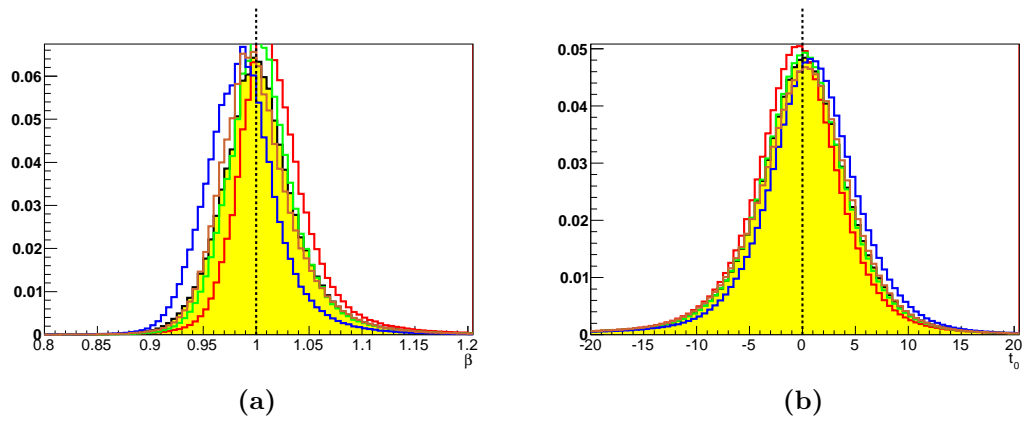
Figure A.6.: MDT (a)β (b)t_0 in $1.51 < |\eta| < 2.00$ region (yellow). Overlaid lines are sub-distributions for $1.51 < |\eta| < 1.63 < |\eta| < 1.75 < |\eta| < 1.88 < |\eta| < 2.00$.

(a)

(b)
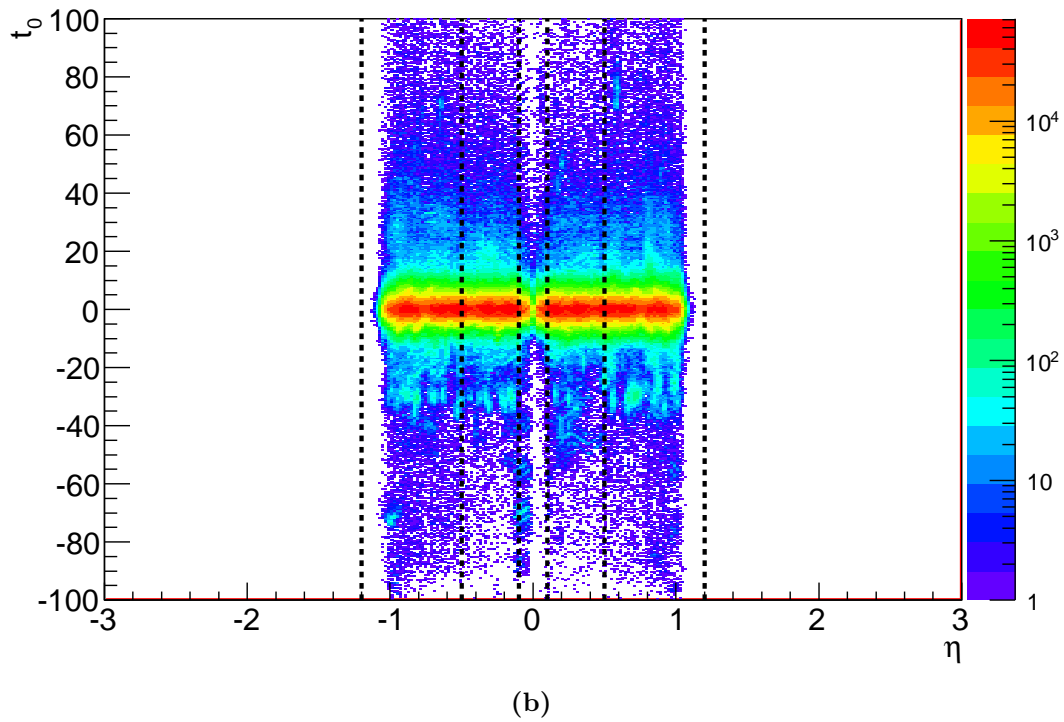
**Figure A.7.:** RPC (a)β (b)t_0 vs η showing η regions.

Figure A.8.: RPC (a)β (b)t_0 in $-0.10 < \eta < 0.10$ region (yellow). Overlaid lines are sub-distributions for $-0.10 <$ η $< -0.05 <$ η $< 0.00 <$ η $< 0.05 <$ η < 0.10.

Figure A.9.: RPC (a)β (b)t_0 in $0.10 < |\eta| < 0.50$ region (yellow). Overlaid lines are sub-distributions for $0.1 <$ $|\eta|$ $< 0.2 <$ $|\eta|$ $< 0.3 <$ $|\eta|$ $< 0.4 <$ $|\eta|$ < 0.5.

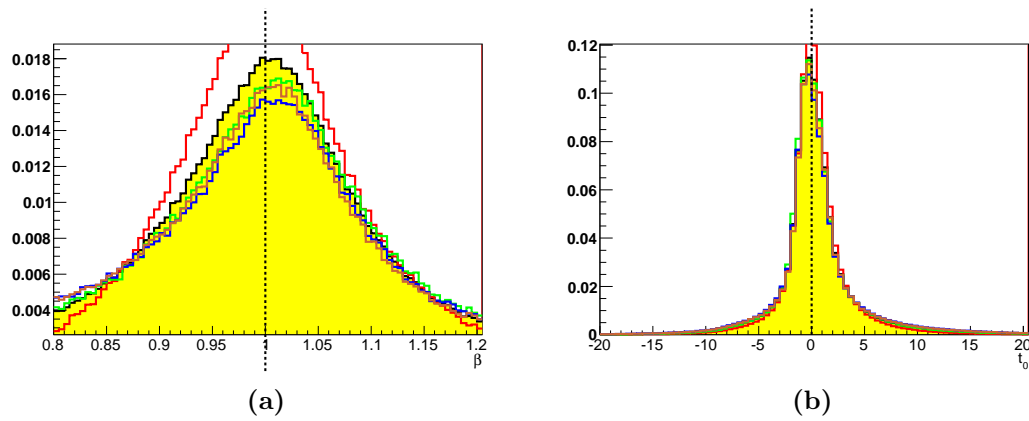**Figure A.10.:** RPC (a)β (b)t_0 in $0.50 < |\eta| < 1.20$ region (yellow). Overlaid lines are sub-distributions for $0.5 <$ $|\eta|$ $< 0.68 <$ $|\eta|$ $< 0.85 <$ $|\eta|$ $< 1.03 <$ $|\eta|$ < 1.20.

(a)

(b)

Figure A.11.: Calorimeter (a)β (b)t_0 vs η showing η regions.

Figure A.12.: Calorimeter (a)β (b)t_0 in $-0.10 < \eta < 0.10$ region (yellow). Overlaid lines are sub-distributions for $-0.10 < \eta < -0.05 < \eta < 0.00 < \eta < 0.05 < \eta < 0.10$.
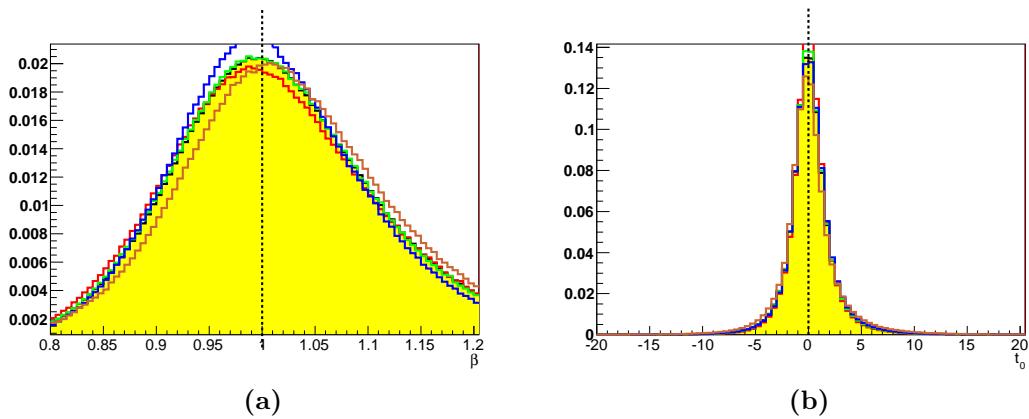
Figure A.13.: Calorimeter (a)β (b)t_0 in $0.10 < |\eta| < 1.00$ region (yellow). Overlaid lines are sub-distributions for $0.10 < |\eta| < 0.33 < |\eta| < 0.55 < |\eta| < 0.78 < |\eta| < 1.00$.
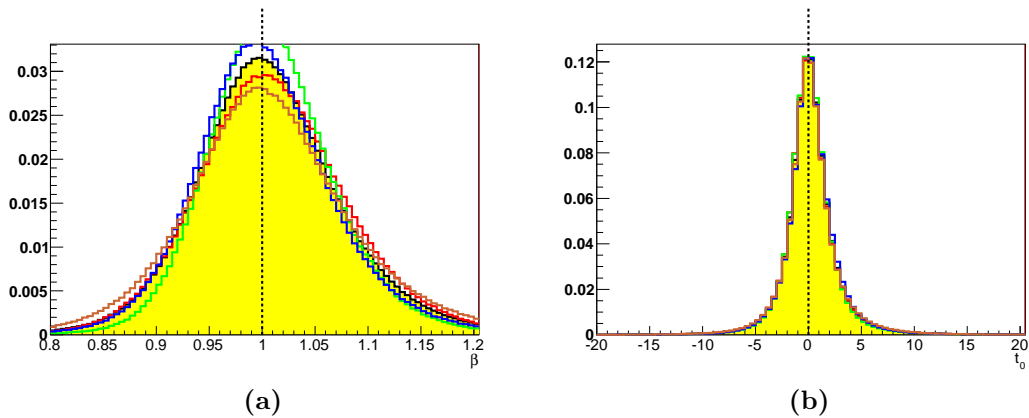
Figure A.14.: Calorimeter (a)β (b)t_0 in $1.00 < |\eta| < 1.60$ region (yellow). Overlaid lines are sub-distributions for $1.00 < |\eta| < 1.15 < |\eta| < 1.30 < |\eta| < 1.45 < |\eta| < 1.60$.

(a)   (b)

Figure A.15.: Calorimeter (a)β (b)t_0 in $1.60 < |\eta| < 2.00$ region (yellow). Overlaid lines are sub-distributions for $1.60 < |\eta| < 1.70 < |\eta| < 1.80 < |\eta| < 1.90 < |\eta| < 2.00$.

Appendix B.

Calibration

The effects of the element calibration, phase shift calibration and β shift calibration steps on β and t_0 are presented. To avoid bias, the histograms have been generated using a dataset obtained with the E_T^{miss} trigger. The calibration databases were obtained using single muon triggers.

To obtain uncalibrated results requires processing in ATHENA, which is highly CPU intensive. A relatively small dataset is used to keep processing time manageable. The specific dataset used is:

- data11_7TeV.periodJ.physics_JetTauEtMiss.PhysCont.DESDM_RPVLL.pro10_v01.

The calorimeter timing is slightly biased towards late hit times for E_T^{miss} triggered events compared to the single muon triggered events used for calibration. This leads to a bias towards low β for calibrated measurements in the calorimeter. This is described further in section 5.5.4.

The calibration results are presented for each detector region in $|\eta|$. The η ranges used and their determination are described in chapter A.
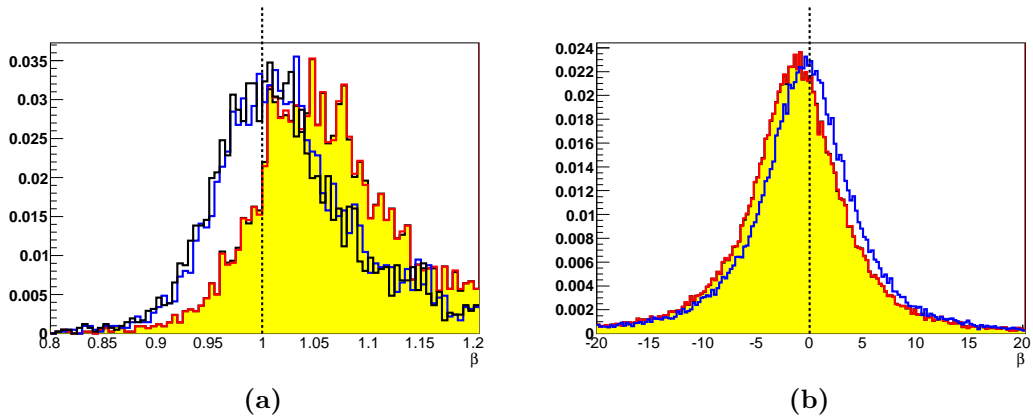
(a)   (b)

Figure B.1.: MDT (a)β (b)t_0 in $-0.10 < \eta < 0.10$ region. Uncalibrated (yellow), element calibration (red), phase-shift calibration (blue), β-shift (black).
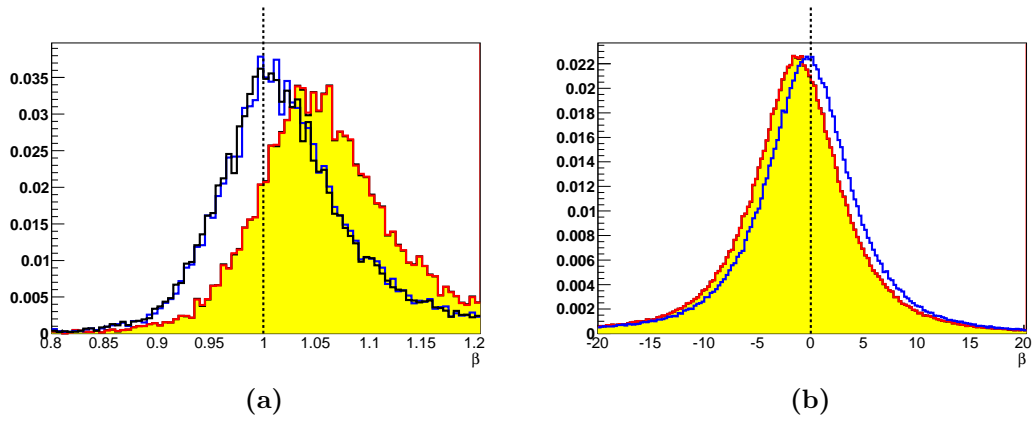
Figure B.2.: MDT (a)β (b)t_0 in $0.10 < |\eta| < 0.45$ region. Uncalibrated (yellow), element calibration (red), phase-shift calibration (blue), β-shift (black).
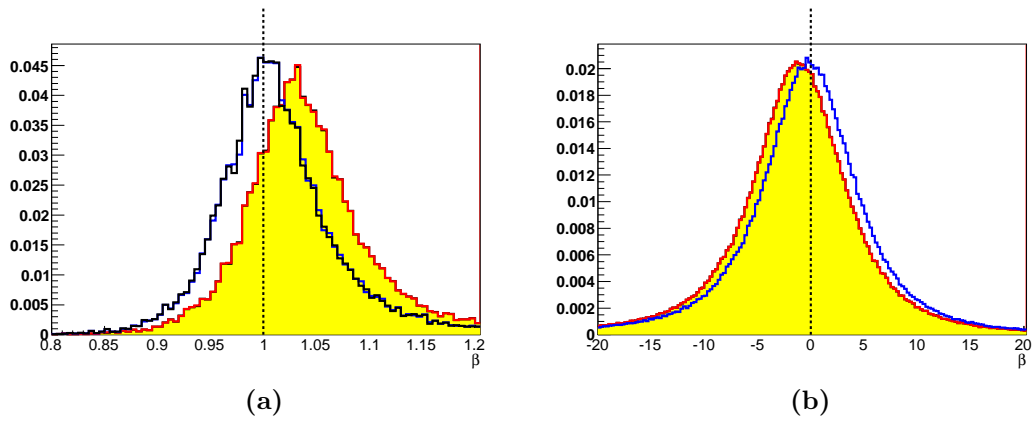

Figure B.3.: MDT (a)β (b)t_0 in $0.65 < |\eta| < 1.15$ region. Uncalibrated (yellow), element calibration (red), phase-shift calibration (blue), β-shift (black).
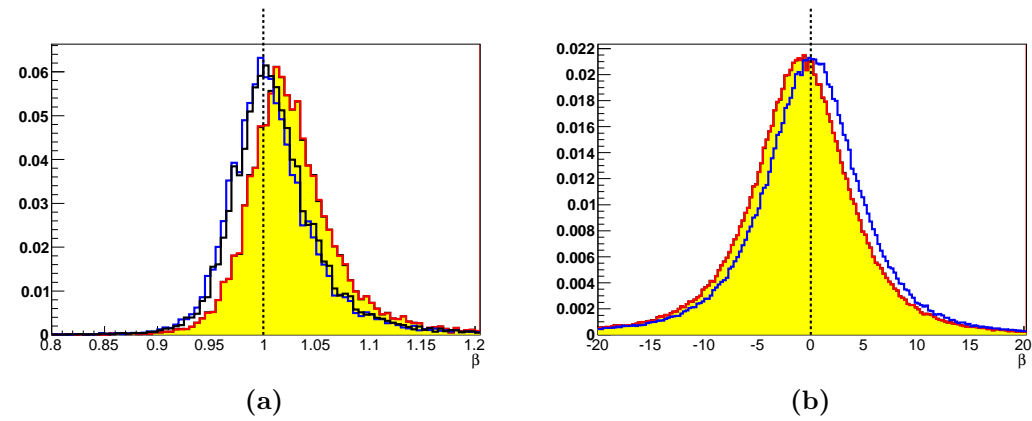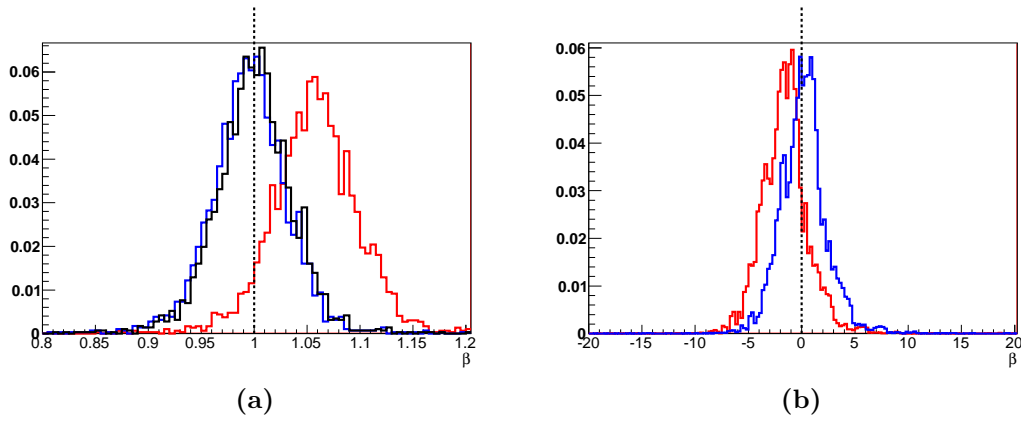

Figure B.4.: MDT (a)β (b)t_0 in $1.51 < |\eta| < 2.00$ region. Uncalibrated (yellow), element calibration (red), phase-shift calibration (blue), β-shift (black).

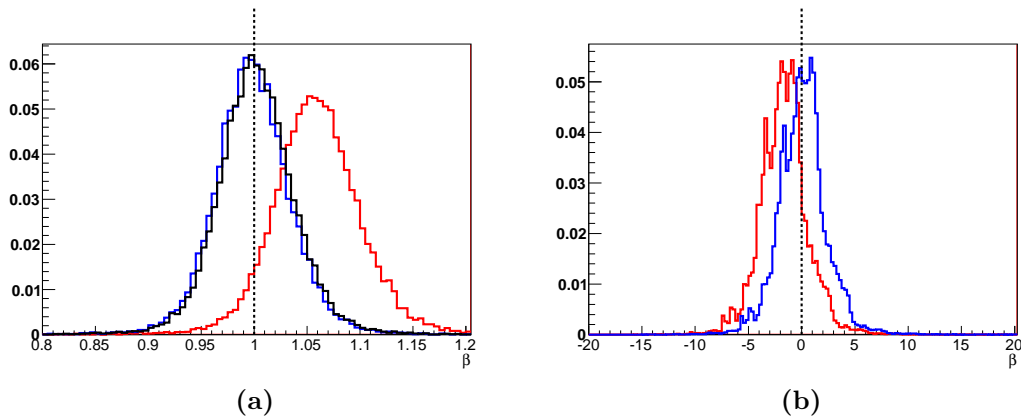**Figure B.5.:** RPC (a)β (b)t_0 in $-0.10 < \eta < 0.10$ region. element calibration (red), phase-shift calibration (blue), β-shift (black).

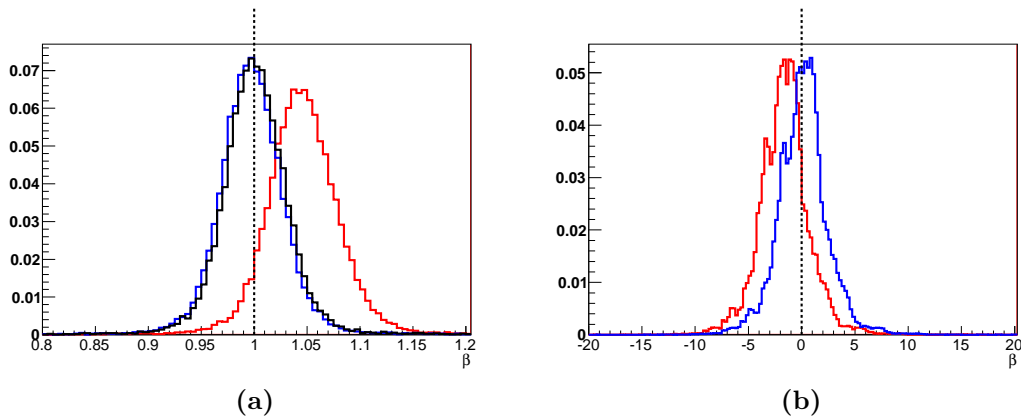**Figure B.6.:** RPC (a)β (b)t_0 in $0.10 < |\eta| < 0.50$ region. element calibration (red), phase-shift calibration (blue), β-shift (black).

Figure B.7.: RPC (a)β (b)t_0 in $0.50 < |\eta| < 1.20$ region. element calibration (red), phase-shift calibration (blue), β-shift (black).
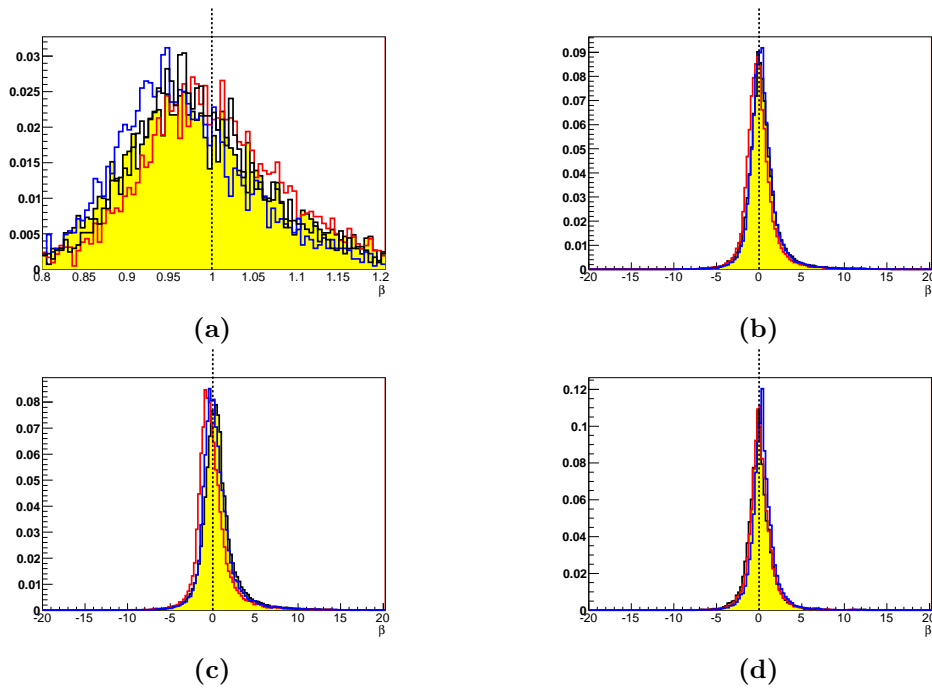
Figure B.8.: Calorimeter (a)β (b)t_0 (c)EMCal t_0 (d)Tile t_0 in $-0.10 < \eta < 0.10$ region. Uncalibrated (yellow), element calibration (red), phase-shift calibration (blue), β-shift (black).
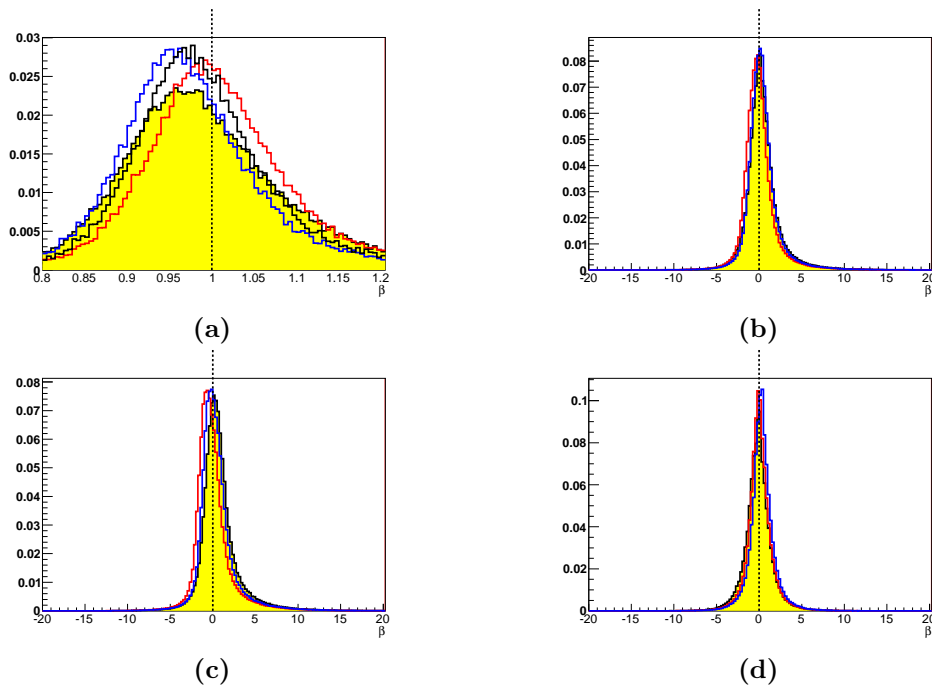

Figure B.9.: Calorimeter (a)β (b)t_0 (c)EMCal t_0 (d)Tile t_0 in $0.10 < |\eta| < 1.00$ region. Uncalibrated (yellow), element calibration (red), phase-shift calibration (blue), β-shift (black).

Figure B.10.: Calorimeter (a)β (b)t_0 (c)EMCal t_0 (d)Tile t_0 in $1.00 < |\eta| < 1.60$ region. Uncalibrated (yellow), element calibration (red), phase-shift calibration (blue), β-shift (black).
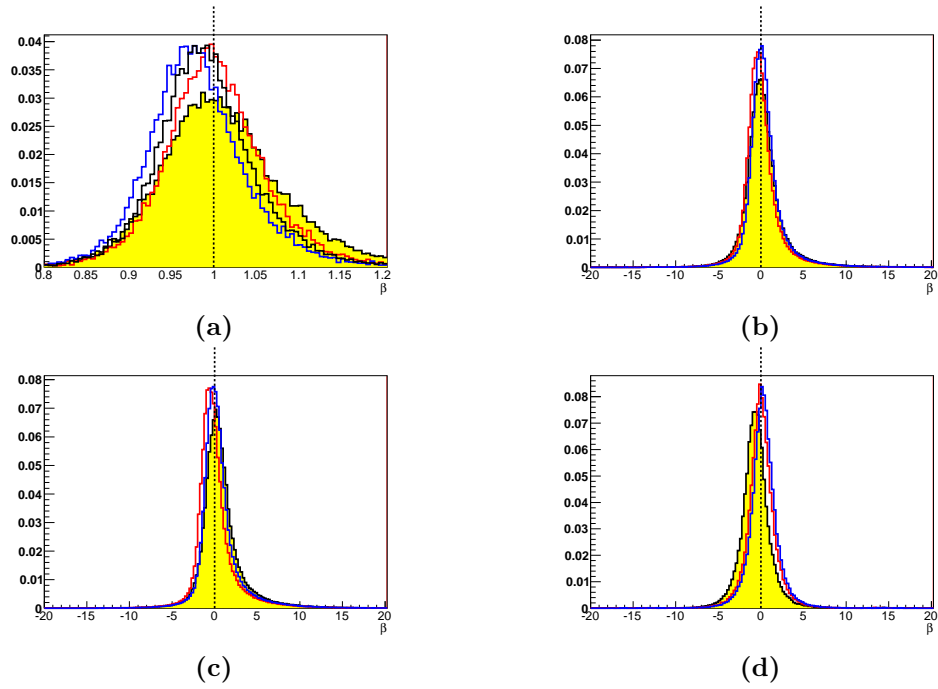

Figure B.11.: Calorimeter (a)β (b)t_0 (c)EMCal t_0 (d)HEC t_0 in $1.60 < |\eta| < 2.00$ region. Uncalibrated (yellow), element calibration (red), phase-shift calibration (blue), β-shift (black).
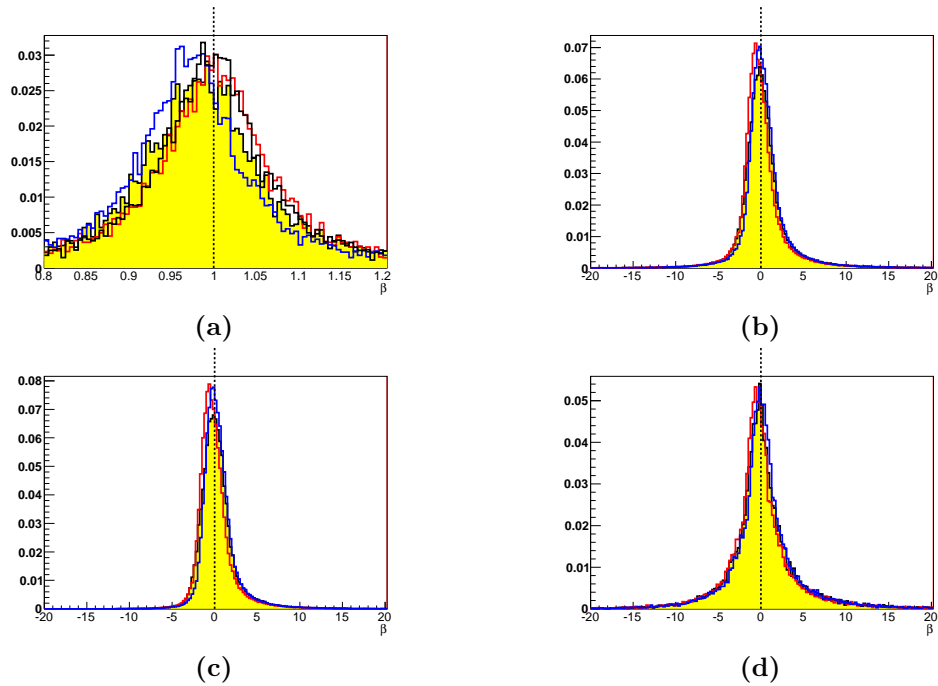
Bibliography

[1] W.N. Cottingham and D.A. Greenwood *An Introduction to the Standard Model of Particle Physics*, ISBN 0-521-58191-5 (1998)

[2] Chris Quigg *Gauge Theories of the Strong, Weak, and Electromagnetic Interactions*, ISBN 0-8053-6021-2 (1986)

[3] H. Baer, P.G. Mercadante, X. Tata, Y. Wang, *The Reach of the CERN Large Hadron Collider for Gauge-Mediated Supersymmetry Breaking Models*, Phys. Rev. D62 095007 (2000)

[4] M. Fairbairn, et. al. *Stable massive particles at colliders*, Physics Reports 438 1-63 (2007)

[5] The ATLAS Collaboration *Measurements of the electron and muon inclusive cross-sections in proton-proton collisions at $\sqrt{s} = 7$TeV with the ATLAS detector*, CERN-PH-EP-2011-108 (2011)

[6] The ATLAS Collaboration *Di-muon composition in ATLAS at 7 TeV*, ATLAS-CONF-2011-003 (2011)

[7] S. Dimopoulos, M. Dine, S. Raby, S. Thomas *Experimental Signatures of Low Energy Gauge Mediated Supersymmetry Breaking*, Phys. Rev. Lett. 76 3494-3497 (1996)

[8] M. Terwort *Searches for GMSB at the LHC*, DIS 2008 (2008)

[9] M. Ferro-Luzzi *Review of 2011 LHC run from the experiments perspective*, Chamonix 2012 Workshop on LHC Performance 38-53 (2012)

[10] The ATLAS Collaboration *The ATLAS Experiment at the CERN Large Hadron Collider*, JINST 3 S08003 (2008)

[11] The ATLAS Collaboration *ATLAS Detector and Physics Performance: Technical Design Report*, CERN-LHCC-99-14 (1999)

[12] The ATLAS Collaboration *The ATLAS Inner Detector commissioning and calibration*, Eur. Phys. J. C70 787-821 (2010)

[13] The ATLAS Collaboration *Performance of the ATLAS Inner Detector Track and Vertex Reconstruction in the High Pile-Up LHC Environment*, ATLAS-CONF-2012-042 (2012)

[14] R.A. Davis, P. Savard *A Study of Pileup Noise in the Barrel and Endcap Calorimetry*,

ATLAS Internal Note CAL-96-084 (1996)

[15] The ATLAS Collaboration *Liquid Argon Calorimeter: Technical Design Report*, CERN-LHCC-96-41 (1996)

[16] A. Artamonov et al *The ATLAS Forward Calorimeters*, JINST 3 P02010 (2008)

[17] Alex Read, *Modified frequentist analysis of search results (the* CL_s *method)*, 1st Workshop on Confidence Limit, CERN 81-101 (2000)

[18] Thomas Junk, *Confidence level computation for combining searches with small statistics*, Nuclear Instruments and Methods in Physics Research A 434 435-443 (1999)

[19] Niels van Eldik, *The ATLAS muon spectrometer: calibration and pattern recognition*, Thesis, NIKHEF, (2007)

[20] Jochem Snuverink, *The ATLAS muon spectrometer: commissioning and tracking*, Thesis, FOM, (2009)

[21] T. Lagouri et al. *A Muon Identification and Combined Reconstruction Procedure for the ATLAS Detector at the LHC at CERN*, IEEE Trans. Nucl. Sci. 51 6pt1 3030-3033 (2004)

[22] ATLAS Computing Group, *ATLAS Computing Technical Design Report*, (2005)

[23] Rene Brun and Fons Rademakers `ROOT` - *An object oriented data analysis framework*, Nuclear Instruments and Methods in Physics Research A 389 81-86, (1997)

[24] Robert S. Engelmore and Anthony Morgan, *Blackboard Systems*, Addison-Wesley Publishing Company, New York, (1988)

[25] The ATLAS Collaboration, *Searches for Heavy Long-Lived Charged Particles with the ATLAS detector in pp collisions at* $\sqrt{s} = 7TeV$, CERN-PH-EP-2011-077, (2011)

[26] The ATLAS Collaboration, *Searches for Heavy Long-Lived Sleptons and R-hadrons with the ATLAS detector in pp collisions at* $\sqrt{s} = 7TeV$, CERN-PH-EP-2012-236, (2012)

[27] Torbjorn Sjostrand, Stephen Mrenna and Peter Skands, *PYTHIA 6.4 Physics and Manual*, JHEP 0605:026, (2006)

[28] G. Corcella et al. *HERWIG 6.5: an event generator for Hadron Emission Reactions With Interfering Gluons (including supersymmetric processes)*, JHEP 0101:010, (2001)

Acknowledgements

I'd like to first thank the staff of Kobe University for helping me on the long journey from a Masters qualification in England to a Doctoral course in Japan. Particularly in this regard I am thankful to Professors Kiyotomo Kawagoe and Hisaya Kurashige for starting me on this path and helping me to see it through. I am also extremely grateful to Associate Professor Yuji Yamazaki, without whose tireless efforts in proof reading this thesis I would be at a severe disadvantage. Yumi Yokoyama is another member of staff to whom I am indebted. Over the course of my doctorate, her administrative expertise has saved me valuable writing up time.

For providing support in the development of MuonBetaRefit I express my thanks to Assistant Professor Takashi Matsushita, whose keen judgement on experimental methods proved invaluable. Sofia Vallecorsa, Enrique Kajomovitz, Shikma Bressler and Sascha Mehlhase of the ATLAS SMP group have also helped me considerably in the field of SMP searches. For introducing this particular avenue of research, I would also like to acknowledge Shogo Okada, who started initial development of the MuonBetaRefit tool.

On a more personal note I would like thank my family for their support over my years spent away from home, especially my mother for proof reading this thesis, despite understanding very little of the scientific content. I wish to thank Reiko, my girlfriend of 4 years, for putting up with the "Thesis Cave", as my isolation for the last few months has come to be known. Finally, I wish to sincerely thank my friends at CERN for providing much needed occasional distractions from "The Eldritch Horror" of writing a Doctoral thesis.